In-Situ Control of $BaZrO_3$ and $BaSnO_3$ Nanorod Alignment and Microstructure in $YBa_2Cu_3O_{7-x}$ Thin Films by Strain Modulated Growth

By

Francisco Javier A Baca

Submitted to the graduate degree program in Physics and Astronomy
and the Faculty of the Graduate School of the University of Kansas
in partial fulfillment of the requirements for the degree of
Doctor of Philosophy

Dissertation Committee:

_____
Chair: Dr. Judy Z. Wu

_____
Dr. Philip S. Baringer

_____
Dr. Siyuan Han

_____
Dr. Timothy J. Haugan

_____
Dr. Susan M. Williams

_____
Dr. Hui Zhao

Date Defended: November 17, 2009

The Dissertation Committee for Francisco Javier A. Baca certifies

that this is the approved version of the following dissertation:

In-Situ Control of $BaZrO_3$ and $BaSnO_3$ Nanorod Alignment and Microstructure in $YBa_2Cu_3O_{7-x}$ Thin Films by Strain Modulated Growth

_____

Chair: Dr. Judy Z. Wu

Date approved _____

Abstract

With the ability to carry very high electrical currents per unit area in kilometer length wires, high temperature superconductors (HTS) are especially promising candidates for applications where size and weight constraints are priorities. From military aircraft and naval applications to energy production by wind power, many types of power generation applications may operate under strenuous conditions, requiring current densities on the order of 10^5 A/cm^2 while subjected to magnetic fields of 3 – 5 T. In the absence of a magnetic field, this current density requirement is well within the intrinsic limits of $YBa_2Cu_3O_{7-x}$ (YBCO), but operation in high magnetic fields makes the problem of vortex motion a limiting factor to the critical current density, J_c. Vortex pinning by the insertion of non-superconducting oxides like $BaZrO_3$ (BZO) or $BaSnO_3$ (BSO) into the YBCO matrix is an effective means of addressing this problem since these defects self-assemble into columnar structures (nanorods) that provide strong pinning along the length of the flux-line. However, only limited control of nanorod geometry is possible by current growth methods. To meet the requirements of applications that operate in magnetic fields of varying intensity or orientation, this thesis aims to produce a defect landscape that may be designed to meet these demands, as the thin film is grown. Achieving this represents a major challenge in the development of HTS cables and power devices, requiring correlation of material synthesis and characterization on a nanometer scale. The microstructure of BZO- and BSO-doped YBCO thin films was studied using Transmission Electron Microscopy and the findings indicate that it is possible to produce a controllable defect landscape by manipulation of the strain relationships using vicinal substrates, as well as through controlled growth dynamics by varying growth temperature.

This work is dedicated to my supportive family,

and to my Love, Beth

Acknowledgements

The work shown in this thesis, and that leading toward it was a highly cooperative effort, and many thanks are due. The seemingly endless support of family, friends, and academic advisors was invaluable, and made it possible for me to finish my doctoral studies. My deepest thanks to you all – I could not possibly repay you in a lifetime for all your efforts and support.

Since nearly half of my graduate research was carried out while working for the Air Force Research Laboratories at Wright-Patterson Air Force Base, the number of people and resources involved in my education increased so significantly that it makes it impossible to list everyone individually. However, special thanks are due to my advisors, Professor Judy Wu, Dr. Timothy Haugan, and Dr. Paul Barnes. Their combined input, guidance, insight, and patience were invaluable in furthering my education and research skills. My thanks also go to the members of my graduate committee at KU for their careful evaluation and input into my dissertation. I also graciously acknowledge the generous support of the Mechanical Energy Conversion Branch, the Energy, Power and Thermal Division, and the Propulsion Directorate of AFRL, which made much of my research possible.

Since TEM work became an integral part of my research, a special thanks is also due to the staff of the AFRL Microstructural Characterization Facility of the Materials and Manufacturing Directorate. I especially thank Dr. Bob Wheeler, who guided me through much of the long process of learning these detailed techniques. Thank you also to Professor Haiyan Wang at Texas A&M University, whose individual guidance on the TEM accelerated my learning significantly.

My sincere thanks and appreciation also go to my fellow students and group members both at KU and at AFRL. Specifically, this work would have been impossible without the collaboration of Rose Emergo, Xiang Wang, Ronald Vallejo, Jonathan Dizon, Dan Fisher, Dr. Rongtao Lu, Dr.

Zhuangzhi Li, Caitlin Rochford, and Guowei Xu, all at KU. Thank you all for your kind support in measurements, learning, discussion, and of course, friendship (including stress-relieving picnics at Clinton Lake, complete with the endless entertainment of croquet, poker, and monopoly games). At AFRL, I am most grateful for the support of Dr. Chakrapani Varanasi, Dr. George Levin, Dr. Bang Tsao, Capt. John Bulmer, Jack Burke, Lyle Brunke, John Murphy, Neal Pierce, Josh Reichart, Matt Mullins, Kevin Yost, Eric Brewster, Jared Petry, John Olds, Mary Locke, Patrick Klenk, Lt. Breanna Ruter-Schoppman, Lt. Craig Harrison, Lt. Andy Chaney, and Lt. LaMarcus Hampton. Thank you also for help with samples, measurements, discussions, equipment, UCI (wow), and again, the close friendships (maintaining sanity through trivia nights, target shooting, and always keeping me smiling – even while sleep deprived). I wish I could say more about each person, but obviously that would be a chapter of its own. Instead, thank you all.

I am greatly indebted to all my immediate and extended family for their kind encouragement, enthusiasm, support, and interest in my studies over the many years of my combined undergraduate and graduate education. I give special thanks and recognition to my late mother, Evangeline, for patiently teaching me so much about how to learn, as well as how to be. The help and encouragement from my father, Rudolph, siblings, Rodolfo, Carlos, Joaquin, and Maria all made it possible for me to complete most of my educational pursuits. Thank you, and thanks to all my nieces, nephews, sisters- and brothers-in-law, grandparents, uncles and aunts who each played unique, yet significant roles in my development.

Most of all, however, my deepest and utmost appreciation goes to my Love, my friend, my wife, Beth. Continuing our respective educations involved spending almost four years of our lives travelling between two states, and any of my work in that time would be mute without her endless support and help. There are not words to express my gratitude. Instead, I look forward to our time together, cherish our memories, and express my deepest love to you.

Table of Contents

List of Figures viii
List of Tables xiv

Chapter 1 1

1.1 Basic Concepts of Superconductivity 2
1.2 Vortex Pinning in High Temperature Superconductors 5
1.2.1 VORTEX PINNING AT DEFECTS 5
1.2.2 INTRINSIC PINNING IN YBCO 6
1.2.3 ENGINEERED VORTEX PINNING: REVIEW OF PROGRESS 8
1.3 Inclusion of Nonsuperconducting Defects in YBCO: Microstructural Effects 14

Chapter 2 16

2.1 Sample Fabrication: Thin Film Growth by Pulsed Laser Deposition 16
2.2 Microstructural Characterization 18
2.2.1 TRANSMISSION ELECTRON MICROSCOPY 18
2.2.2 MICROSTRUCTURE AND CRYSTALLINE DEFECTS 21
2.2.3 SPECIMEN PREPARATION 22
2.3 Electrical Transport Measurement 26

Chapter 3 28

3.1 Nanorod Formation in YBCO Thin Films: Review of Potential Mechanisms 29
3.2 Surface Energies and Vicinal Surfaces 33
3.3 YBCO Thin Films and Nanorod Alignment on Vicinal Substrates 36
3.3.1 EXPERIMENTAL DETAILS 36
3.3.2 MICROSTRUCTURAL RESULTS 37
3.3.3 GROWTH MECHANISMS ON VICINAL SUBSTRATES 41
3.4 Superconducting Properties of Vicinal BZO-Doped YBCO 49
3.5 Conclusions 53

Chapter 4 54

4.1 Experimental Details **55**
4.2 Microstructural Results **56**
4.2.1 $BaZrO_3$ DOPING CONCENTRATION 56
4.2.2 LATTICE MISFIT AND NANOROD ALIGNMENT: $BaSnO_3$-DOPED YBCO 64
4.2.3 VERTICAL AND LATERAL CORRELATION OF DEFECTS – QUALITATIVE DESCRIPTION 67
4.3 Superconducting Properties **70**
4.4 Conclusions **76**

Chapter 5 **78**

5.1 Basic Growth Dynamics of Thin Films **80**
5.2 Experimental Details **83**
5.3 Microstructural Results **84**
5.4 Superconducting Properties with T_g **88**
5.5 Microstructural Mechanisms of Aligned Growth **95**
5.6 Conclusions **97**

Chapter 6 **99**

Conclusions and Future Directions **99**
6.1 Conclusions **99**
6.2 Future Directions **103**
References **105**
Publication List **114**

List of Figures

Figure 1.1: The superconducting order parameter and magnetic flux density as functions of position from the center of a vortex core for an isolated vortex (13).4

Figure 1.2: Two YBCO unit cells. 6

Figure 1.3: As reported by Ref. (20). Critical current density as a function of angle of incidence of applied magnetic field. At $\theta = 0°$, the field is oriented parallel to the *a*-*b* plane. The four curves are for field intensities of 1, 3, 5, and 7 Tesla as labeled. 7

Figure 1.4: From Ref. (28). Damage tracks in YBCO crystal irradiated by 580MeV Sn^{+} ions. The inset shows a cross-sectional view, while the main figure is taken at approximately 10° from the track direction. 9

Figure 1.5: Cross-sectional image of YBCO thin film doped with nanoparticle forming Y_2BaCuO_5. From Ref. (22). 11

Figure 1.6: Critical current density as a function of applied magnetic field. The curves labeled '211' and 'Y_2O_3' show the nanoparticle-doped YBCO films. The curve labeled 'BZO' shows typical pinning behavior of the nanorod-doped YBCO films (31). These measurements are taken at 77 K and for the applied field parallel to the YBCO *c*-axis ($H \parallel c$). 12

Figure 1.7: Plan-view (left) and cross-sectional view (right) of BZO-doped YBCO thin films, showing self-assembled cylindrical nanorods (25). 13

Figure 2.1: (a) Illustration of Pulsed Laser Deposition of thin film on temperature-controlled substrate (39). (b) Photograph of a plume produced from a YBCO target. 17

Figure 2.2: Simplified schematic of TEM beam path in analogy to a light projector. From Ref. (45). 19

Figure 2.3: From Ref (46), electron beam path in a TEM in imaging (left) and diffraction (right) modes. 19

Figure 2.4: Photographs of an FEI Titan 300keV TEM (left), and a Philips CM200 200 keV TEM. 20

Figure 2.5: Interface between a thin film (filled dots) and substrate (open dots) for (*a*) no misfit (homoepitaxial), (*b*) misfit accommodated by strain, (*c*) misfit accommodated by dislocation (48). 21

Figure 2.6: FEI Nova NanoLab dual-beam FIB system, as used to prepare foils for TEM characterization. 23

Figure 2.7: Side view of sample mounted for TEM foil preparation by FIB (52). 24

Figure 2.8: Sample preparation for cross-sectional TEM foil by FIB. (*a*) SEM image of sample viewed at 52° from the film normal, (*b*) protective Pt layer deposited, (*c*) trenches cut in bulk film (viewed normal to film surface), (*d*) trenches viewed at 52° tilt angle, (*e*) micromanipulator used to lift foil out of bulk film and attach to Mo holder, (*f*) cross-sectional view of foil thinned to final thickness. 26

Figure 2.9: From Ref. (54), magnetic field orientation for $J_c(\theta)$ measurements. 27

Figure 3.1: Cross-sectional TEM images of YBCO films doped with (a) 2 vol. % BZO, and (b) 4.5 vol. % BSO. Examples of the self-assembled nanorods are marked with arrows, and the scale bars indicate 50 nm. 31

Figure 3.2: Schematic of interfaces in doped YBCO thin film on substrate. Interfaces between the YBCO matrix and BZO are labeled by "1", and the interfaces between the surrounding YBCO and the substrate are labeled "2". 34

Figure 3.3: (a) Example of a vicinal $(3,\bar{2},16)$ surface of a face centered cubic crystal (70), (b) example of vicinal surface by miscut away from [001] toward [100] (71). 35

Figure 3.4: Cross-sectional TEM images of YBCO films with 2 vol. % BZO grown on (a) nonvicinal, (b) 5°, (c) 10°, (d) 15°, (e) 20° STO substrates. The single-

ended and double-ended arrows point to examples of self-assembled nanorods and stacking faults, respectively. The scale bars indicate 50 nm. 40

Figure 3.5: High-resolution cross-sectional TEM image of BZO-doped YBCO on 5° vicinal STO. The inclined a-b planes of the YBCO with respect to the macroscopic substrate surface, as well as a substrate terrace/step are visible..... 41

Figure 3.6: AFM images of (a) 1.2° vicinal STO before deposition, (b) the surface of 120 nm thick YBCO film on the 1.2° vicinal substrate, (c) YBCO film on nonvicinal STO (001). (a) – (b) from Ref. (78), (c) from Ref. (67). 42

Figure 3.7: As shown in Ref. (68), the (a) Island (Volmer-Weber), (b) Layer plus Island (Stranski-Krastanov), (c) Layer (Frank-Van der Merwe) growth modes. 43

Figure 3.8: Illustration of step-flow growth on a vicinal surface from Ref. (34). 43

Figure 3.9: From Ref. (78), the layered YBCO unit cell may be considered as three nearly cubic cells. If the height of the vicinal surface steps does not coincide with the size of a component cell, a dislocation results..... 44

Figure 3.10: TEM cross-section of YBCO film with 2 vol. % BZO on 10° vicinal STO substrate. The arrow points to a BZO nanorod, and the markers indicate dislocations in the surrounding matrix. The scale bar indicates 5 nm..... 47

Figure 3.11: $J_c(H)$ of 2 vol. % BZO-doped YBCO on vicinal STO measured at 77 K with the applied magnetic field parallel to the *c*-axis. Curves are shown for four vicinal angles (0° – 20°) (54)..... 49

Figure 3.12: $J_c(H)$ of 2 vol. % BZO-doped YBCO on vicinal STO measured at 77 K with the applied magnetic field parallel to the *a*-*b*-plane (54). 51

Figure 3.13: J_c of 2 vol. % BZO-doped YBCO as a function of the angle of incidence of the applied magnetic field for $H = 1$ T and $H = 5$ T (54). 51

Figure 4.1: Cross-sectional TEM images of nonvicinal YBCO films doped with (a) 2 vol. %, (b) 4 vol. %, (c) 6 vol. % BZO. Examples of adjacent nanorods are marked with arrows, and the scale bar indicates 50 nm. 57

Figure 4.2: Cross-sectional TEM images of YBCO films grown on 5° vicinal STO, doped with (a) 2 vol. %, (b) 4 vol. %, and (c) 6 vol. % BZO. Vertical arrows show examples of *c*-axis aligned nanorods, while the horizontal point out the *a*-*b* alignment. The scale bars indicate 50 nm..... 59

Figure 4.3: High-resolution cross-sectional TEM image of samples in Figure 4.2: (a) 4 vol. %, and (b) 6 vol. % BZO-doped YBCO on 5° vicinal STO..... 60

Figure 4.4: Left: High-resolution TEM images of (a) 4 vol. %, and (b) 6 vol. % BZO doped YBCO films. Right: Fourier filtered images of those on left. Some dislocations are marked with arrows 61

Figure 4.5: Cross-sectional TEM images of: (a) 4 vol. %, and (b) 6 vol. % BZO-doped YBCO films on 20° vicinal STO substrates. The scale bars indicate 20 nm. 63

Figure 4.6: Cross-sectional TEM images of YBCO films doped with 4.5 vol. % BSO on (a) nonvicinal, (b) 5°, (c) 10°, and (d) 20° STO substrates. 65

Figure 4.7: From Ref. (89), schematic of model for correlated growth of InAs quantum dots in GaAs matrix. 69

Figure 4.8: Critical current density as a function of magnetic field orientation measured at 1 T and 77 K. The 4 vol. % samples are shown in blue curves and 6 vol. % by red curves. BZO-doped YBCO on vicinal STO. Non-doped YBCO on 0° STO is shown for comparison (filled squares) (53). All symbols in the plot represent actual data points, while the connecting lines serve only as viewing guides..... 71

Figure 4.9: Critical current density with magnetic field orientation for YBCO films doped with 4.5 vol. % BSO on STO substrates with vicinal angles of 0°, 5°, and 10° (53). All symbols in the plot represent actual data points, while the connecting lines serve only as viewing guides..... 73

Figure 4.10: (a) Transition temperature, and (b) YBCO c-axis length as function of vicinal angle for 2 – 6 vol. % BZO and 4.5 vol. % BSO concentrations. Values for undoped YBCO are also shown for comparison (54). 75

Figure 5.1: Calculated diffusivity as a function of temperature. The horizontal axis is plotted in units of (k_B/E_D) while the vertical is scaled by D_o. 82

Figure 5.2: Cross-sectional bright field TEM images of YBCO thin films doped with 2 vol. % BZO. Images are shown for growth temperatures of 780° – 835°C, and the overlaid lines illustrate the paths of the BZO nanorods through the film. The scale bars represent 50 nm. 85

Figure 5.3: Average BZO nanorod length in YBCO matrix as compared to values reported in Ref. 5.5. The solid lines represent a polynomial fit to the data points shown by symbols. 87

Figure 5.4: J_c vs. applied magnetic field for YBCO films with 2 vol. % BZO with varied growth temperature. Data for an undoped ("pure YBCO") sample is included as a reference. An increasing trend with T_g is clear for H > 0.5 T, indicating a change in the vortex pinning structure. Each plotted point represents a measured value. 88

Figure 5.5: Flux pinning force (per unit volume) vs. applied magnetic field for T_g from 780° C to 835° C. The increasing value of $F_{p\,max}$ and H_{max} indicate the increased correlation of the BZO nanorods with T_g Each plotted point represents a measured value. 90

Figure 5.6: Values of the applied magnetic field at which the maximum flux pinning force density occurs. 90

Figure 5.7: Average separation between BZO nanorods as a function of growth temperature. The averages are based on multiple measurements of several cross-sectional TEM images at each temperature. The dashed line represents a polynomial fit to the data points shown by symbols. 91

Figure 5.8: Critical current densities at self-field, 1 T and 3 T as a function of growth temperature. The closed symbols are the data points collected in this work, and for comparison, the open symbols show the values reported in Ref. (96). The solid and dashed lines represent a polynomial fit to the data points shown by symbols. 93

Figure 5.9: Critical current density at self-field, 1 T and 3 T as a function of average nanorod length. Values are shown both for the work of this study and those from Ref. (96). The difference in peak positions of the fitted curves is indicated. The solid and dashed lines represent a polynomial fit to the data points shown by symbols. 94

Figure 5.10: Calculated plot of the effective probability for migration and correlated growth showing the dependence on temperature. (Expression derived by Xie, et al. Ref. (89)) 97

List of Tables

Table 3-I: Lattice mismatch values for common vortex pinning dopants with respect to YBCO along the three crystallographic directions. The [003] mismatch is shown since *c*/3 of the orthorhombic YBCO provides a closer match with the cubic structures. The values shown are calculated from the lattice parameters listed in Powder Diffraction Files published by the International Union of Crystallography. 30

Table 3-II: c-axis lattice parameter of 2 vol. % BZO-doped YBCO with vicinal angle as measured by X-ray diffraction (54)..... 46

Table 4-I: Average nanorod parameters measured from cross-sectional images of *nonvicinal* BZO-doped YBCO films. 57

Table 4-II: YBCO *c*-axis (in Å) with increasing BZO doping and vicinal angle, as measured by X-ray diffraction (54). 62

Chapter 1

Introduction

Upon their discovery, the breadth of applications for high temperature superconductors (HTS) was expected to be enormous [1]. With oxides such as $YBa_2Cu_3O_{7-x}$ (YBCO) that transition into the superconducting state well above the temperature of liquid nitrogen and have the ability to maintain this state inside a nonzero magnetic field, power handling applications were seemingly feasible. However, it was quickly observed that high-current applications of HTS were severely hindered by their ability to carry such currents beyond a critical value, I_c [2 – 3]. Although multiple factors ultimately determine I_c, the intrinsic limitation to YBCO has yet to be achieved [2]. Therefore, the demand for high performance, efficient conductors has motivated efforts to understand and overcome the obstacles that impede their potential capabilities. Recently, these demands have been further stimulated by the increasing awareness of the limitations of current energy sources, such as fossil fuels [4].

Applications suitable to HTS range from lightweight electric propulsion and power generation in aircraft and naval vessels to more efficient and reliable wind-powered generators [5 – 8]. For example, the ability to carry high current densities would, by one design, reduce the mass of a wind turbine by approximately 35%, while increasing the maximum power output from 5 MW to 8 MW, as compared to its copper-based counterpart [8 – 9]. However, applications like generators and

motors require the superconductor to operate in magnetic fields of ~3 – 5 T, and possibly under varying orientation [2]. Unfortunately, one of the significant contributors to a reduced I_c is the problem of vortex motion when the superconductor is operating in the presence of a magnetic field [10 – 11]. Overcoming this problem has been a topic of intense research, and although significant improvements have been reported for specific magnetic field configurations, the flexibility to meet the demands of specific applications is still lacking [2, 10 – 11].

Several aspects of the challenges to HTS applications may be approached from a materials design perspective, enabling the pursuit of superconducting properties that may be optimized to meet application-specific constraints. This is the topic of this dissertation, where the vortex pinning properties of doped YBCO thin films are addressed by attempting to produce a controlled defect landscape from the growth stage. We aim to enhance the performance properties necessary for applications by tuning the defect structure of the film, as it is grown.

1.1 Basic Concepts of Superconductivity

A superconductor is a material that is characterized by the absence of electrical resistance below a transitional temperature (T_c). In addition, a significant trait of a material in the superconducting state is the exclusion of magnetic flux. Up to a critical field value, the flux exclusion may be considered as the result of a complete diamagnetic counteraction of the applied field, and is commonly referred to as the Meissner effect. Separating two major categories of superconductors is the

extent of this in-field behavior. A type I superconductor, while below T_c, reverts to its normal state if an external magnetic field exceeds a specific value (H_c), whereas a type II material retains its superconducting state through phases as the field is increased. In a type II superconductor, as the magnetic field increases from zero to a value H_{c1}, the flux is completely excluded just as in a type I. Increasing beyond H_{c1}, magnetic field lines are admitted, contributing to the magnetic flux in quantized increments of $\Phi_o = 2.067 \times 10^{-15}$ T m (also called flux quanta, or fluxons) until the field intensity exceeds a second critical value, H_{c2}, and the normal state is again restored. For the nonzero flux through the superconductor, in the field range $H_{c1} < H < H_{c2}$, the material is said to be in a mixed or vortex state [3, 12].

The vortex state is so named because of shielding currents that encompass the regions of flux penetration, thereby locally isolating a region of non-superconducting material known as the vortex core [3]. The thermodynamic theory of Ginzburg and Landau generates length scales that also predict the dimension of the normal state vortex cores. These include the penetration depth λ, which determines the extent to which a magnetic field extends into a superconductor, and the coherence length ξ, which gives the minimum length over which a significant change in superconducting state (order parameter) can occur [12]. Figure 1.1, as plotted by Matsushita, shows the magnitudes of the magnetic flux density and order parameter for an isolated flux line as functions of position away from the vortex core [13].

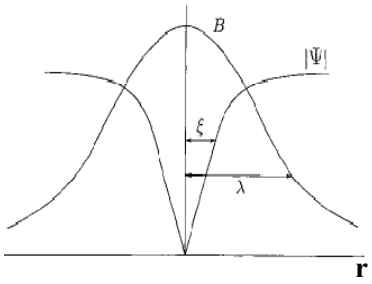

Figure 1.1: The superconducting order parameter and magnetic flux density as functions of position from the center of a vortex core for an isolated vortex [13].

We can see from the plot that the magnetic flux density is maximized at the vortex core ($r = 0$), while the order parameter is minimized. The number density of superconducting charge carriers is proportional to the squared magnitude of the order parameter, so we can see that as $|\Psi|$ approaches zero at the origin, the normal state is restored and the magnetic flux is fully admitted. Figure 1.1 also shows the significance of the penetration depth and coherence length as characteristic lengths for the size of a vortex core, with the diameter of the normal core spanning approximately 2ξ, and λ setting the distance from the core for significant decrease in the field intensity. In YBCO, the coherence length and penetration depths are anisotropic and temperature dependent, with approximate values of, $\xi_c \sim 0.14 – 0.8$ nm, $\xi_{a\text{-}b} \sim 1.2 – 4$ nm, $\lambda_c \sim 800 – 1121$ nm, and $\lambda_{a\text{-}b} \sim 150 – 210$ nm, where the subscripts denote the length along the *c*-axis and *a*-*b* plane, respectively (and where the lower values listed are for $T = 0$ K and larger for $T = 77$ K) [2 – 3, 14 – 18]. Here, and in subsequent references, the *a*, *b*, and *c* –axes refer to the crystallographic unit cell axes, using a right-handed convention.

1.2 Vortex Pinning in High Temperature Superconductors

In an ideal, unflawed superconductor, the forces acting on an individual flux line due to surrounding vortices are a consequence of a Lorentz-type interaction. Therefore, the magnitude of this repulsive force is proportional to the cross product of the velocity of the current carriers and the magnetic field ($\mathbf{F}_L = q[\mathbf{v} \times \mathbf{B}]$) and acts in an orthogonal direction to both **v** and **B**. In the absence of other outside forces, the flux lines then settle into an equilibrium state that minimizes their interaction, generally in the form of a triangular lattice [12]. Similarly, a transport current will exert a Lorentz-type force on the flux lines due to the motion of the transport charge carriers, breaking the equilibrium and inducing motion in them [3]. The movement of the flux lines then has an overall resistive effect, reducing the efficiency of current transport and limiting the current carrying capacity. This maximum current set by the resistive effect then adds the vortex-motion contribution to the critical current, and thus motivates finding a means to counter the interaction by inducing a state in which the flux lines are stabilized in an energetically preferred region.

1.2.1 Vortex Pinning at Defects

For a region in which the energy state of a flux line is reduced relative to a surrounding position, the gradient in energy would imply a force is required to change the position of the flux line [3]. This is referred to as a flux pinning force. If a transport current exerts a Lorentz force that is greater than a local pinning force, then vortex motion occurs, bringing with it added resistance. Therefore, it is important to

find a configuration that maximizes the local pinning of vortices. Because a normal core through a superconductor requires shielding currents, the free energy of the system is necessarily higher than it would be for a corresponding volume of a non-superconducting material (since in that case there is no need to generate the shielding currents) [3]. This implies that if a region of normal-state material were embedded in a volume of superconductor, the free energy of the system would be reduced for a flux line passing through the normal inclusion rather than generating shielding currents to pass through the superconductor. Hence, the interaction between the normal state inclusion and the flux core is attractive [13]. We may then define the critical current density (J_c) as that which causes the Lorentz force on the vortex core to overcome the attractive interaction with the pinning center [12]. Approaches to increase J_c through enhanced flux pinning have focused on methods of including regions of normal state, or significantly reduced order parameter, toward which the flux lines are attracted and penetrate in an energetically preferred fashion.

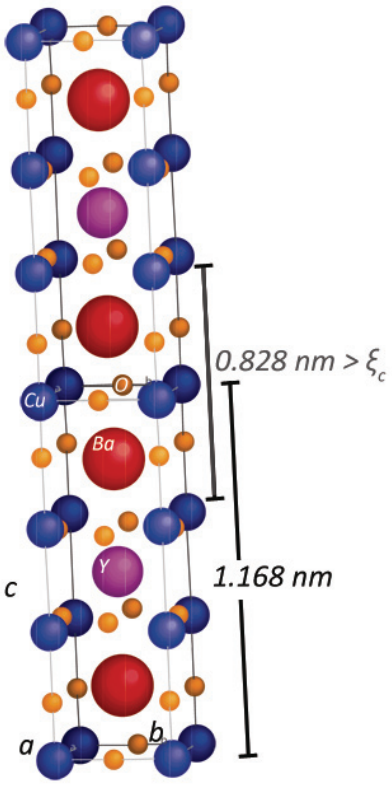

Figure 1.2: Two YBCO unit cells.

1.2.2 Intrinsic Pinning in YBCO

Because YBCO is structurally anisotropic, its layered structure happens to intrinsically provide a means of vortex pinning. Within the

orthorhombic YBCO unit cell, the supercurrent is mainly carried along Cu-O planes that are separated by a distance in the *c*-direction that exceeds the coherence length ξ_c, as illustrated in Figure 1.2. Therefore, coupling along the *c*-axis is weak compared to that through the *a*-*b* plane and regions with size on the order of ξ_c from the Cu-O planes are "weakly superconducting" [3]. The anisotropy then intrinsically provides vortex pinning for magnetic fields applied parallel to the *a*-*b* plane, since the flux lines energetically favor the weakly coupled regions, thus also making J_c angularly dependent [19]. This has been demonstrated experimentally, where a local maximum in J_c is observed when the applied field is parallel to the *a*-*b* plane, as shown by Horide, et al. in Figure 1.3, which plots the critical current density of a YBCO thin film as a function of the angle of incidence of the magnetic field, $J_c(\theta)$ [20].

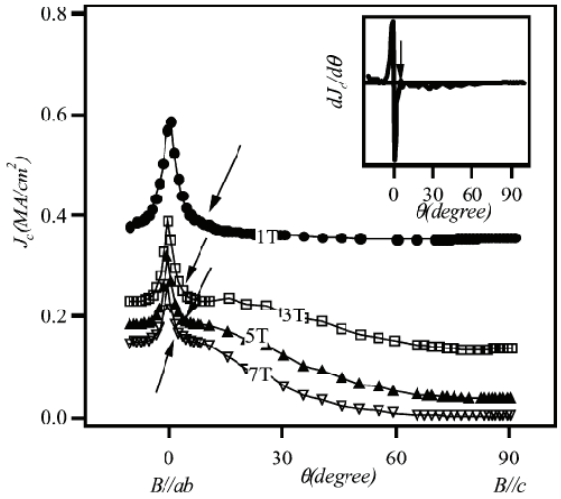

Figure 1.3: As reported by Ref. [20]. Critical current density as a function of angle of incidence of applied magnetic field. At θ = 0°, the field is oriented parallel to the *a*-*b* plane. The four curves are for field intensities of 1, 3, 5, and 7 Tesla as labeled.

1.2.3 Engineered Vortex Pinning: Review of Progress

Several techniques to locally regulate the order parameter have been attempted, most of which fall into the general categories of pinning by physical removal or alteration of superconducting material and the inclusion of normal state or reduced T_c phases into the YBCO matrix [21 – 26]. A necessary tradeoff is encountered in all these methods since including a volume of normal state material increases overall flux pinning force, but reduces the superconducting cross-sectional area. Thus, there is an extreme value when the density of normal inclusions exceeds that which makes their spacing less than the coherence length. Beyond this density, overlap of the normal cores may occur and the sample is dominated by non-superconducting material [21]. Therefore, an optimal value of pinning center density should be matched with the flux line density (field intensity) expected for the application.

The geometry of the defect, or normal state inclusion, is also an important factor since the vortex pinning force is additive along the flux line. Because of this, defects correlated along the direction of incidence of the magnetic field provide the maximum pinning force per unit length [3]. In addition, to minimize the displacement of the superconducting cross-section, the defect size should be minimized. Since, as discussed above, the radial length scale over which the normal core extends is roughly the coherence length, we strive for defects whose diameter is approximately $2\xi_{ab}$ [13]. For these reasons, columnar defects of ~3 – 8 nm that align

with the direction of magnetic field incidence are generally considered optimal vortex pinning geometries [3, 11, 13] .

1.2.3.1 High Energy Ion Beam Irradiation

Pinning enhancement by generation of columnar defects has been achieved by damaging the structure severely enough that the material is not superconducting along tracks into the crystal. Irradiation by heavy ions can produce defect columns on the order of 5 – 7 nm in diameter and up to several micrometers long, as shown in Figure 1.4 [21, 27 – 28]. The dark lines in this electron image show the damage tracks from a viewing perspective approximately 10° away from the column axes, while the inset shows a cross-sectional view [28].

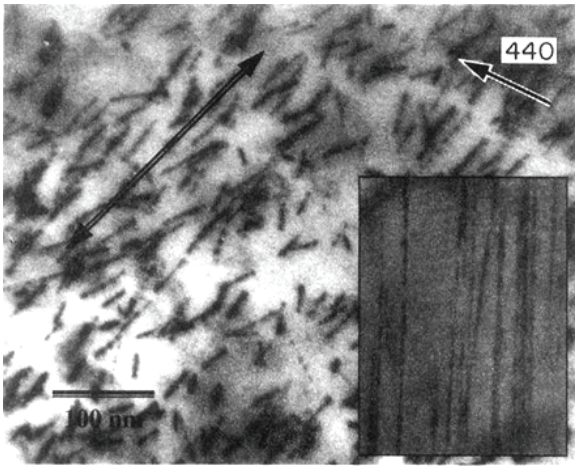

Figure 1.4: From Ref. [28]. Damage tracks in YBCO crystal irradiated by 580MeV Sn^{+} ions. The inset shows a cross-sectional view, while the main figure is taken at approximately 10° from the track direction.

The main mechanism of defect inclusion by irradiation is structural damage by collision or ionization resulting from the interaction with incident particles [21].

The nearly cylindrical shapes and diameters of the normal inclusions are theoretically predicted to provide nearly ideal flux pinning [11]. However, the effects observed are dependent on the incidence angle of the field relative to the defect alignment, and a reduction in T_c is also noted [2, 21]. Additionally, remnant materials may be radioactive, making safe handling difficult and costly [1].

However, ion irradiated YBCO does show improvements in J_c when the applied magnetic field is parallel to the damage tracks. Civale, et al. showed improved pinning in YBCO single crystals irradiated by 580 MeV Sn^+ ions, maintaining $J_c \sim 10^5$ A/cm^2 at fields up to 5 Tesla, compared to negligible J_c in the undamaged YBCO at the same field [21]. These improvements diminished for magnetic field intensities exceeding the "matching field", which is a way of quantifying the defect density in terms of the flux quantum, $n = B/\Phi$ [21]. Although ion irradiation is not necessarily a practical means of generating vortex pinning sites, these experiments demonstrated the effectiveness of the columnar defect geometry, and the high pinning force per unit length it provides since the flux lines are stabilized along their path through the superconductor.

1.2.3.2 Second-Phase Inclusions

With the dramatic vortex pinning enhancement shown by ion irradiation, more practical in-situ methods of incorporating comparable defect structures were sought. This introduced many materials challenges, including the chemical compatibility of the non-superconducting inclusions (or dopants), as well as the structural interactions

with the YBCO matrix. Several oxides have been shown to reasonably maintain compatibility with YBCO, including Y_2BaCuO_5 (211), Y_2O_3, $BaZrO_3$ (BZO), $BaSnO_3$ (BSO), and the respective structures they form within the matrix have generated significant interest for their vortex pinning properties [22, 24 – 26, 29]. Interestingly, the structural relationships of the dopant with the matrix significantly influence the geometry of the inclusions, and thus the vortex pinning properties. Both the method of insertion and the type of dopant used appear to influence the shape of the inclusions, indicating the significant roles of growth and the structural relationships.

Early reports of in-situ doping by second phase inclusions showed that sequentially delivering small quantities of 211 and YBCO (in a multilayer fashion) produces distinct 211 nanoparticles of approximately 9 – 14 nm diameter within the YBCO matrix, as illustrated in Figure 1.5 [22, 30].

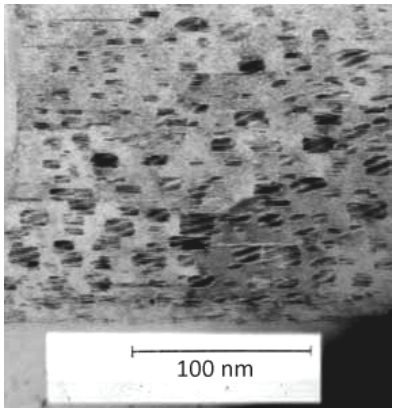

Figure 1.5: Cross-sectional image of YBCO thin film doped with nanoparticle forming Y_2BaCuO_5. From Ref. [22].

Similar particle inclusions are also seen in Y_2O_3-doped YBCO films, with comparable diameters of 8 – 13 nm under equivalent growth conditions [30]. The

critical current density is improved when these nanoparticles are included, especially at low to moderate applied magnetic field intensities. Specifically, inclusion of 211 particles showed an increase in J_c by a factor of 2 – 3 at an applied field of 1.5 T when compared to a single-layer YBCO film [22]. The multilayer particle inclusion of Y_2O_3 showed only a slightly smaller increase in J_c over a comparable range of applied fields, up to ~ 4 T, as illustrated in Figure 1.6 [31]. In this figure, which plots J_c as a function of applied magnetic field intensity, the curves labeled '211' and 'Y_2O_3' show the J_c dependence for the nanoparticle-doped YBCO films as well as an

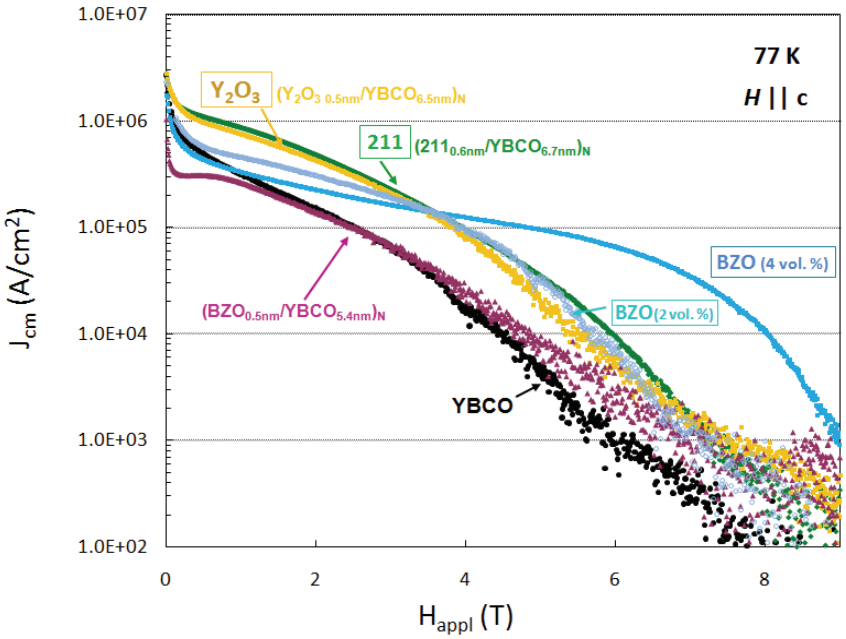

Figure 1.6: Critical current density as a function of applied magnetic field. The curves labeled '211' and 'Y_2O_3' show the nanoparticle-doped YBCO films. The curve labeled 'BZO' shows typical pinning behavior of the nanorod-doped YBCO films [31]. These measurements are taken at 77 K and for the applied field parallel to the YBCO *c*-axis (H || c).

undoped film, labeled 'YBCO' (other dopant configurations are also shown and some distinctions between them will be discussed below). From the nearly random particle

distribution seen in Figure 1.5, we may also expect to see less angular dependence than the columnar pinning structures, but at the expense of net pinning strength. However, this clearly demonstrates that as-grown defects indeed serve as effective vortex pinning structures, and the distributed nanoparticles may be especially well suited for applications under applied magnetic fields up to 3 – 4 T at liquid nitrogen temperatures.

An interesting effect was later observed when BZO or BSO were used as YBCO dopants [25 – 26]. With these additions, the inclusions produce self-assembled columnar structures comparable to the damage tracks observed in ion irradiated YBCO. An example of these structures is shown in Figure 1.7, which for BZO typically shows nearly cylindrical structures of 5 – 7 nm diameter [25].

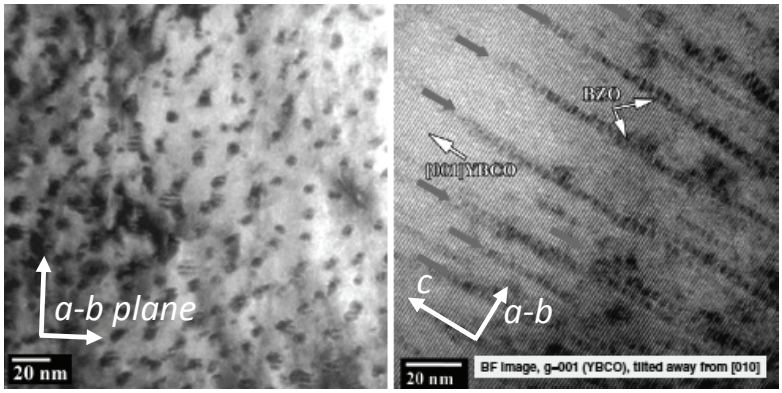

Figure 1.7: Plan-view (left) and cross-sectional view (right) of BZO-doped YBCO thin films, showing self-assembled cylindrical nanorods [25].

In Figure 1.7, which shows images with a viewing perspective down the direction of growth (also called plan-view) and along a cross-section, we see the columns (nanorods) extend nearly continuously through the YBCO film. Because of this, the

flux-line is pinned along its length, just as in the irradiated samples, and we may again expect a directional improvement in J_c for a magnetic field applied parallel to their axes. The curve labeled 'BZO' in Figure 1.6 shows the enhanced vortex pinning that is characteristic of these columnar defects for a magnetic field parallel to the nanorods and the YBCO *c*-axis ($H \parallel c$). Here we see that J_c is significantly enhanced for higher intensity magnetic fields of approximately 2 – 8 T, as may be expected for the high net vortex pinning force of the continuous nanorods. BSO-doped YBCO films show similar cylindrical nanorods, but with slightly larger diameters of 5 – 11 nm [26].

1.3 Inclusion of Nonsuperconducting Defects in YBCO: Microstructural Effects

Strain-mediated growth mechanisms have been attributed to the formation of nanorods in the YBCO matrix [25, 32]. By inserting structures of different phase into the YBCO matrix, the crystal lattices of each material are forced to match at the interface between them. However, since the microstructural strain describes the relative displacement of atoms from their equilibrium positions in a crystal lattice, then if the lattice parameters of the respective materials are not equal, a strained state results [33]. The role of strain will be discussed further in Chapters 3 – 4, but we have seen some evidence indicating its importance through the differences in the structures formed by varied dopants described above.

Displacing the lattice from its relaxed state requires energy, thus making an interface between highly mismatched lattices less favorable than one of lower

mismatch [34]. Since the lattice parameters of BZO, BSO and 211 are mismatched to YBCO, the minimum energy state would minimize the interfacial area between them. Thus, the dopant phases preferentially grow at a position where this phase already exists. Each of the dopants mentioned above has differing mismatch to YBCO (Chapters 3 – 4), which may begin to explain the different geometries observed [22, 25 – 26].

While the second-phase doped films show improved vortex pinning when compared to undoped YBCO, it is noteworthy that the geometry of the produced defect structure is largely restricted to those described. However, since individual applications may impose distinct operating conditions, including varied magnetic field orientation and intensity, producing an effective vortex pinning configuration requires some ability to control the defect geometry. By experimentally studying the microstructure and corresponding superconducting properties, we have investigated the controlled alignment of nanorods in strain modulated BZO- and BSO-doped YBCO thin films.

Chapter 2

Experimental Methods

2.1 Sample Fabrication: Thin Film Growth by Pulsed Laser Deposition

As introduced in Chapter 1, defects that are inherent to the growth of YBCO thin films help improve the vortex pinning properties when compared to single-crystals, making effective techniques for fabrication necessary [35 – 36]. The ability to deliver controlled stoichiometries over a moderate range of background gas pressures makes Pulsed Laser Deposition (PLD) a suitable technique for the growth of oxide thin films, including YBCO [37]. A form of physical vapor deposition, PLD uses high energy, short duration laser pulses to ablate a solid target, ejecting an ionized plume of vapor and, under some circumstances, solid and liquid phases [37]. A schematic illustrating an example of an experimental PLD system is shown in Figure 2.1 (a), and a photograph of a plume generated during ablation of a YBCO target is shown in Figure 2.1 (b). The pressure of the background gas aids in confining the plume shape, and for YBCO growth, provides necessary oxygen to produce optimal transition temperatures [3].

In this experiment, the growth conditions were chosen using parameters optimized for high performance YBCO films [38]. The conditions that were held constant in all samples discussed in this work are a background pressure of 300 mTorr O_2, laser fluence of approximately 3.2 J/cm^2 at 248 nm wavelength, and an 8 Hz pulse rate. For the vicinal BZO-doped samples discussed in Chapters 3 – 4,

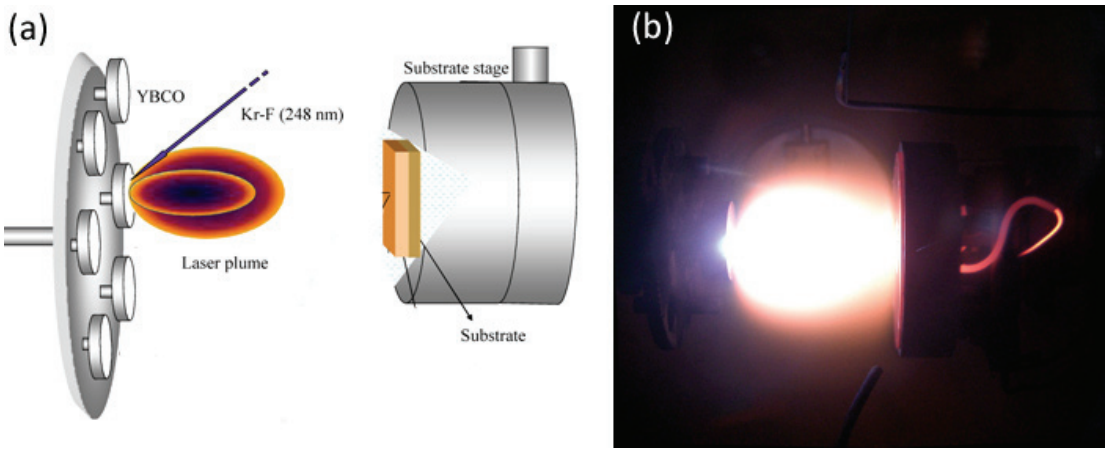

Figure 2.1: (a) Illustration of Pulsed Laser Deposition of thin film on temperature-controlled substrate [39]. (b) Photograph of a plume produced from a YBCO target.

separate targets with varied dopant concentrations were used, and the growth temperature was fixed at 810° C. To study the growth dynamics, the samples discussed in Chapter 5 were grown with substrate temperatures ranging from 780° C – 835° C.

Targets for ablation of BZO-doped YBCO were made by adding $BaZrO_3$ powder (SCI Inc., 99.0% purity) in varied concentration, to commercially available $YBa_2Cu_3O_7$ powder (Nexans Inc.) to produce the required volume concentration. The combined powders were thoroughly mixed using an agate mortar and pestle producing a homogeneous mixture. Cylindrical targets were formed in a steel die and pressed to 3000 psi, and sintered at 850° C – 920° C for 240 hr. After final sintering, typical carbon content of the targets was less than 200 ppm, and their densities ranged from 91 – 93% of the maximum bulk density.

2.2 Microstructural Characterization

2.2.1 Transmission Electron Microscopy

As introduced in Chapter 1, regions of reduced superconducting order parameter in the YBCO matrix, including microstructural defects and inclusions of secondary phases, act as pinning sites for magnetic fluxons, or vortices [35 – 36]. To minimize the disruption to the cross-sectional area, the size scale of the vortex pinning is ideally on the order of the coherence length of YBCO, approximately 3 nm, though in practice, artificially inserted second-phase defects range from 4 – 11 nm in diameter for both nanoparticle and nanorod geometries [22, 24 – 25, 30, 40 – 42]. Imaging structures of this length scale makes electron microscopy a strong candidate in the choice of characterization techniques. In particular, Transmission Electron Microscopy (TEM) provides the resolution to resolve features down to 0.5 – 1 nm in modern instruments [43 – 44].

To illustrate the basic operation, Figure 2.2 shows an extremely simplified schematic of the electron optics in a TEM that emphasizes the analogy to a light projector [45]. In most TEMs, electrons are accelerated in vacuum to 100 – 300 keV, and collimated by magnetic lenses, exposing a thin specimen. The transmitted

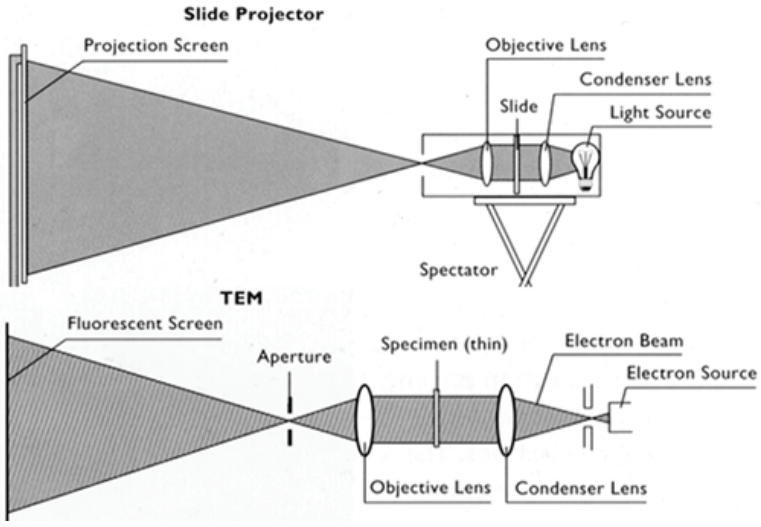

Figure 2.2: Simplified schematic of TEM beam path in analogy to a light projector. From Ref. [45].

electron beam is then focused through a series of lenses, as shown in Figure 2.3, to form an image on a fluorescent screen in the image plane [46]. A fraction of the beam may be scattered by the crystal lattice of the sample, where under interference

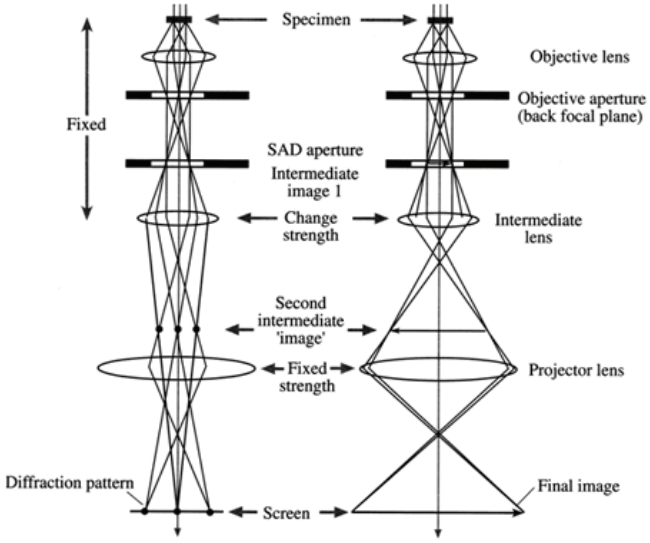

Figure 2.3: From Ref. [46], electron beam path in a TEM in imaging (left) and diffraction (right) modes.

conditions, a diffraction pattern is produced [43]. Examples of actual TEMs are shown in the photographs of Figure 2.4.

Contrast in TEM images results from several mechanisms, including sample mass and thickness variation [43, 47]. In the crystalline YBCO samples examined in our experiments, we may generally attribute image features to a combination of mass-thickness and diffraction contrast, the latter of which results from differences in the crystalline orientation or structure within the sample.

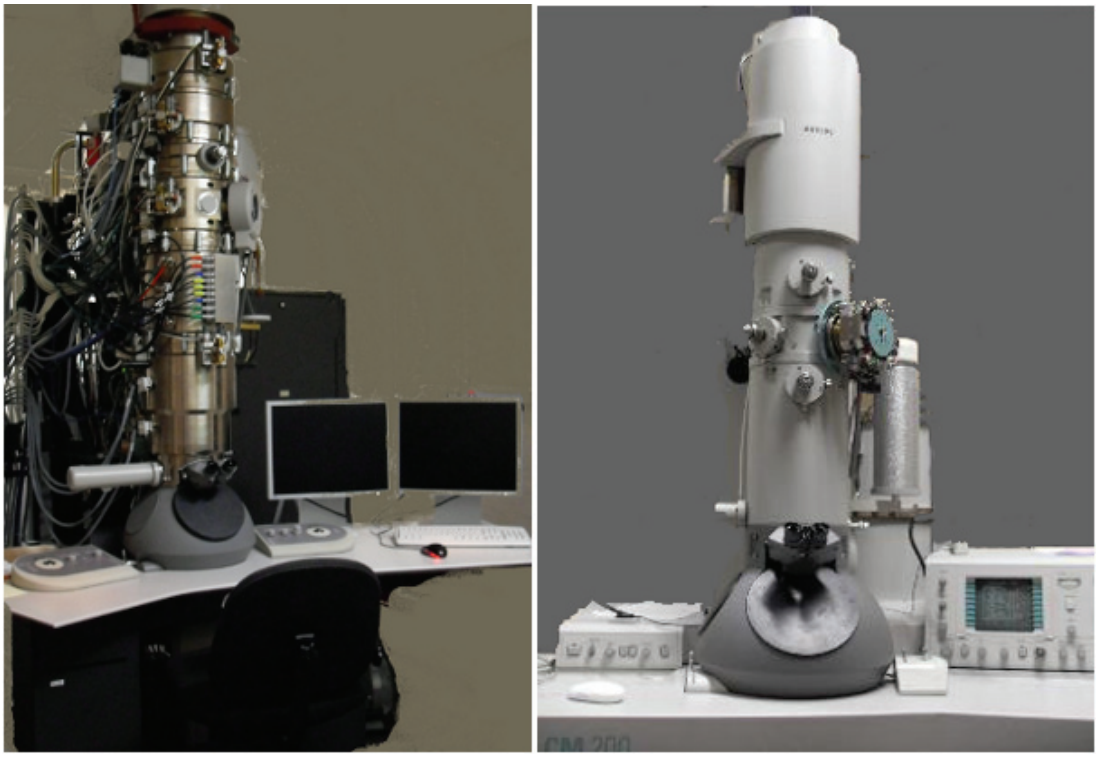

Figure 2.4: Photographs of an FEI Titan 300keV TEM (left), and a Philips CM200 200 keV TEM.

2.2.2 Microstructure and Crystalline Defects

Epitaxy is defined as the growth of a thin film that crystallographically follows the structural template of the substrate [48]. If the deposited film and the substrate have some mismatch between their respective lattices, but still form a structured crystal, the growth is considered heteroepitaxial. In this case, the mismatch, or misfit, between atomic sites on the lattices is accommodated by either straining the growing film, or by introducing a defect. This is illustrated in Figure 2.5, which shows (*a*) no misfit between the film and substrate (homoepitaxial), (*b*) misfit accommodated by a strained interface (where $a' < a$ denotes a strained lattice), and (*c*) formation of a misfit dislocation [48]. In general, identifying and characterizing dislocations is non-trivial [47, 49]. However, owing to the layered

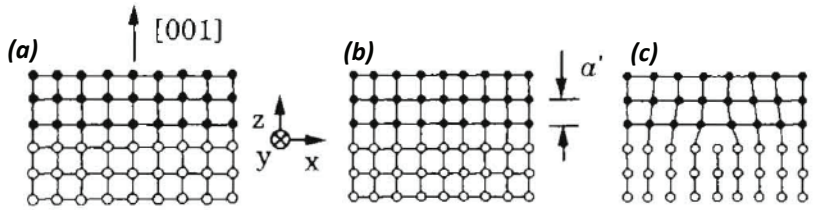

Figure 2.5: Interface between a thin film (filled dots) and substrate (open dots) for (*a*) no misfit (homoepitaxial), (*b*) misfit accommodated by strain, (*c*) misfit accommodated by dislocation [48].

structure of YBCO, misfit dislocations are observable by TEM imaging, and show up as interruptions in the otherwise continuous lattice planes [50 – 51].

2.2.3 Specimen Preparation

In the discussion of TEM imaging above, electron beam transmission through the sample is assumed. However, since the probability of multiple scattering interactions is strongly dependent on the mean free path, the size of the sample in the direction parallel to the beam (thickness) must be very small [47]. The thickness for "electron transparency" depends on several factors including the atomic number, but in general and for the samples examined here, 100 – 200 nm is roughly the targeted value. Because of the historical precedence of early TEM work focused on metallic materials, the term "foil" is commonly used to refer to the thinned specimen, and this convention is used in later chapters [43].

Thinning a bulk crystal to the sub-micrometer dimensions required for TEM analysis is a non-trivial and time intensive process that may have the potential to introduce artifacts or damage to the sample. These undesired effects may be minimized, however, by selecting preparation techniques appropriate to the specific sample composition and by considering the data to be acquired. One traditional technique includes mechanical cutting, grinding and polishing with progressively finer diamond abrasives. The single crystal ceramic substrates used for YBCO growth in this experiment (such as $SrTiO_3$ and $LaAlO_3$) are mechanically brittle, making the samples even more prone to damage by mechanical thinning techniques. For this reason, and because the vicinal substrates used are microscopically

anisotropic (as described in Chapter 3), most samples in this study were prepared for TEM using the Focused Ion Beam (FIB) technique described below.

Similar in design to a Scanning Electron Microscope (SEM), a dual-beam FIB is capable of scanning an electron beam for imaging, with the added control of surface modification using a 5 – 30 keV ion beam. As pictured in Figure 2.6, FEI Nova NanoLab and FEI DB235 dual-beam systems were used to prepare most of the samples in this experiment.

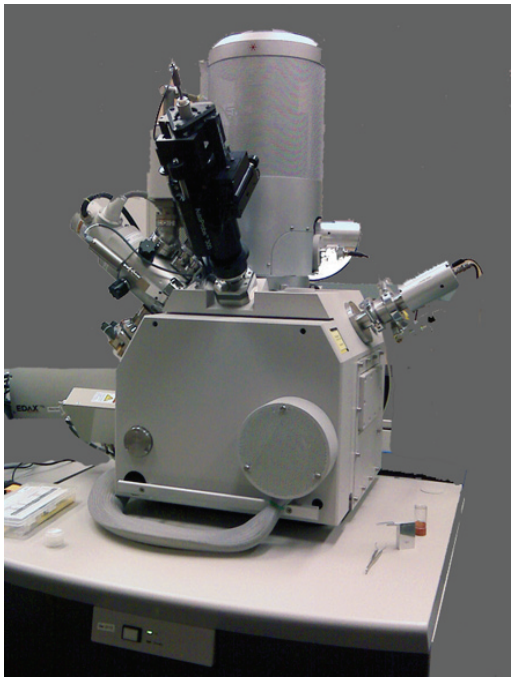

Figure 2.6: FEI Nova NanoLab dual-beam FIB system, as used to prepare foils for TEM characterization.

For FIB cross-sectioning, thin film YBCO samples grown on STO substrates were mounted on Cambridge-type SEM pin stubs using friction fit aluminum foil to

mechanically stabilize the sample, as illustrated in Figure 2.7. This mounting has an added benefit of maintaining electrical grounding between the YBCO film and the

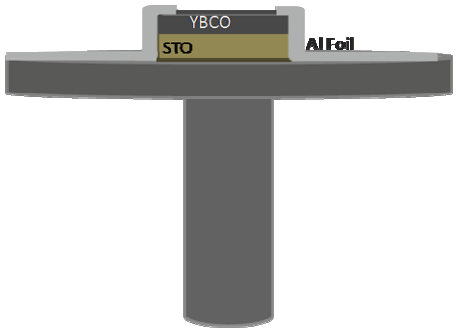

Figure 2.7: Side view of sample mounted for TEM foil preparation by FIB [52].

SEM stub without risk of chemical contamination from solvent-based bonding such as colloidal silver paint [52].

The procedure used to cut the cross-sectional samples from the YBCO films in this experiment is outlined in Figure 2.8. A low magnification image of the sample tilted by 52° with respect to the electron beam is shown in part (a) of this figure, where the YBCO film surface, one side of the STO substrate, and the aluminum foil mounting are visible. In Figure 2.8 (b), a protective layer of platinum approximately 20 μm x 1.5 μm x 1.5 μm was patterned and deposited in-situ. This layer serves to prevent ion damage and implantation into the YBCO film in the area of interest, and defines the shape of the section to be cut in subsequent steps. The dashed lines are drawn parallel to the surface steps in this particular sample, which was grown on 10° vicinal STO. This highlights a significant advantage of this method of sample preparation since the cross-section is cut precisely perpendicular to the vicinal steps.

In Figure 2.8 (c) trenches approximately 3 – 5 μm deep were cut into the film/substrate using a 30 keV Ga^+ ion beam, imaged normal to the film surface. In Figure 2.8 (d), the sample was tilted such that the ion beam was incident at ~30°, allowing the bottom edge of the foil to be cut free of the bulk substrate. A needle-shaped tungsten micromanipulator (OmniProbe 3000) was attached to one end of the foil, and it was subsequently cut loose, lifted out of the bulk sample, and mounted on a molybdenum TEM grid, shown in Figure 2.8 (e). The foil was then thinned to electron transparency, approximately 100 – 200 nm, and a side view is shown in Figure 2.8 (f). A lower Ga^+ ion flux was used during final thinning to control damage to the film. The films were examined in a TEM to roughly gauge the foil thickness, and subsequently polished incrementally with 1.5 keV – 600 eV Ar^+ ions incident at 10° (Fischione NanoMill 1040).

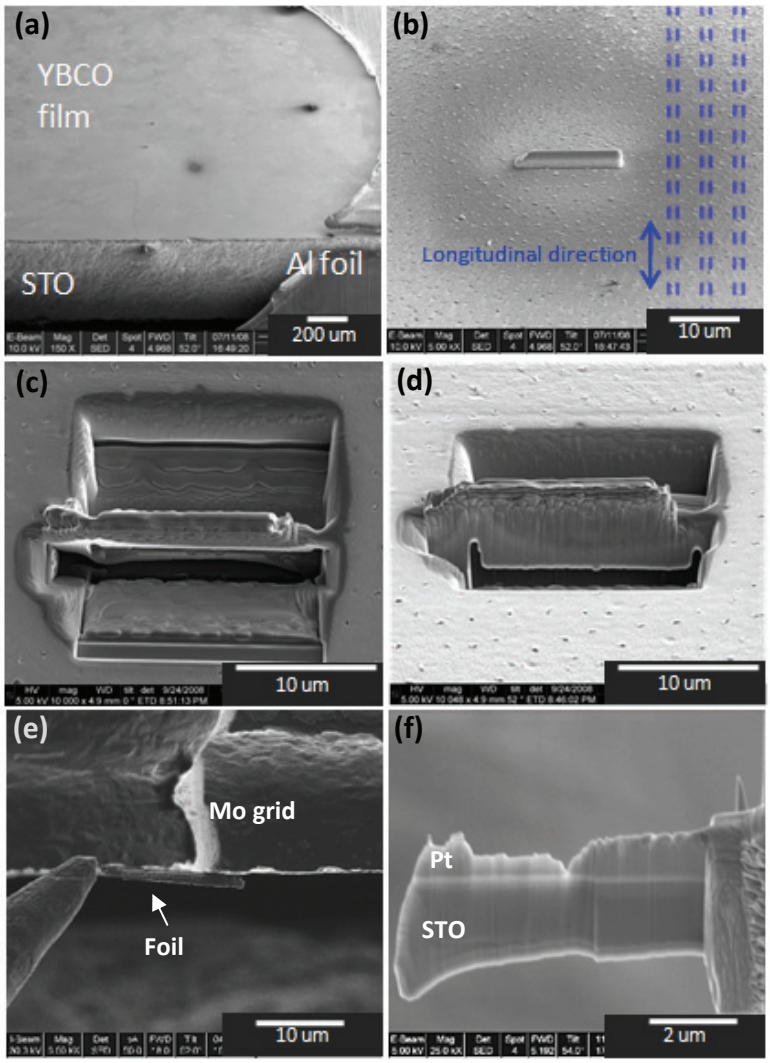

Figure 2.8: Sample preparation for cross-sectional TEM foil by FIB. (*a*) SEM image of sample viewed at 52° from the film normal, (*b*) protective Pt layer deposited, (*c*) trenches cut in bulk film (viewed normal to film surface), (*d*) trenches viewed at 52° tilt angle, (*e*) micromanipulator used to lift foil out of bulk film and attach to Mo holder, (*f*) cross-sectional view of foil thinned to final thickness.

2.3 Electrical Transport Measurement

Electrical transport properties were measured in the direction parallel to the surface steps of the vicinal samples, using a four-point measurement [53]. The

superconducting transition temperature was determined by measuring the resistivity as a function of temperature while cooling from 305 K to 77 K.

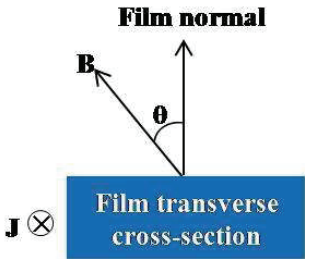

Figure 2.9: From Ref. [54], magnetic field orientation for $J_c(\theta)$ measurements.

The critical current density dependence on applied magnetic field intensity and angle of incidence, $J_c(H)$ and $J_c(\theta)$, respectively, were measured using an 8 T superconducting magnet in the maximum Lorentz force configuration shown in Figure 2.9 [54].

Chapter 3

Controlled Alignment of Nanorod Growth in YBCO by Substrate Mediated Strain

As introduced in Chapter 1, the columnar structures that form within a $BaZrO_3$-doped YBCO thin film provide an effective vortex pinning mechanism for a magnetic field applied normal to the plane of a transport current (parallel to crystallographic *c*-axis). However, the growth mechanisms that guide the alignment direction and nearly cylindrical shape are not fully understood.

It is generally accepted that the strain distributions within the crystal play a critical role in the self-assembly, particularly with respect to the BZO nucleation site [25, 55]. This hypothesis produces an intuitive result in that the net strain is minimized (and thus a lower energy state is maintained) when nucleation and growth proceed at locations of lesser lattice mismatch. In other words, the BZO would preferentially grow on itself before nucleating elsewhere within the YBCO lattice. This strain-mediated mechanism is consistent with the observed self-assembly of BZO nanorods, but still leaves some question about the size and preferred direction of alignment of the inclusions. In this chapter, we will discuss the role of the surface strain distribution on the growth and alignment of the BZO nanorods and show experimental evidence of the effects by varying the vicinal angle of the growth surface.

3.1 Nanorod Formation in YBCO Thin Films: Review of Potential Mechanisms

With a relatively small average lattice misfit of -1.35% (defined here as $f = a_1 - a_2 / a_2$, where a_1 and a_2 are the film and substrate lattice parameters, respectively), YBCO grows *c*-axis oriented thin films with reasonably good epitaxy on $SrTiO_3$ (STO) substrates [56 – 57]. By definition, epitaxial thin films grow by following the structural template of the substrate, though the misfit between the two is an important factor determining the nature of the interface. For example, some misfit between the substrate and film may be accommodated by displacing the film atoms from their relaxed positions, thus straining the lattice. This is called coherent strain, but typically, the accommodation is limited to a certain film thickness [48]. Since the strain energy increases with volume, exceeding this critical film thickness makes it energetically more favorable to relieve the strain by the formation of misfit dislocations [48, 58]. The interfacial effects become even more important when second-phase dopants like BZO are added to YBCO films since misfit with the matrix is considerable. Typical values are summarized in Table 3-I, where the misfit to YBCO along the various crystallographic axes is listed for two commonly used cubic dopants. From these relatively high values, we may expect that a coherent YBCO/BZO interface would result in a highly strained lattice, or that a significant number of misfit dislocations would result. Reports of both increased average strain and the formation of aligned dislocations in YBCO films with self-assembled BZO nanorods have experimentally shown that the interfaces are probably

Table 3-I: Lattice mismatch values for common vortex pinning dopants with respect to YBCO along the three crystallographic directions. The [*003*] mismatch is shown since *c*/3 of the orthorhombic YBCO provides a closer match with the cubic structures. The values shown are calculated from the lattice parameters listed in Powder Diffraction Files published by the International Union of Crystallography.

	Misfit to *YBCO* lattice			
YBCO crystalline axes	*[100]*	*[010]*	$(a\text{-}b)_{avg}$	*[003]*
$BaZrO_3$ (PDF #03-0632)	8.85%	7.25%	8.05%	7.08%
$BaSnO_3$ (PDF #15-0780)	7.22%	5.59%	6.41%	5.42%

a more complex combination of coherent and incoherent strain [25, 59]. This strain-mediated consideration does however give some insight to the favorability for BZO growth at positions where nucleation has already occurred. The minimization of strain would then imply that to some extent, segregation or accumulation of species would be energetically preferred. Because the average misfit between YBCO and BZO in the *a*-*b* plane is slightly larger than the misfit along the *c*-axis (~8.1% vs. ~7.1%), the cylindrical shapes of the inclusions would be consistent with this argument since the interfacial area of highest strain is minimized. This would also be consistent with the larger nanorod diameters observed in $BaSnO_3$ (BSO)-doped YBCO films (9 – 12 nm as compared to 5 – 7 nm for BZO), because of the lower average in-plane misfit of ~6.4% [26, 40]. Examples of typical BZO and BSO doped YBCO films are illustrated by the cross-sectional TEM images in Figure 3.1. Although lower than BZO, the average *a*-*b* misfit of BSO is still larger than along the

c-axis, which, by the reasoning above, would favor high aspect-ratio geometries like the observed cylindrical rods.

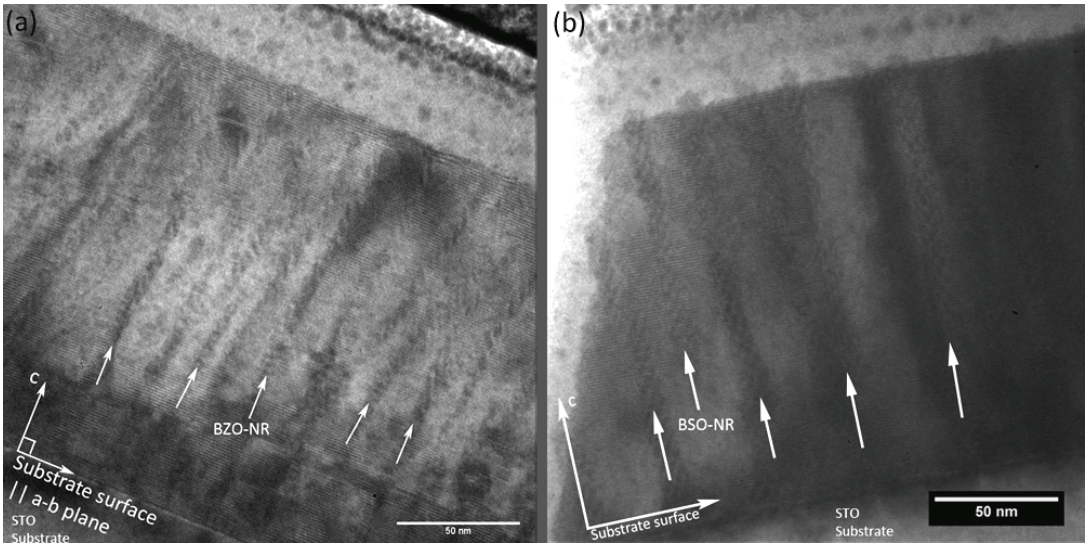

Figure 3.1: Cross-sectional TEM images of YBCO films doped with (a) 2 vol. % BZO, and (b) 4.5 vol. % BSO. Examples of the self-assembled nanorods are marked with arrows, and the scale bars indicate 50 nm.

Calculations of the strain energy have shown that, assuming coherent cylindrical inclusions, the interaction would produce a YBCO matrix under mechanical shear, while the BZO or BSO are under compressive strain [60].

Similar self-aligned structures have been reported in other oxide systems, including, for example, vertically aligned arrays of multiferroic $BiFeO_3$ (BFO) alternating with Sm_2O_3 (SmO) columns [61]. In this case, several conditions were attributed to the vertical (along growth direction) alignment, including the balance between the substrate/film strain and the strain of the interfaces of the film constituents. Here, the SmO has negligible misfit with the STO substrate and ~2.57%

misfit to the BFO. The misfit between BFO and STO is ~ -1.46%, so the coherently strained region is expected only at the BFO/STO and BFO/SmO interfaces [61]. The authors suggest that a condition for alignment is that the area of interface between vertical features must exceed that with the substrate (this area would increase with the film thickness during growth). Thus, for films less than a critical thickness, the strain due to the substrate/film interface would dominate that of the BFO/SmO interfaces. Indeed, measurements of the *c*-axis lattice parameter show that the SmO transitions from compressive to tensile strain after a film thickness of ~20 nm, indicating the tensile strain of the positive misfit with BFO may overtake the compressive effect of the substrate beyond this thickness [61]. Again, the interfaces are assumed to be coherent, however the occurrence of misfit dislocations were reported and assumed to relieve some of the strain [61]. Other accounts of self-assembled structures in magnetic oxides also consider the influence of the substrate/film interface, where the tensile strain on $La_{0.67}Ca_{0.33}MnO_3$ (LCMO) induced by an MgO substrate (f ~ -8%) forms pyramid-shaped inclusions [62]. Similarly, composite films of $(La_{0.67}Ca_{0.33}MnO_3)_{0.5} + MgO_{0.5}$ on MgO substrates formed domains of LCMO in a matrix of MgO, where similar tensile strain is observed. However, in this case, few dislocations are reported, and strain accommodation is attributed to crystalline phase transformations [62]. Other reports have shown comparable structures form in other oxide compositions, though following a common theme of strained interfaces [63 – 65]. While the structural mechanisms have not been considered in detail for each system, we may gather from these accounts that analogous strain-mediated

mechanisms are probably responsible for their formation. Thus, in the sense that the doped YBCO films are comparable ceramic oxides (even sharing the perovskite structure of some of the composites considered), it appears reasonable to take strain-mediated growth as a likely mechanism. However, the direction of alignment of the inclusions may not be fully described by this approach since only the role of the substrate and film interfaces have been considered so far. As we discuss next, the surface energies at the substrate and within the film may also play a significant role, especially on the nanorod alignment.

3.2 Surface Energies and Vicinal Surfaces

While columnar defects provide high pinning force per unit length, the degree of misalignment, or splay, is also an important factor in creep rate and thus influences the overall $J_c(H)$ behavior (see Chapter 1). Therefore, to maximize performance in applications where loads require sustained high currents, we must maintain some level of control over the direction of alignment of the self-assembled nanorods within the film. This would allow for maximum control over the defect landscape and provide a means toward a vortex pinning structure that could be tuned to the design requirements of the specific application. We have introduced the important role that strained interfaces play in the formation of BZO, BSO and other nanostructures. However, the surface energies are closely related, and since a vicinal surface consists of a series of steps and terraces, the surface energy is inherently modulated [66]. By varying the angle of inclination of the terraces (miscut angle, as described below), we

may change the step density in a controlled fashion [67]. This provides a method to study the dependence of the nanorod alignment on the surface energy distribution as a means toward controlling the overall pinning landscape at the growth stage.

Nanostructured YBCO films present multiple pairs of interfaces, as schematically illustrated in Figure 3.2. In this figure, some interface pairs of interest

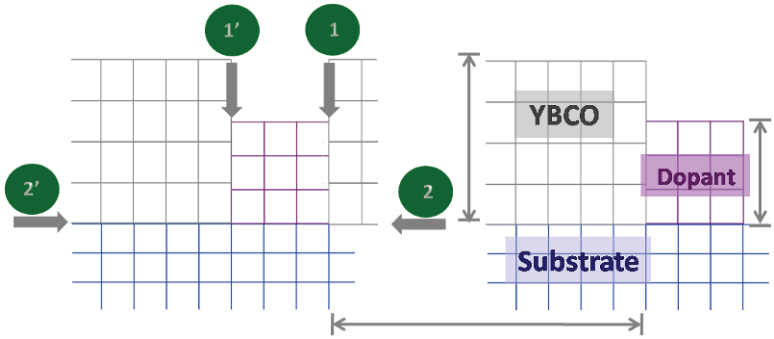

Figure 3.2: Schematic of interfaces in doped YBCO thin film on substrate. Interfaces between the YBCO matrix and BZO are labeled "1", and the interfaces between the surrounding YBCO and the substrate are labeled "2".

are pointed out, including the substrate/YBCO, YBCO/dopant (BZO, BSO, etc), and the dopant/substrate. Along with the misfit and strain, each interface presents a new surface that will influence the overall growth. In general, a surface maintains a higher energy state than that of the bulk material, and the spatial distribution directly influences where nucleation is preferable. For example, to produce a new surface in a bulk solid, work is required to break the bonds maintaining the crystalline structure. The surface energy per unit of new area exposed, or surface tension γ, is then defined as the amount of work required to create the new surface divided by the new area [66, 68]. While the surface energy distribution is a function of orientation, and may be

quite complicated, the simplest cases of low-index planes in highly symmetric crystal structures (e.g. cubic) are isotropic [69]. However, if the surface is parallel to a higher-index plane, such as for a bulk crystal polished at an angle with respect to the crystalline axes (miscut), a stepped surface with a modulated surface energy distribution is produced. This is characteristic of a vicinal surface, as illustrated in Figure 3.3 (a) from Ref. [70].

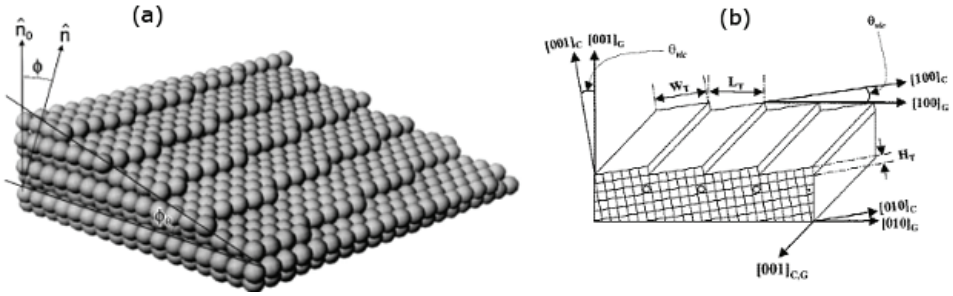

Figure 3.3: **(a)** Example of a vicinal (*3,2̄,16*) surface of a face centered cubic crystal [70], **(b)** example of vicinal surface by miscut away from [*001*] toward [*100*] [71].

Thus, a vicinal crystal gives a surface that is modulated both in morphology and in energy. The physical shape and surface energy are both functions of the vicinal (or miscut) angle. In the simple cases we will consider, this angle is measured from, say the [*001*] direction, toward only one of the orthogonal axes like [*100*] in a cubic crystal. This produces straight, parallel ridges on the substrate surface, as shown in Figure 3.3 (b) [71]. The modulated surface then gives a tunable parameter, the vicinal angle, that we may vary to study the defect formation and geometry, and thus attempt to produce a controlled vortex pinning landscape.

Previous studies have shown that YBCO films grown on STO with vicinal angles of 5° – 20° showed the formation of pores, that due to the sharp transition to the non-superconducting state, produce a strong vortex pinning response [72, 73]. The $J_c(H)$ dependence showed significant increase at low magnetic fields (< 1 T), but did not show the decrease at self-field generally observed in second-phase doped samples. However, the vortex pinning properties could also be further tuned to improve $J_c(H)$ at higher fields of ~2 T with the incorporation of Y_2BaCuO_5 nanoparticles, where both an increased pore density and the nanoinclusions provided pinning structures [73]. The formation of the pores has been attributed to a means of relieving the net strain accumulation due to the modulated growth surface. Indeed, we also saw that the morphology of the growth surface plays a significant role in the pore formation, as similar structures were produced in YBCO films deposited on substrates decorated with Y_2O_3 particles with comparable aspect ratios to the steps on a vicinal surface [74]. Thus, we have seen that the microstructural modification at the growth surface provides a means toward tailoring the vortex pinning structure. We then attempt to extend this technique to further control a landscape suitable for varied magnetic field intensities and orientations.

3.3 YBCO Thin Films and Nanorod Alignment on Vicinal Substrates

3.3.1 Experimental Details

YBCO films with 2 vol. % BZO were deposited via single-target pulsed laser deposition using a KrF laser with $\lambda = 248$ nm at an 8 Hz repetition rate. The

substrates were held at 800°C during the deposition, with an O_2 partial pressure of 300 mTorr. Films approximately 200 nm thick were grown on STO substrates with vicinal angles of 0° ("flat"), 5°, 10°, and 20°. The samples were patterned by photolithography, and transport properties were measured in the direction parallel to the vicinal steps via a four-point probe. Transition temperatures (T_c) were found by measuring the sample resistivity as it was cooled to 77 K in liquid nitrogen. To study the microstructural properties by TEM, cross sections were prepared using FEI Nova 600 NanoLab and DB235 focused ion beam systems. Care was taken to cut the cross-sectional foils perpendicular to the vicinal steps so that the effects of the modulated surface could be directly observed. The microstructures of the films were studied using a Philips CM200 and FEI Titan TEM using acceleration voltages of 200 and 300 kV, respectively.

3.3.2 Microstructural Results

Cross-sectional TEM images taken down the [*100*] axis (looking parallel to the vicinal steps) are shown in Figure 3.4, and illustrate the microstructures of the YBCO films doped with 2 vol. % BZO on STO substrates with vicinal angles ranging from 0° – 20°. For comparison, Figure 3.4 (a) shows a nonvicinal film with features that are consistent with those commonly observed in the literature [25, 55, 75]. In Figure 3.4 (a), nanorods 5 – 6 nm in diameter with an average splay of 5.3 ± 2.4° are visible by the contrast of the moiré fringes. Since the typical thickness of the electron transparent cross-section is 100 – 200 nm, and given the diameter of the nanorods, the

fringes result from interference patterns produced by the overlapping YBCO and BZO with mismatched lattice constants [50].

The 5° vicinal sample in Figure 3.4 (b) shows only slight microstructural change when compared to the nonvicinal film, and higher resolution images show that the YBCO *a*-*b* planes form roughly parallel to the vicinal terraces (measured as approximately 4.1° from the nonvicinal [*010*]). At increased magnification, the high-resolution TEM image in Figure 3.5 shows an example of the inclination of the *a*-*b* planes. The BZO nanorods show a slight average misalignment of approximately 9.7 ± 3.1° from the tilted *c*-axis, which happens to be a comparable splay to that reported by Civale et al. for high energy Sn irradiated YBCO [28]. Therefore, from the increased columnar splay in the vicinal film, we may expect increased vortex entanglement and a corresponding increase in the in-field J_c resulting from the reduced vortex creep. However, the splay observed at this vicinal angle is also is approaching the maximum angles considered beneficial for reducing vortex hopping, indicating a further increase would not be expected to produce further improvement [76]. The reduced *c*-axis alignment (increased splay) of the nanorods does, however, give a preliminary indication that the modulated surface of the vicinal substrate is influencing the microstructural evolution through the ~250 nm thickness of the film. We have also observed the increased splay to persist up to 1 μm film thickness, showing the effects are not limited to the nucleation phase at the substrate level [77].

The highly defective YBCO microstructure of the 10° sample, with a significant occurrence of stacking faults, is shown in Figure 3.4 (c). These types of structural defects have been reported for pure YBCO growth on vicinal substrates, which will be discussed further in this chapter [78]. However, the high density of stacking faults observed here shows that the effect appears to be exaggerated, also indicating the extended nature of the defect structure initiated by the vicinal surface. The increased defect density may also show that a mechanism of strain accommodation is initiating, implying that otherwise the net strain of the matrix would increase with increasing vicinal angle. Additionally, the continuity of the BZO nanorods through the film thickness is reduced, implying that the $H \parallel c$ vortex pinning may be slightly diminished by the reduction in total pinning force.

A more drastic microstructural change is observed in the 15° – 20° vicinal films shown in Figure 3.4 (d) – (e). At these angles, the BZO nanorod alignment is significantly influenced. The 15° vicinal sample shows some nanorods rotated roughly 90° such that their axes are oriented nearly parallel to the YBCO *a*-*b* planes. In the 20° sample of Figure 3.4 (e), the nanorods become fully aligned in the *a*-*b* plane, showing that the alignment direction appears to undergo a transformation that completes by this vicinal angle. In addition, the diameter of the nanorods is increased to approximately 10.8 ± 1.5 nm, nearly twice the diameter of those in the nonvicinal films. It is also notable that as the vicinal angle is increased from 10° to 20°, the density of stacking faults diminishes significantly. The reorientation of the BZO nanorods with increased miscut angle further suggests that the microstructural

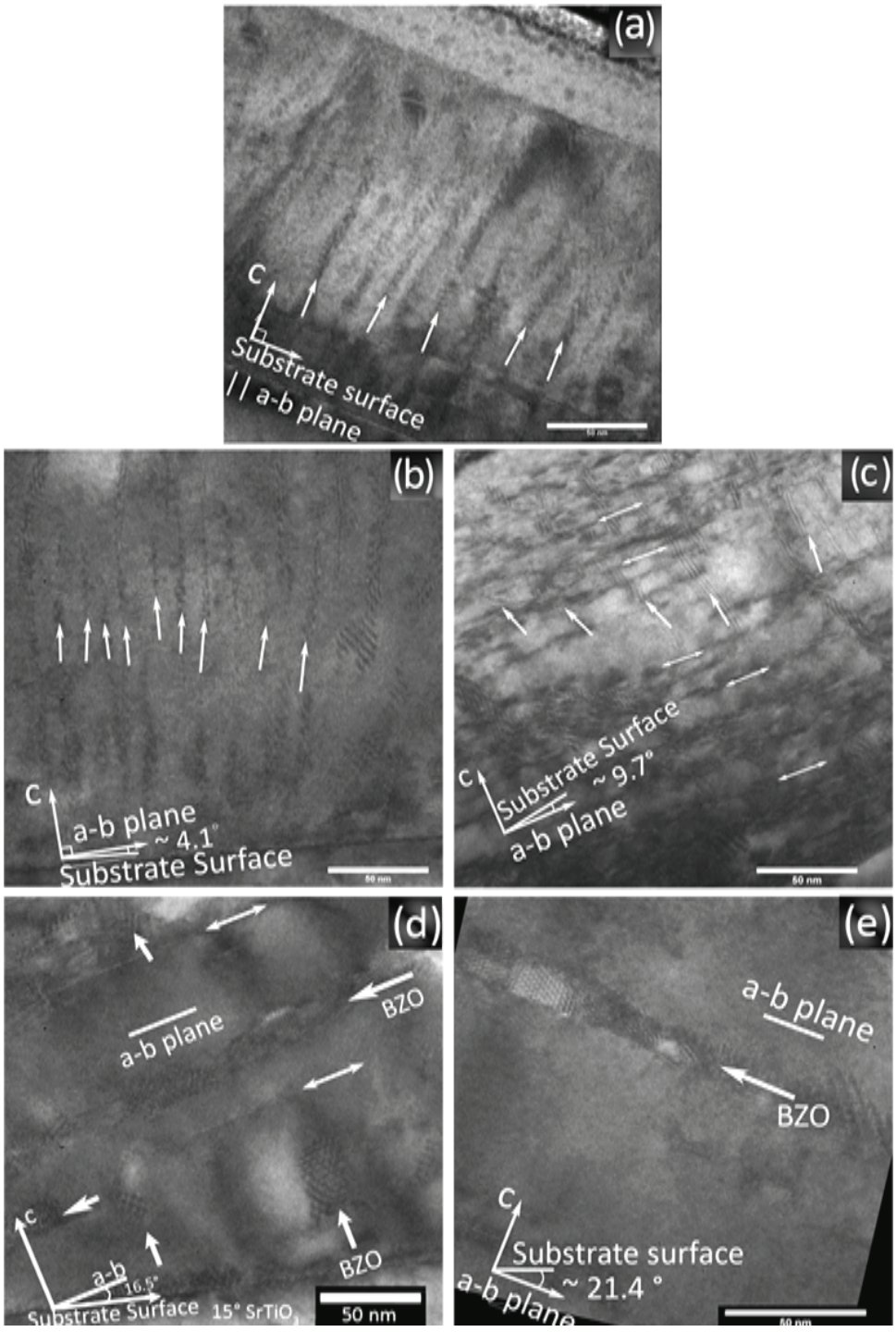

Figure 3.4: Cross-sectional TEM images of YBCO films with 2 vol. % BZO grown on (a) nonvicinal, (b) 5°, (c) 10°, (d) 15°, (e) 20° STO substrates. The single-ended and double-ended arrows point to examples of self-assembled nanorods and stacking faults, respectively. The scale bars indicate 50 nm.

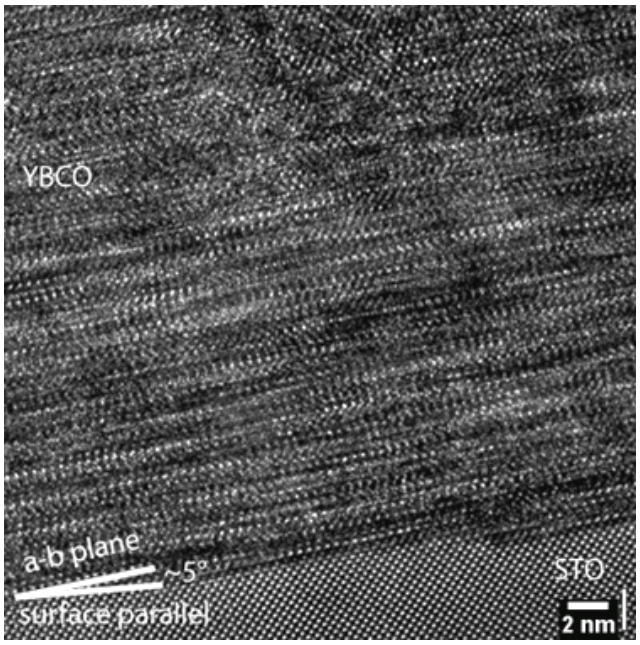

Figure 3.5: High-resolution cross-sectional TEM image of BZO-doped YBCO on 5° vicinal STO. The inclined a-b planes of the YBCO with respect to the macroscopic substrate surface, as well as a substrate terrace/step are visible.

conditions that dictate their direction of alignment are strongly linked to parameters influenced by the vicinal growth surface. The modulated surface energy of the vicinal substrate clearly adds additional degrees of complexity to the strain relationships between the nanorods and the YBCO matrix. For this reason, it is beneficial to first consider the growth of single-phase YBCO films on vicinal substrates, from which it may be possible to extend some conclusions about the microstructure of the doped films.

3.3.3 Growth Mechanisms on Vicinal Substrates

The morphology of YBCO thin films grown on vicinal surfaces changes significantly, reflecting the modulated surface of the substrate, when compared to that

on nonvicinal surfaces [67, 71, 78]. Examples of surface images of YBCO films on 1.2° vicinal and nonvicinal STO substrates are shown in Figure 3.6 (b) and (c), respectively (from Refs. [67, 78]). The ridged surface morphology of the vicinal

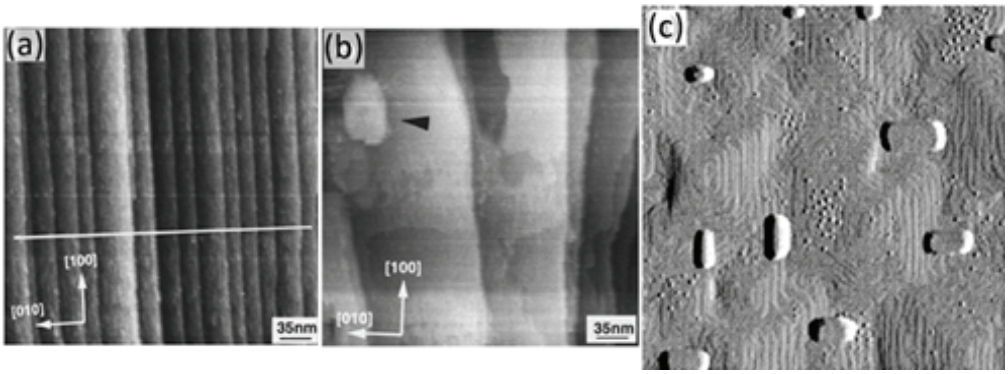

Figure 3.6: AFM images of (a) 1.2° vicinal STO before deposition, (b) the surface of 120 nm thick YBCO film on the 1.2° vicinal substrate, (c) YBCO film on nonvicinal STO (*001*). (a) – (b) from Ref. [78], (c) from Ref. [67].

STO is exaggerated by the YBCO film, which shows the significantly wider terraces seen in Figure 3.6 (b). By comparison, the surface of the nonvicinal YBCO in (c) shows spiral patterns commonly observed. The change in morphology indicates a probable change of growth modes in the vicinally grown films. This is not unexpected since the growth mode of thin films is strongly dependent on the relative balance of the individual surface tensions of the substrate, film, and substrate-film interface [48]. Three common growth modes are illustrated in Figure 3.7, which shows examples of (a) Island, (b) Layer plus Island, and (c) Layer growth [68]. On nonvicinal substrates of relatively low mismatch, such as STO, $LaAlO_3$ and MgO, YBCO thin films initiate via island growth [78 – 80].

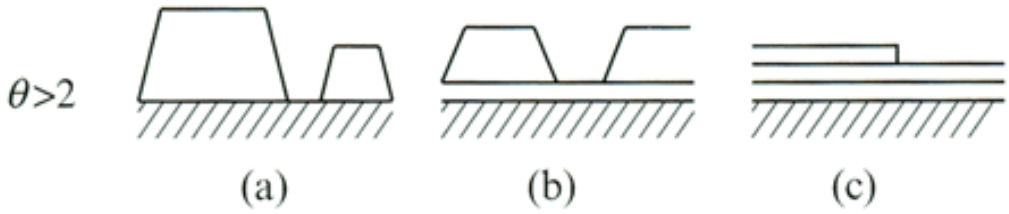

Figure 3.7: As shown in Ref. [68], the (a) Island (Volmer-Weber), (b) Layer plus Island (Stranski-Krastanov), (c) Layer (Frank-Van der Merwe) growth modes.

The images in Figure 3.6 are an example of experimental evidence that has shown that YBCO growth transitions from island nucleation on nonvicinal substrates to step-flow mode on vicinal STO [56, 67, 78]. In this case, the higher surface energy makes nucleation at the steps more favorable, causing growth to proceed from the edges until finally overgrowing the terraces, as illustrated in Figure 3.8 from Ref. [34].

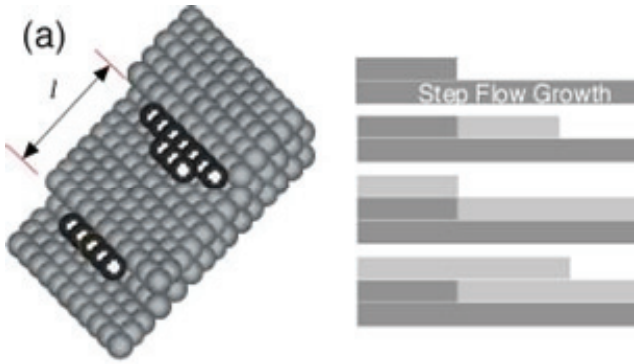

Figure 3.8: Illustration of step-flow growth on a vicinal surface from Ref. [34].

Given adequate surface diffusion, this mode is comparable to layer growth for epitaxial films since continuous coverage precludes the nucleation of islands within the terrace [34]. Thus, the film is less likely to develop defects when compared to island growth. However, Haage, et al. observed the formation of stacking faults

(planar defects) coinciding with the surface steps in YBCO thin films grown on vicinal STO [78]. As illustrated in Figure 3.9, these defects were associated with antiphase boundaries that result when the height of the vicinal steps does not match with a block of the layered unit cell, and are thus a product of the slight mismatch and heteroepitaxial growth of YBCO on vicinal STO [78]. Therefore, we see that the formation of strain-dependent inclusions like BZO or BSO nanorods may be influenced by the vicinal substrate since the strain distribution would already be modulated by the dislocations occurring at regular intervals (coinciding with steps).

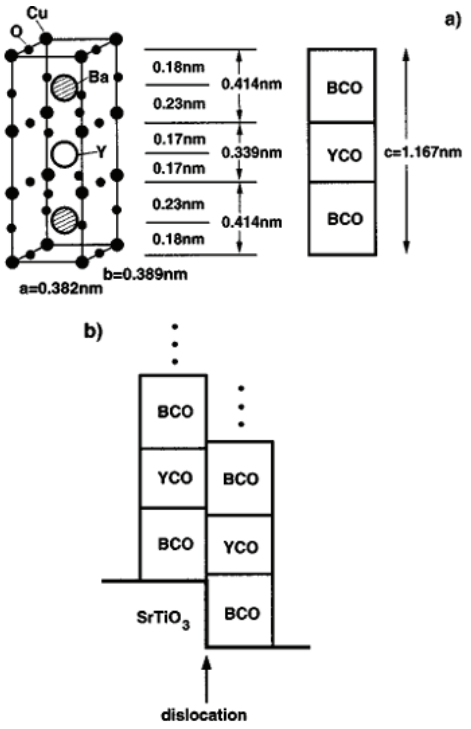

Figure 3.9: From Ref. [78], the layered YBCO unit cell may be considered as three nearly cubic cells. If the height of the vicinal surface steps does not coincide with the size of a component cell, a dislocation results.

As was discussed in the review of magnetic oxide nanostructures, the contact area is important in determining the extent of strain accumulation [61 – 62]. This is also relevant to the nucleation of YBCO on vicinal STO since the terrace widths on the vicinal surface decrease with increasing miscut angle (proportional to $1/tan(\theta_{vic})$) [67]. Consequently, for higher vicinal angles, the ratio of contact area between the film and terraces to that of the film and steps decreases. Since, as illustrated in Figure 3.9, defects may be introduced at each step interface, as the vicinal angle increases, the proportion of the YBCO matrix subject to the step-induced defects will also increase. Therefore, with an increased defect density, we may expect the effects on BZO nanorod growth to become more significant as the vicinal angle increases. Indeed, previous studies have found that for undoped YBCO grown on vicinal STO, the *c*-axis parameter contracts with increasing vicinal angle [81 – 82]. If the YBCO is under compressive strain in the vertical (*c*-axis) direction, a tensile strain in the *a*-*b* plane would result. This would then reduce the anisotropy of the misfit between the YBCO and BZO, which we have attributed to the columnar shape of the BZO nanorods.

Some evidence of this increasing effect with vicinal angle was observed in the BZO-doped YBCO. As shown in Figure 3.4, the 2 vol. % BZO-doped film on 10° vicinal STO showed significantly distorted lattice planes when compared to that on the 5° STO. This may indicate that matrix strain is increasing with the increased vicinal angle while the nanorods are still *c*-axis aligned. The matrix distortion

appears to diminish, however, upon the transition to *a*-*b* aligned nanorods, indicating the tensile strain on the *c*-axis may relax in this configuration.

Measurements by x-ray diffraction of the BZO-doped YBCO are consistent with this observation, which showed a compressive strain in the *c*-axis direction that relaxes with the *a*-*b* realignment, as shown in Table 3-II [54]. On nonvicinal STO,

Vicinal Angle	*0°*	*5°*	*10°*	*20°*
c-axis (Å) 2 vol. % BZO-doped YBCO	11.82	11.56	11.55	11.73

Table 3-II: c-axis lattice parameter of 2 vol. % BZO-doped YBCO with vicinal angle as measured by X-ray diffraction [54].

the *c*-axis of the YBCO is stretched, as expected from the larger lattice parameter and *c*-axis alignment of the BZO nanorods. The contracted *c*-axis on the 5° – 10° samples shows behavior comparable to that reported for undoped YBCO, and thus reduces the misfit anisotropy between the YBCO and BZO. This makes the *c*-axis misfit comparable to the *a*-*b* misfit, which may provide less confinement to vertical alignment, and would contribute to the added splay observed in the 5° – 10° vicinal angles. That the *c*-axis parameter remains nearly constant from 5° to 10° is consistent with the observed lattice distortion observed in the TEM images of Figure 3.4, if the added strain of the increased step contact area is instead accommodated by dislocation and defect formation. Further evidence of this is seen in Figure 3.10, which shows a high-resolution image of the 2 vol. % BZO-doped film on a 10°

vicinal substrate. The cross-sectional image shows a disturbed YBCO lattice surrounding the BZO nanorod, and several of the planar defects previously noted are visible. The marks on the figure show examples of observable dislocations spaced on average ~4.2 nm apart, but separated by ~14 nm of uniformly structured matrix, thus increasing the overall average spacing to approximately 9.1 nm. While dislocations are expected given a mismatched interface, the spacing between dislocations, *D*, should roughly follow the relationship, $D = \frac{(\bar{a})^2}{a_1 - a_2}$, where $\bar{a}$ is the average of the

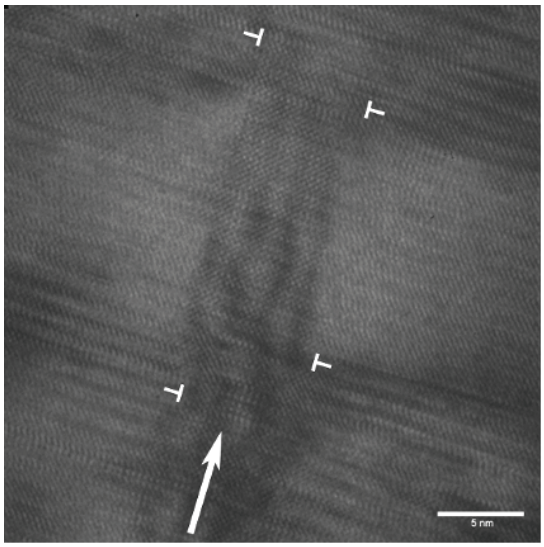

Figure 3.10: TEM cross-section of YBCO film with 2 vol. % BZO on 10° vicinal STO substrate. The arrow points to a BZO nanorod, and the markers indicate dislocations in the surrounding matrix. The scale bar indicates 5 nm.

lattice parameters a_1 and a_2 of the two materials [58]. Treating YBCO as a trilayered cubic, for the nonvicinal YBCO/BZO interface, the average dislocation spacing would be approximately 5 – 6 nm [60, 78]. An increased spacing between

dislocations would then increase the net misfit strain, which is consistent with the maintained contraction of the *c*-axis at this angle.

The abundance of structural defects at the 10° vicinal angle indicates the YBCO is approaching a threshold for strain accommodation. Therefore, a further contraction of the *c*-axis by increasing the vicinal angle may then invert the misfit anisotropy, putting the *a*-*b* plane under tensile strain, and making this direction energetically favorable for BZO growth. However, the x-ray diffraction data show the YBCO *c*-axis parameter is relaxed to nearly its bulk value at the 20° vicinal angle. This is not unreasonable though, since now a significant proportion of the YBCO/BZO interface is along the *a*-*b* planes. Therefore, although the misfit anisotropy now favors growth along the *a*-*b* planes, the larger contact area between the mismatched lattices is also along this plane. The relatively large average spacing of 50.8 nm between nanorods (measured in the *c*-axis direction) is roughly ten times the length scale over which dislocations would be expected to relieve the misfit strain. Therefore, the geometry provides the necessary volume of YBCO over which to distribute the misfit strain, relax the lattice, and thus increase the average *c*-axis length measured by X-ray diffraction (XRD) [54]. At this angle, the overall reduced misfit may also produce the larger nanorod diameters because of the reduced strain that constrains the nucleation size.

3.4 Superconducting Properties of Vicinal BZO-Doped YBCO

The microstructural modifications have a direct effect on the flux pinning properties of the films as evident in Figure 3.11, which shows the critical current density vs. applied magnetic field parallel to the YBCO *c*-axis at 77 K.

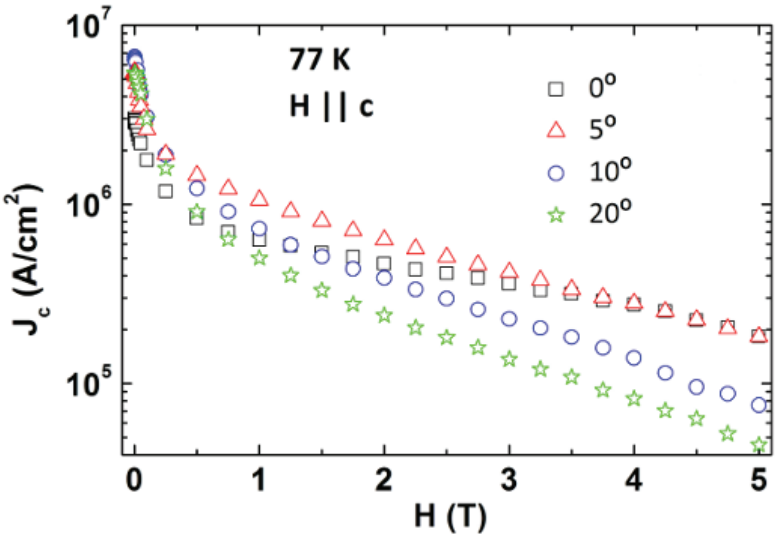

Figure 3.11: $J_c(H)$ of 2 vol. % BZO-doped YBCO on vicinal STO measured at 77 K with the applied magnetic field parallel to the *c*-axis. Curves are shown for four vicinal angles (0° – 20°) [54].

In this figure, each curve corresponds to a vicinal angle from 0° – 20°, and the open squares show the nonvicinal sample. It is noteworthy that the ~86.1 K T_c of the film on the nonvicinal substrate shows the typical reduction seen in BZO-doped YBCO, while that of the samples on the vicinal substrates range from 88.3 – 89.2 K. The mediated T_c in the vicinal samples may be due to the *c*-axis variation described previously, but will be discussed in more detail in the next chapter. In Figure 3.11 we see that the 5° sample shows an overall increase of $J_c(H)$ up to approximately 4.7 T.

Since the magnetic field is applied in the *c*-axis direction, this improvement in the low-to-moderate applied magnetic field range is consistent with the defect structure shown in Figure 3.4, and may be attributed to the increased splay of the BZO nanorods (and reduced vortex creep) at this vicinal angle. This is also consistent with similar increases observed in ion-irradiated YBCO for doses less than the matching field [28]. As the vicinal angle is increased, the increase in $J_c(H||c)$ occurs at lower field intensities, indicating the reduction in BZO nanorods aligned in this direction. Specifically, at 10° an increased J_c is measured up to ~1.3 T, while at 20° there is only a slight increase of $J_c(H||c)$ up to ~0.6 T. These $J_c(H||c)$ behaviors are in agreement with the observed defect structure in Figure 3.4, since the alignment of the nanorods broadened away from the *c*-axis and toward the *a-b* plane of the YBCO above the 10° vicinal angle. This is verified by the $J_c(H||a\text{-}b)$ curves shown in Figure 3.12, where an overall increase is seen for the vicinal samples through the measured range of 5 T. The largest increase in $J_c(H||a\text{-}b)$, maximized at approximately 0.5 T, is seen in the 10° sample. Given the high density of planar defects at this vicinal angle, the H || *a-b* behavior is not surprising. The $J_c(H||a\text{-}b)$ of the 20° sample is also increased overall, with the most improvement for fields less than 1 T. This improvement at lower H is consistent with the increase in average spacing between nanorods observed in the cross-sections. The distance between adjacent nanorods increases from approximately 25.4 nm in the 10° sample to roughly 50.8 nm in the 20° sample (which also accounts for the larger nanorod diameters), thus the matching field is correspondingly reduced.

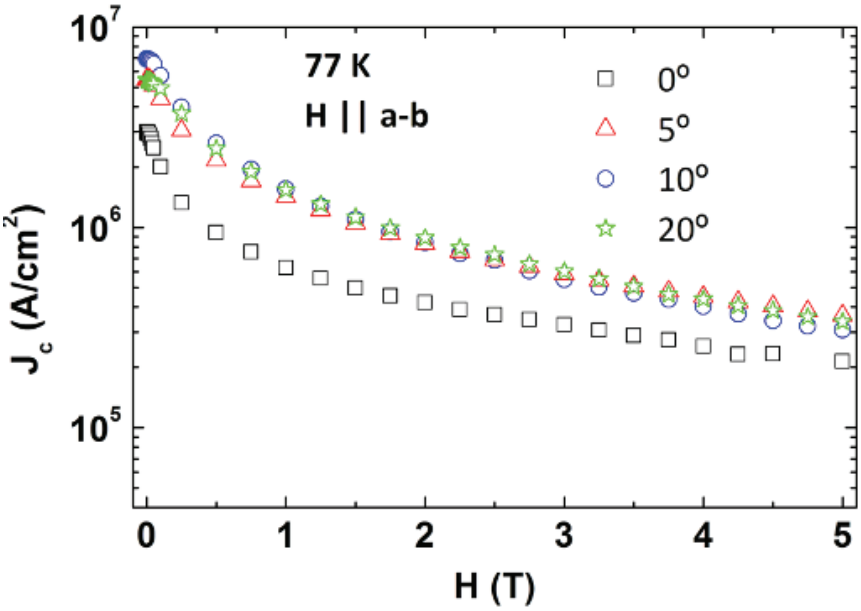

Figure 3.12: $J_c(H)$ of 2 vol. % BZO-doped YBCO on vicinal STO measured at 77 K with the applied magnetic field parallel to the *a*-*b*-plane [54].

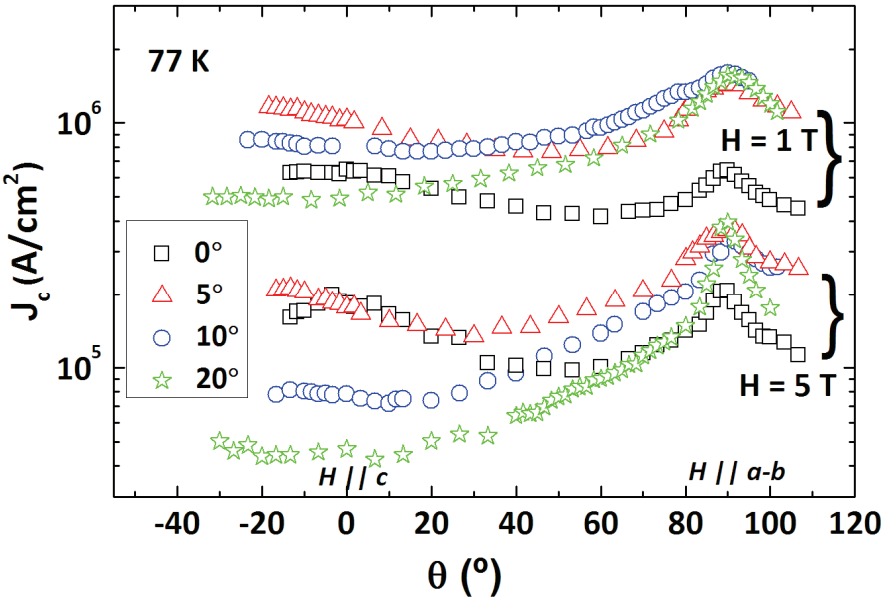

Figure 3.13: J_c of 2 vol. % BZO-doped YBCO as a function of the angle of incidence of the applied magnetic field for H = 1 T and H = 5 T [54].

A clear picture of the J_c dependence with the modified defect structure is shown by varying the angle of incidence at which the magnetic field is applied. This shows the geometric effects of the modified pinning landscape, and measurements at 1 T and 5 T magnetic fields are shown in Figure 3.13. Here we see that by varying the surface modulation, a range of vortex pinning behavior is produced. For example, the 5° sample gives increased values of $J_c(\theta)$ for $H \parallel c$ at 1 T when compared to the nonvicinal film, while at 5 T these peaks are nearly equal. Again, the $H \parallel c$ pinning behavior of the splayed BZO nanorods in the vicinal film is consistent with that attributed to reduced vortex hopping in the splayed ion damage tracks in irradiated YBCO for applied magnetic fields less than the matching field [28]. The set of curves at the 1 T magnetic field show $J_c(\theta)$ is increased over a broad range of angles, with the widest increase about $H \parallel a$-b in the 10° vicinal sample. On the other hand, the 20° sample peaks strongly about $H \parallel a$-b, but diminishes around $H \parallel c$. These results agree very well with the observed microstructure, given that the BZO nanorods show a general trend of increased splay at the lower vicinal angles (5° – 10°) and begin an orthogonal realignment at higher angles (15° – 20°). The more continuous, longer length nanorods at the 5° vicinal angle may account for the more rapid increase in $J_c(\theta)$ at $H \parallel c$, as compared to that shown for the 10° vicinal sample. Because of the increased pinning through the thickness of the film, a higher net pinning force would be expected at the 5°, producing the slightly sharper peak observed in Figure 3.13

3.5 Conclusions

The growth of second-phase nanorods (BZO, BSO, etc.) in YBCO thin films is most likely a strain-mediated process by which an anisotropic strain distribution leads to a favorable alignment direction. We have seen that interfacial and surface effects at the substrate and film level can significantly alter the alignment and uniformity of the inclusions. This growth-initiated control of the defect geometry provides a means toward producing a vortex pinning landscape that ideally may be tuned to a specific application to provide optimal performance. By varying the surface strain distribution via the vicinal angle, we have shown a range of tailored BZO nanorod alignments. At low angles (5° – 10°), we observed an increased splay in the *c*-axis aligned nanorods. While at higher angles (15° – 20°) a transition to an orthogonal *a*-*b* alignment was shown. The different geometries produced vortex pinning structures that improve the $J_c(H)$ and $J_c(\theta)$ over several regimes, including significantly broadened peaks for $H \parallel c$ (in the 5° sample) and for $H \parallel a$-b in the 10° sample.

Since the strain distribution at the growth surface, as well as within the film, is important in the growth and alignment of nanorods, the degree of mismatch is a parameter that may be experimentally varied. In addition, the net strain within the lattice is directly affected by the formation of dislocations. Therefore, we may also expect the mismatch and the inter-nanorod separation (dopant concentration) to influence the nanorod alignment and growth, and we examine these effects next.

Chapter 4

Effect of Dopant Concentration and Lattice Parameter on Nanorod Alignment and Microstructure

We have seen that the controlled growth of the defect structure in YBCO films provides a means of producing a tailored vortex pinning landscape. We may imagine then that the $J_c(H)$ performance demanded by specific applications could be addressed through design of the thin film growth. If increased magnetic field intensity is one of these demands, an increased number density of defects is necessary to avoid depinning by vortex-vortex interactions (see Chapter 1). For example, this was shown in irradiated YBCO by simply increasing the ion flux, thus increasing the density of damage tracks, and the $J_c(H)$ at higher fields [83]. Analogously, a simple solution to this vortex pinning problem using self-assembled nanorods is to increase the amount of dopant infused in the matrix. For example, Traito, et al. showed that by increasing the concentration of BZO from 2.9% to 9% (by weight), the density of nanorods increased from approximately 1300 μm^{-2} to 4200 μm^{-2} [84]. The density of BSO nanorods was shown to change similarly by increasing the dopant concentration [40]. As expected, $J_c(H)$ is improved for magnetic fields up to the matching fields value, but another problem is introduced since the T_c is generally reduced by several Kelvin with increased doping [32, 84]. The change in T_c is less pronounced in BSO-doped YBCO than with BZO-doped YBCO, which has been attributed to effects of chemical contamination as well as a possible strain-induced reduction [25 – 26, 85].

An additional complexity is introduced by increasing the dopant concentration since, as previously discussed, the strain in the matrix surrounding the inclusion plays a critical role in the anisotropic misfit that guides the nanorod alignment. We would also expect that increasing the number of nanorods in the YBCO matrix would influence the overall strain distribution since this would reduce the spacing between adjacent nanorods. For example, if the inter-rod separation were decreased below the critical thickness for dislocation formation, we would expect the matrix strain to correspondingly increase until crossing the threshold over which a coherent interface may be accommodated . We saw a similar effect in the vicinal BZO-doped YBCO films, which then promoted the realignment of the nanorods (Chapter 3). The misfit between the dopant and YBCO would similarly affect the strain distribution. As shown in Table 3-I, the misfit between YBCO and BSO is smaller than that of BZO with respect to all three lattice parameters, so the matrix strain should be reduced when compared. For the same reason, we may again expect the BSO nanorod alignment to vary in the vicinal films compared to that for BZO-doping. We examine this experimentally by varying the BZO concentration (nanorod spacing) and by investigating the alignment in BSO-doped YBCO (lattice/dopant misfit) films grown on vicinal STO substrates.

4.1 Experimental Details

To study the inter-rod spacing, the dopant concentration was varied by increasing the volume fraction of BZO in the YBCO ablation target to 2%, 4%, and

6%. The powders were mixed, pressed into 2.5 cm cylindrical targets and sintered, as described in Chapter 2. Thin films were deposited by PLD using the same parameters described in Chapter 3, with separate depositions for the 2% – 6 vol. % samples using the respective targets and a growth temperature of 810°C. Samples used to study the nanorod misfit were fabricated by the same method, except the BSO powder was mixed in to the target by molar, as opposed to volume, concentration. In this case, 10 molar % BSO was added. Converting to volume fraction gives a concentration of approximately 4.5 vol. %, which will be referenced through the rest of this chapter. TEM cross-sections were prepared by a Focused Ion Beam technique, using the same procedure previously described.

4.2 Microstructural Results

4.2.1 $BaZrO_3$ Doping Concentration

For comparison, cross-sectional TEM images (along [*010*] or [*100*]) of YBCO films doped with 2%, 4% and 6% BZO by volume deposited on nonvicinal STO substrates are shown in Figure 4.1. From measurements over multiple regions from each sample (for a total of 60 – 90 measurements per sample), the average linear spacing between visible nanorods decreases from approximately 10.8 nm to 4.4 nm

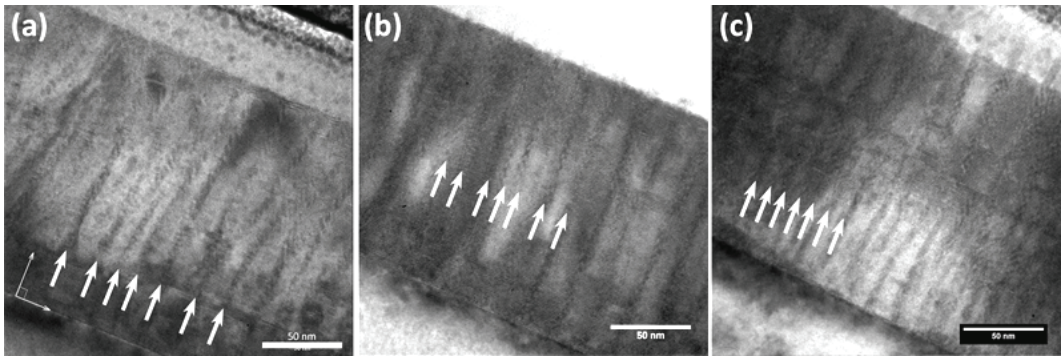

Figure 4.1: Cross-sectional TEM images of nonvicinal YBCO films doped with (a) 2 vol. %, (b) 4 vol. %, (c) 6 vol. % BZO. Examples of adjacent nanorods are marked with arrows, and the scale bar indicates 50 nm.

when the BZO concentration is increased from 2 vol. % to 6 vol. %, and shows a very slight increase in the average diameter. These average values are listed in Table 4-I, where the reported deviation incorporates variations in the measured diameter and spacings. It should be noted, however, that the spacing values were measured edge-to-edge for adjacent nanorods in the cross-section. Since the foil is 100 – 200 nm thick, then depending on the geometric arrangement of nanorods within the film (e.g. square lattice), the apparent edge-to-edge spacing in the cross-section may be shorter than the separation in the plane of the film.

Table 4-I: Average nanorod parameters measured from cross-sectional images of *nonvicinal* BZO-doped YBCO films.

BZO vol. concentration	*2%*	*4%*	*6%*
Nanorod spacing (nm)	10.8 ± 3.2 nm	6.0 ± 2.7 nm	4.4 ± 0.7 nm
Nanorod diameter (nm)	5.2 ± 0.5 nm	5.8 ± 0.6 nm	5.9 ± 0.9 nm

The increased nanorod density at higher doping levels would, however, imply higher matching fields and increased $J_c(H)$ at higher fields. In addition, the slightly larger nanorod diameters at 4 – 6 vol. % may give a preliminary indication of the lateral strain influencing their size, as discussed in more detail in this chapter.

The samples grown on the 5° vicinal substrates behave much differently at increased BZO concentrations. Figure 4.2 (a) – (c) shows cross-sectional TEM images of YBCO films doped with 2 – 6 vol. % BZO. In this figure, we see that at 5° most of the nanorods are aligned parallel to the *a*-*b* plane at 4 vol. %, showing that the orthogonal realignment is more favorable at much lower vicinal angle than in the 2 vol. % BZO-doped samples (which realigned at 15 – 20°). Some *c*-axis aligned nanorods are still visible in the 4 vol. % films (a few examples marked by vertical arrows), but increasing to 6 vol. % shown in Figure 4.2 (c), the transition to *a*-*b* alignment appears complete. Interestingly, the average diameter of the *a*-*b* aligned nanorods, measured over multiple images and locations, ranges from approximately 5.4 – 6.6 nm in the 4 – 6 vol. % BZO-doped samples. This is nearly half the diameter of the ~10.7 nm *a*-*b* aligned nanorods observed in the 2 vol. % BZO-doped samples at the 20° vicinal angle (Figure 3.5). This may also give an indication of the strain state of the matrix surrounding the nanorods, since we attributed the increased diameter to a net reduction of the misfit between the YBCO and BZO. In this case, the contracted YBCO *c*-axis caused by the 5° vicinal angle in combination with the

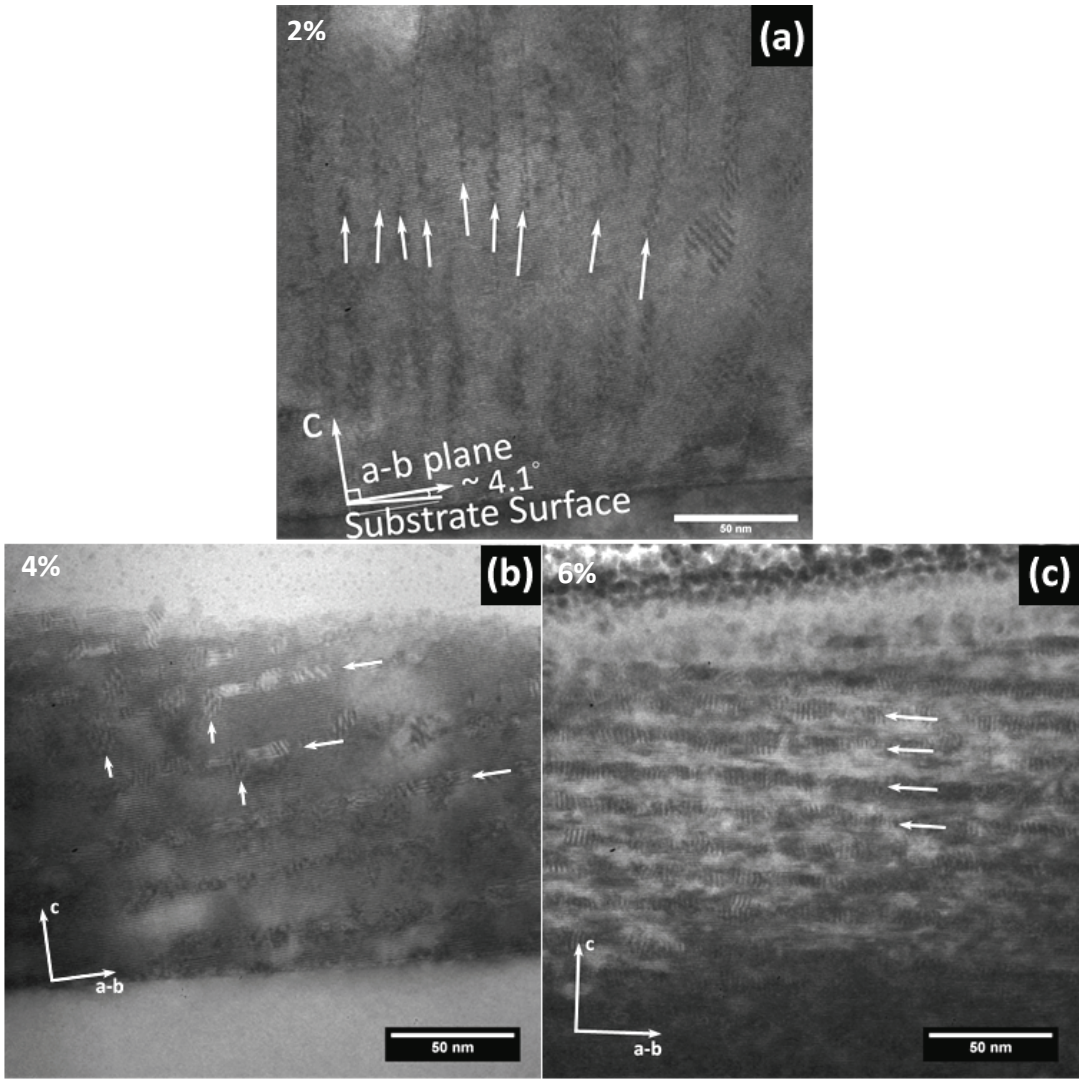

Figure 4.2: Cross-sectional TEM images of YBCO films grown on 5° vicinal STO, doped with (**a**) 2 vol. %, (**b**) 4 vol. %, and (**c**) 6 vol. % BZO. Vertical arrows show examples of *c*-axis aligned nanorods, while the horizontal point out the *a*-*b* alignment. The scale bars indicate 50 nm.

increased strain from the increased BZO concentration may cause the misfit anisotropy to favor *a*-*b* aligned growth at significantly lower vicinal angles. The high-resolution images in Figure 4.3 also indicate the increased strain interaction with

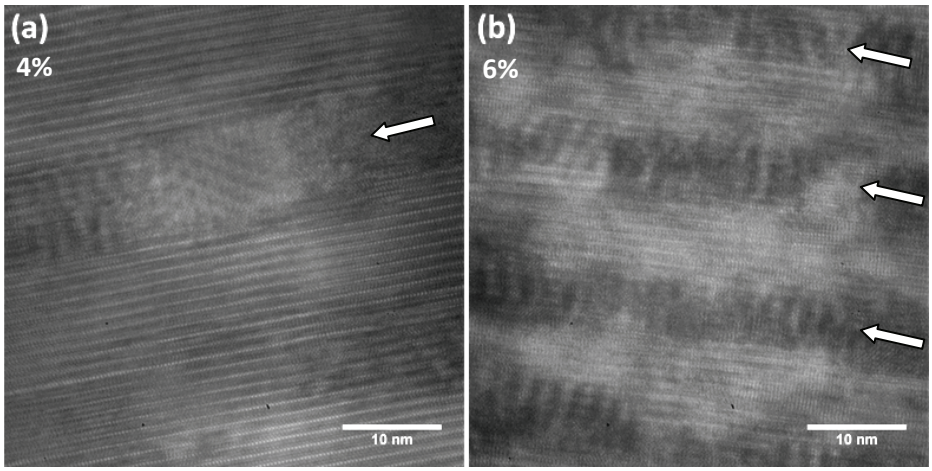

Figure 4.3: High-resolution cross-sectional TEM image of samples in Figure 4.2: (**a**) 4 vol. %, and (**b**) 6 vol. % BZO-doped YBCO on 5° vicinal STO.

increasing BZO concentration, since the matrix surrounding the nanorods shows nearly-parallel, ordered planes in the 4 vol. % sample (a), while the 6 vol. % BZO-doping appears to heavily distort the *a*-*b* planes (b). This lattice distortion and plane buckling is consistent with a high density of dislocations, which would reduce the overall strain in the matrix and may reduce its effect on constraining the size. The increased dislocation density may result from the reduced spacing of approximately 7.8 nm between the nanorods, which is approaching the critical thickness of 5 – 6 nm for dislocation formation [75]. This is more clearly seen in Figure 4.4, which shows Fourier filtered high-resolution TEM images of (a) 4 vol. % and (b) 6 vol. % samples.

By filtering the images, periodic arrangements (like the lattice planes) may be accentuated, making features such as dislocations more visible [86]. From these images, we can more clearly see the reduced order of the YBCO

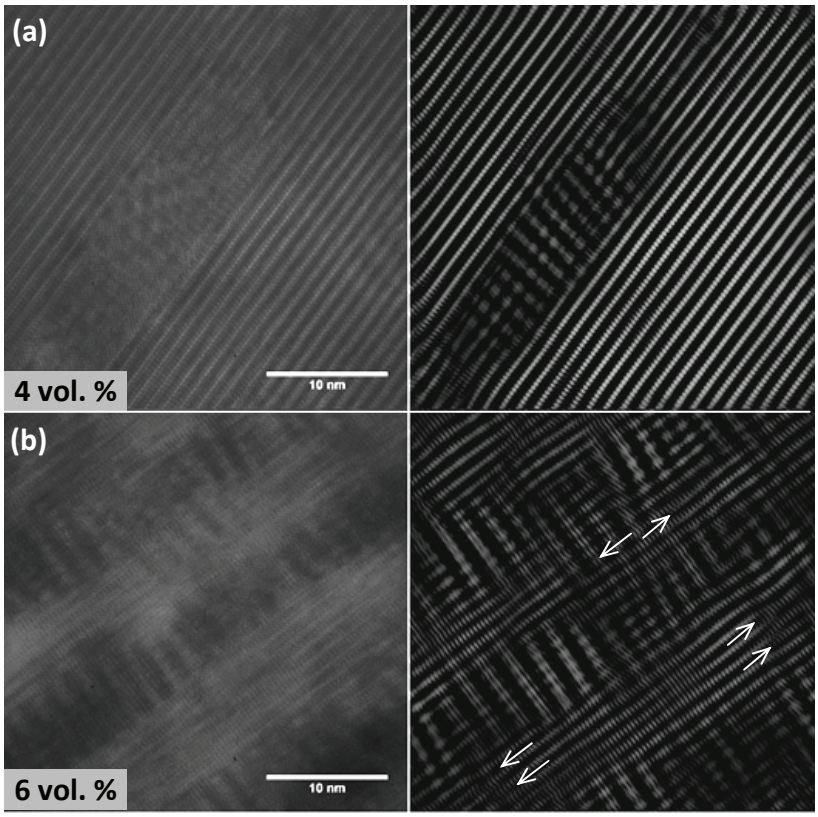

Figure 4.4: **Left**: High-resolution TEM images of (a) 4 vol. %, and (b) 6 vol. % BZO doped YBCO films. **Right**: Fourier filtered images of those on left. Some dislocations are marked with arrows

lattice by observing the distorted planes and multiple dislocations distributed between the nanorods in the 6% sample when compared to the 4%. This may indicate that the reduced spacing between nanorods leads to an overlap of their associated strain fields in the YBCO lattice, thus exceeding the threshold for dislocation formation. Indeed, XRD measurements showed that the YBCO *c*-axis lattice parameter increases slightly from 11.54 Å to 11.64 Å when the BZO concentration is increased from 4% to 6%, as summarized in Table 4-II [54]. Here we see that the *c*-axis contraction with

Table 4-II: YBCO *c*-axis (in Å) with increasing BZO doping and vicinal angle, as measured by X-ray diffraction [54].

	BZO-doping Concentration (vol. %)			
Vicinal Angle	***0 %***	***2 %***	***4 %***	***6 %***
0°	11.74 Å	11.82 Å	11.71 Å	11.67 Å
5°	11.55 Å	11.56 Å	11.54 Å	11.64 Å

increasing vicinal angle counters the tensile strain of the added BZO dopant. The contracted *c*-axis of the nonvicinal 4 – 6 vol. % BZO-doped YBCO was attributed to possible formation of impurity phases [54]. However, the *c*-axis contraction of the vicinal samples is maintained up to 6 vol. % doping, consistent with the distorted planes observed in Figure 4.4 (b). The increase in *c* at 6 vol. % BZO may imply a reduced in-plane tensile strain in the YBCO, also consistent with the abundance of dislocations observed in Figure 4.4 (b).

Figure 4.5 shows the microstructure of 4 – 6 % BZO-doped YBCO films on 20° vicinal STO substrates. The cross-sectional images in Figure 4.5 show similar features to what was observed at the 2% BZO concentration at 20°, where the nanorods are fully aligned in the *a*-*b* planes. As expected from the nonvicinal samples, the nanorod number density is also increased at 4- and 6-vol. %. While the transition to *a*-*b* aligned nanorods is initiated at the lower vicinal angles, they

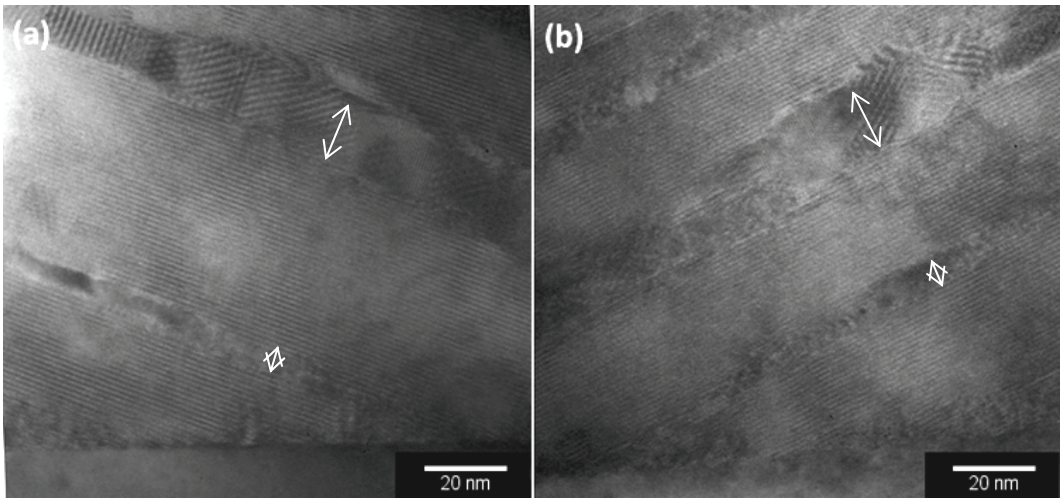

Figure 4.5: Cross-sectional TEM images of: (a) 4 vol. %, and (b) 6 vol. % BZO-doped YBCO films on 20° vicinal STO substrates. The scale bars indicate 20 nm.

continue to follow this trend at 20°. It is noteworthy, however, that nanorods of two size regimes are observed. In both the 4% and 6% BZO-doped samples, nanorods of approximately 6 nm and 11 nm average diameters are visible in Figure 4.5. Thus the larger nanorods are comparable in size to those seen in the 2% samples grown on 20° vicinal STO, while the smaller diameters are comparable to those of the 5° samples shown in Figure 4.3. This bi-modal size distribution may indicate growth effects beyond the misfit strain we have considered so far, and will be discussed further in section 4.2.3. However, it appears that strain overlap continues to be of influence, since as seen in Figure 4.5 (b), the YBCO lattice shows some distortion of the *a*-*b* planes between the BZO nanorods at 6% doping (though not as severe as that observed in Figure 4.3).

So far, we have seen that the nanorod alignment is influenced both by the growth-surface induced strain and by the interaction between nanorods within the

film. To attempt to understand this behavior, we next examine the microstructure of YBCO films with a dopant of lower misfit. With consideration of the added results, we may then continue the discussion of the nanorod alignment.

4.2.2 Lattice Misfit and Nanorod Alignment: $BaSnO_3$-doped YBCO

Since the misfit between the matrix and dopant, at least in part, determines the extent of the lattice strain, we next consider a dopant of lower mismatch that also produces YBCO-compatible self-assembled nanorods. The misfit between the cubic $BaSnO_3$ (BSO) and the lattice parameters of YBCO are listed in Table 3-I, where we see the average *a-b* misfit is approximately 6.4%, compared to 8.1% for BZO. The anisotropic misfit is lower along $[003]_{YBCO}$ (5.4%), so in terms of strain-mediated growth, analogous reasoning used for BZO self-assembly would also apply to BSO. Reports of BSO nanorod growth in YBCO typically show diameters of 5 – 11 nm, where the slightly larger diameter has been attributed to the smaller *a-b* misfit [26, 42, 85]. Although the average in-plane misfit is smaller, the *ratio* of the *c*-axis to *a-b* mismatch with YBCO is slightly larger for BSO than BZO. Because of this, we may expect comparable columnar growth, but perhaps less interaction or overlap in the strain fields of adjacent nanorods as we observed in the higher concentration BZO-doping.

Figure 4.6 shows the microstructure of the 4.5 vol. % BSO-doped YBCO films on (a) nonvicinal, (b) 5°, (c) 10° and (d) 20° STO substrates. The nonvicinal

cross-sectional image shows nanorods with an average diameter of 9.5 nm, consistent with those typically reported [26, 85].

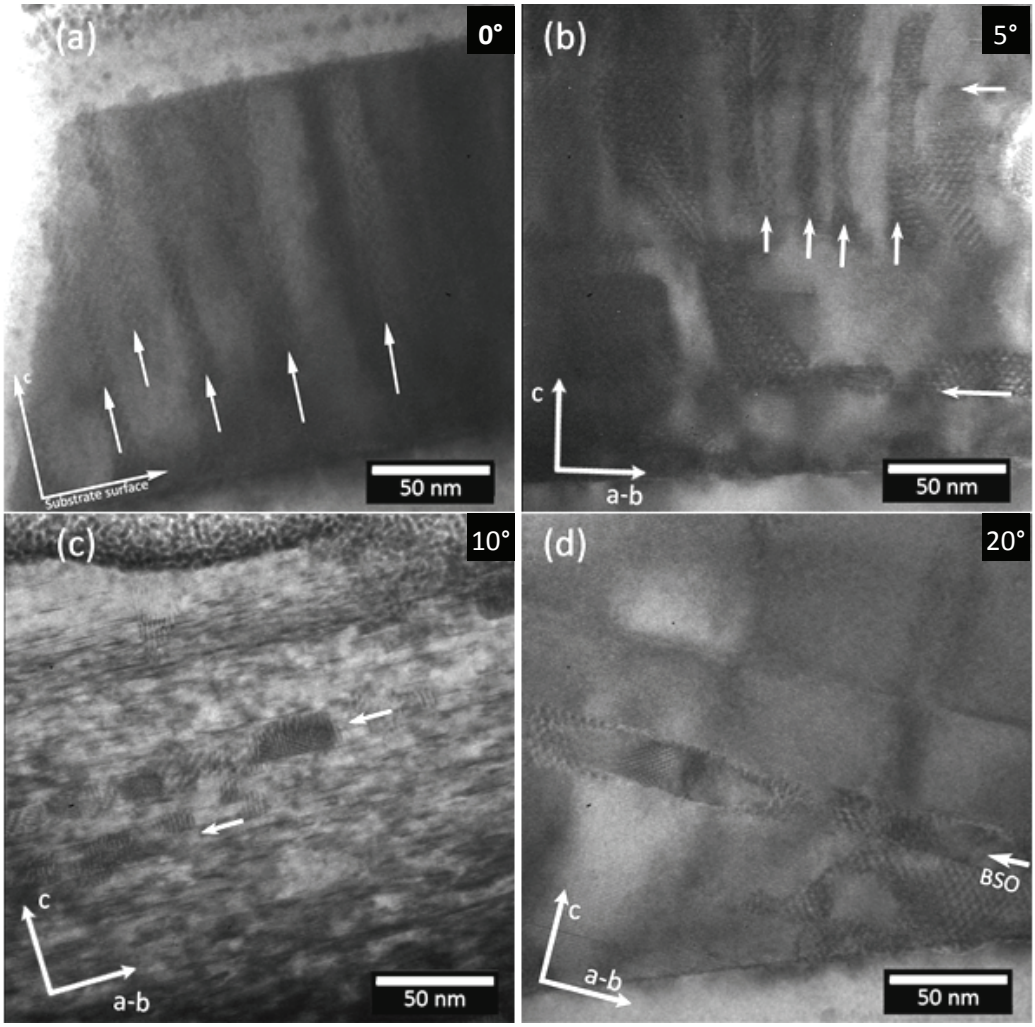

Figure 4.6: Cross-sectional TEM images of YBCO films doped with 4.5 vol. % BSO on (a) nonvicinal, (b) 5°, (c) 10°, and (d) 20° STO substrates.

The 5° vicinal sample in Figure 4.6 (b), however, shows an interesting arrangement of nanorods mostly aligned along the *c*-axis direction with few parallel to *a*-*b* planes. At a similar concentration, the 5° vicinal BZO-doped sample showed a

higher density of *a-b* aligned nanorods, indicating the alignment direction indeed has some dependence on the matrix/nanorod interface. It is also of interest that the mean splay of the *c-axis aligned* (not including those parallel to the *a-b* planes in the average) nanorods increases by approximately 11.8° when compared to the nonvicinal BSO-doped film. However, the increased splay is primarily a result of nanorods at a relatively high-angle (roughly 20 – 30°) from the *c*-axis. Columnar defects at such large angles probably exceed the splay over which vortex pinning is improved. Similar effects were shown in irradiated YBCO, where angular deviation beyond approximately 10° produced diminishing improvement [76].

The 10° sample in Figure 4.6 (c) shows the nanorods realigned in the *a-b* direction, but again showing a heavily distorted YBCO lattice. Also similar to what was observed in the BZO-doped YBCO, the 20° vicinal sample in Figure 4.6 (d) shows BSO nanorods fully aligned along the *a-b* planes of the matrix. The large diameters (22.3 nm on average) of these nanorods are noteworthy, since they are roughly double that of the *c*-axis aligned defects. Similar to the 2 – 4 vol. % BZO-doped films on 20° substrates, the matrix surrounding the nanorods appears reasonably well ordered without a high density of defects. With solely *a-b* aligned defects, we would again not expect a significant change in the vortex pinning behavior for magnetic fields away from this direction.

4.2.3 Vertical and Lateral Correlation of Defects – Qualitative Description

We have observed a realignment of the nanorods parallel to the YBCO *a-b* planes under several conditions. At 2 vol. % BZO doping, the realignment occurs for vicinal angles of 15° – 20°, but this transition angle is reduced to approximately 5° for 4 – 6 vol. % BZO concentrations. Similarly, the lower misfit of BSO produces a range of nanorod alignments at 4.5 vol. % on 5° vicinal STO, while fully *a-b* aligned structures form on 10 – 20° substrates. The doped films on 20° vicinal substrates share a common feature in that the nanorod sizes increase to nearly double what is observed in the lower angle counterparts. Aspects of classical nucleation theory, as well as models developed to describe the self-assembled growth of semiconducting quantum dots, may provide some understanding of these observations.

Recent reports of a new class of nanorod-forming dopants in YBCO, Re_3TaO_7 (where Re stands for rare earth elements such as Er, Gd and Yb), have suggested that the geometry of the nanorods, especially their diameters, may be described by considering the classical treatment of nucleation in phase change [42]. In a change of physical phase, such as the nucleation of a thin film from the gas or liquid phase, the Gibb's free energy (G) of the system changes. By definition, $G = H - TS$ (where $H=U+PV$ is the enthalpy), gives the maximum energy available to do work [87]. This change in free energy has contributions arising from the change in energy (per unit volume) of the two phases, Δg_{AB}, as well as the surface energy of the newly created interface, γ_{AB} [33, 88],

$$\Delta G = (\Delta g_{AB})V + \gamma_{AB}A \qquad (4.1).$$

For example, a spherical precipitate of radius *r* would give,

$$\Delta G = -\Delta g_{AB}\frac{4}{3}\pi r^3 + \gamma_{AB}4\pi r^2.$$

The favorable state would minimize the free energy, whose extrema (at *r**), $\Delta G^* \equiv \Delta G(r^*)$, are found by differentiating,

$$\left(\frac{\partial \Delta G}{\partial r}\right)_{r=r*} = -4\pi\Delta g_{AB}r^{*2} + 8\pi\gamma_{AB}r^* \stackrel{\text{def}}{=} 0$$

$$\Rightarrow r^* = \frac{2\gamma_{AB}}{\Delta g_{AB}} \qquad (4.2).$$

This classic result in phase transformation gives the minimum size at which forming nuclei become stable and growth may proceed [33, 48]. Then for a growing film, this means that the size of the forming nuclei is proportional to the surface energy. For heteroepitaxial growth, like that of BZO or BSO-doped YBCO, this is in turn proportional to the misfit. Therefore, for a fixed Δg_{AB} (which would depend on growth parameters, but not on interfacial properties), we would expect larger nucleation sites with larger misfit between the matrix and dopant. As we showed in Chapter 3, the misfit of BZO to $[003]_{\text{YBCO}}$ increased with vicinal angle up to 10° until the *a-b* realignment initiated. In this case, the critical nucleation diameter may explain the larger diameters seen in the 20° *a-b* aligned nanorods, given the increasing interfacial strain between the matrix and dopant in this direction. However, this does not explain the appearance of the smaller *a-b* aligned nanorods in

the 4- and 6-vol. % BZO doping at the lower 5° vicinal angles. To understand this, we may gain some understanding by drawing on models developed for aligned quantum dots.

Since similar strain-mediated mechanisms are assumed to guide their assembly, we consider the model of Xie, et al. for correlated InAs quantum dots in a GaAs matrix [89]. In this work, they propose an effective probability for correlated growth by considering the migration of InAs through a strained matrix to nucleate at a position directly above the previous island. Again, this assumes favored nucleation at strain minima, as we have discussed in the previous sections and chapter. This is schematically shown in Figure 4.7 from Ref. [89], and shows the critical parameters

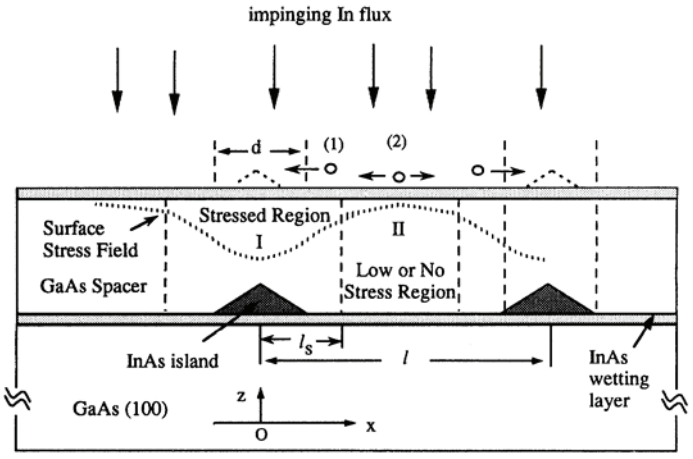

Figure 4.7: From Ref. [89], schematic of model for correlated growth of InAs quantum dots in GaAs matrix.

for correlated growth. In this model, the effective probability for correlation is given by,

$$K = \frac{2D_0}{k_B T} e^{-E_d/k_B T} \frac{\Delta\mu(l_s, z_s)}{l}$$

where $\Delta\mu$ is the change in chemical potential as a function of position along the growth direction z, and l is the spacing between adjacent islands in the lateral direction [89]. The role of mobility and temperature will be discussed in the next chapter, but for this case, we consider these fixed parameters. While corrections for the specific growth mode and composition-dependent variables like the chemical potential would be necessary to make quantitative predictions, some qualitative understanding may be gained from this model. For example, we see that the probability for correlated growth is inversely proportional to the separation between inclusions. Qualitatively, by adapting the correlation probability to the *a-b* aligned nanorods, we may expect the likelihood of realignment to increase with decreased separation.

4.3 Superconducting Properties

The $J_c(\theta)$ dependence for the 4- and 6-vol. % BZO doped samples is shown in Figure 4.8 for 0°, 5° and 20° vicinal angles. As suggested by the microstructure shown in Figure 4.1 – 4.2, peaks for $H \parallel c$ are observed in the $J_c(\theta)$ curves, as expected from the *c*-axis aligned columnar defects in the nonvicinal (0°) samples. Although measured at 1 T, the increased performance would likely continue to higher field intensities given the greater number of defects in the 4-6% BZO concentrations. However, it is noteworthy that while the peak locations reflect the geometry of the defect structure, the overall $J_c(\theta)$ values are depressed in the nonvicinal samples at

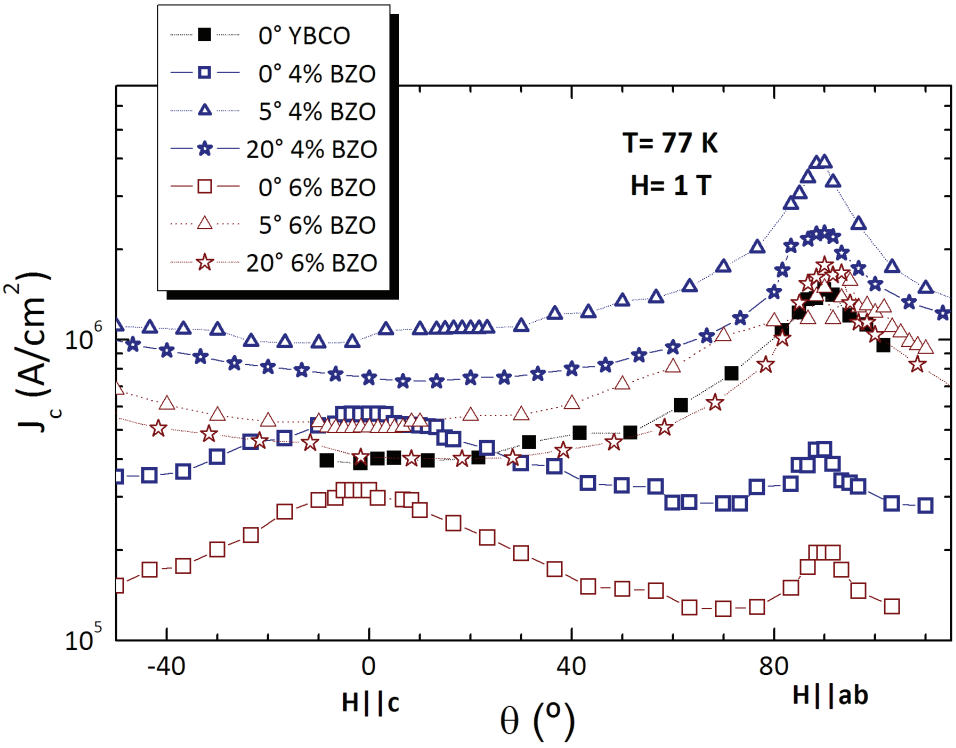

Figure 4.8: Critical current density as a function of magnetic field orientation measured at 1 T and 77 K. The 4 vol. % samples are shown in blue curves and 6 vol. % by red curves. BZO-doped YBCO on vicinal STO. Non-doped YBCO on 0° STO is shown for comparison (filled squares) [53]. All symbols in the plot represent actual data points, while the connecting lines serve only as viewing guides.

both 4- and 6-vol. %. This is probably because of the reduced T_c in the 4- and 6-vol. % BZO concentrations, which are approximately 86 K and 85 K, respectively. Interestingly, the effect of depressed T_c with increased doping is less exaggerated in the vicinal samples, as will be discussed later [54].

The angular dependence of the 5° samples also reflects the observed microstructure. At this vicinal angle, we see an overall increase in $J_c(\theta)$ for the 4% BZO, which shows a broad peak for H || a-b, and only a small increase at H || c.

This behavior is consistent with the mixed nanorod alignment shown in Figure 4.2, where the more continuous nanorods parallel to the *a*-*b* planes provide more pinning force per unit length than the segmented defects in the *c*-axis direction. Similarly, $J_c(\theta)$ for the 6 vol. % BZO sample on the 5° vicinal substrate shows the expected peak for H || *a*-*b*, but here the lack of *c*-axis aligned nanorods is clearly reflected by the nearly flat angular dependence.

The $J_c(\theta)$ curves in Figure 4.8 also reflect the fully realigned nanorods along the a-b planes in the 20° vicinal sample with 4 vol. % BZO, where the pinning at H || *c* is reduced. While a significant peak at H || a-b is shown for both the 4- and 6-vol. % samples, the lower J_c of the 6% sample at 1 T may reflect the slight distortion in the current-carrying a-b planes of the YBCO matrix, as shown in Figure 4.5.

Although the microstructure of the BSO-doped films showed somewhat similar behavior to the BZO, the $J_c(\theta)$ dependence of the BSO samples shown in Figure 4.9 highlights some distinctions. As shown in Figure 4.6, the nonvicinal (0°) sample shows nanorods highly aligned along the *c*-axis, and this is reflected by the distinct peak in the angular dependence of J_c at 1 T and 77 K shown in Figure 4.9. This strong increase for H || *c* in the 0° sample is consistent with results typically reported in the literature for BSO-doped YBCO, and is generally attributed to the continuity of the long nanorods providing high pinning force per unit length, as well as by local T_c reduction due to Sn substitution in the surrounding YBCO matrix [26, 40, 75, 85]. Interestingly, the 5° vicinal sample does not show any increase at H || *c*,

and the peak for H || a-b is only comparable in magnitude to the intrinsic pinning peak of the undoped YBCO sample on nonvicinal STO. The lack of added pinning in the H || c direction may be due to the very large deviation in the direction of alignment, as pointed out in the discussion of Figure 4.6. In this case, the shorter nanorod segments along the c-axis provide a smaller net pinning force, while it is

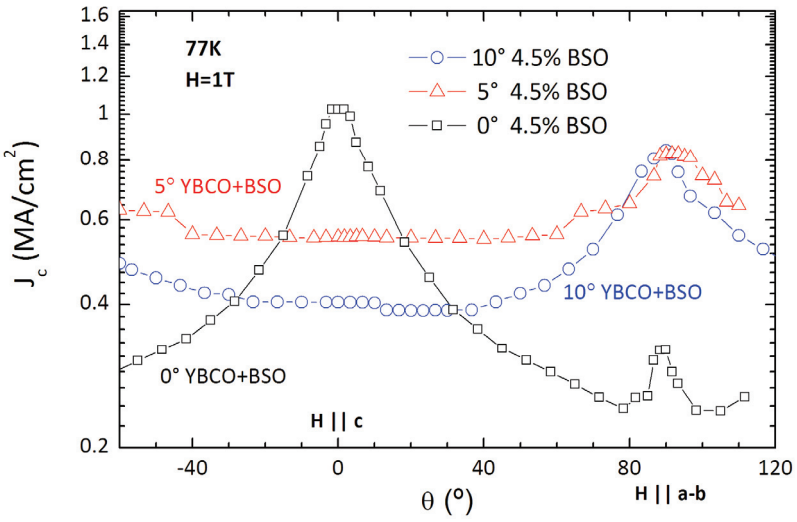

Figure 4.9: Critical current density with magnetic field orientation for YBCO films doped with 4.5 vol. % BSO on STO substrates with vicinal angles of 0°, 5°, and 10° [53]. All symbols in the plot represent actual data points, while the connecting lines serve only as viewing guides

likely that those at higher-angles exceed the range of effective splay. This is consistent with the results of Krusin-Elbaum, et al., where they showed that the benefit of reduced vortex hopping with splayed columnar defects diminishes for splay greater than approximately 10° [76]. Thus, at this magnetic field intensity, any gains of the inclusions may be minimized by their very large angular deviation. The $J_c(\theta)$

of the 10° BSO-doped sample shows similar behavior for H || a-b. This is consistent with the structure observed in the cross-sectional images, where the BSO nanorods were aligned along the a-b planes by this vicinal angle. Away from H || a-b, however, the $J_c(\theta)$ is largely suppressed, which probably reflects the highly defective YBCO lattice as shown in Figure 4.6.

Figure 4.10(a) shows the transition temperatures as a function of the vicinal angle for 2 – 6 vol. % BZO and the 4.5 vol. % BSO concentrations. Doping YBCO with BZO is generally reported to reduce the T_c by approximately 0.5 K – 1.5 K per vol. % increase [32, 41, 90]. This effect is less pronounced in BSO-doped films, however, which decrease more slowly with dopant concentration, where up to approximately 9.5 vol. %, a T_c of about 88 K has been reported [91]. As shown in Figure 4.10(a), we measured a similar decrease in the nonvicinal (0°) samples, which decreased from approximately 90 K with no doping, to ~84.5 K at the 6 % BZO concentration, and ~87.5 K with 4.5 vol. % BSO doping. The 2 – 4 vol. % BZO-doped films showed comparable T_cs of ~86 K, making the 2 vol. % T_c slightly lower than typical, but well the within experimental spread of 1 – 2 K commonly observed in PLD-grown YBCO films. The vicinal samples appear to mitigate this decrease to some extent, since as shown in Figure 4.10, the extent of the T_c reduction is reduced. Since the spacing between Cu-O planes in the YBCO is known to vary the transition temperature, the structural effects of the BZO on the matrix may be expected to also influence the T_c [3, 41]. In Figure 4.10(b), a general trend of reduced YBCO c-axis

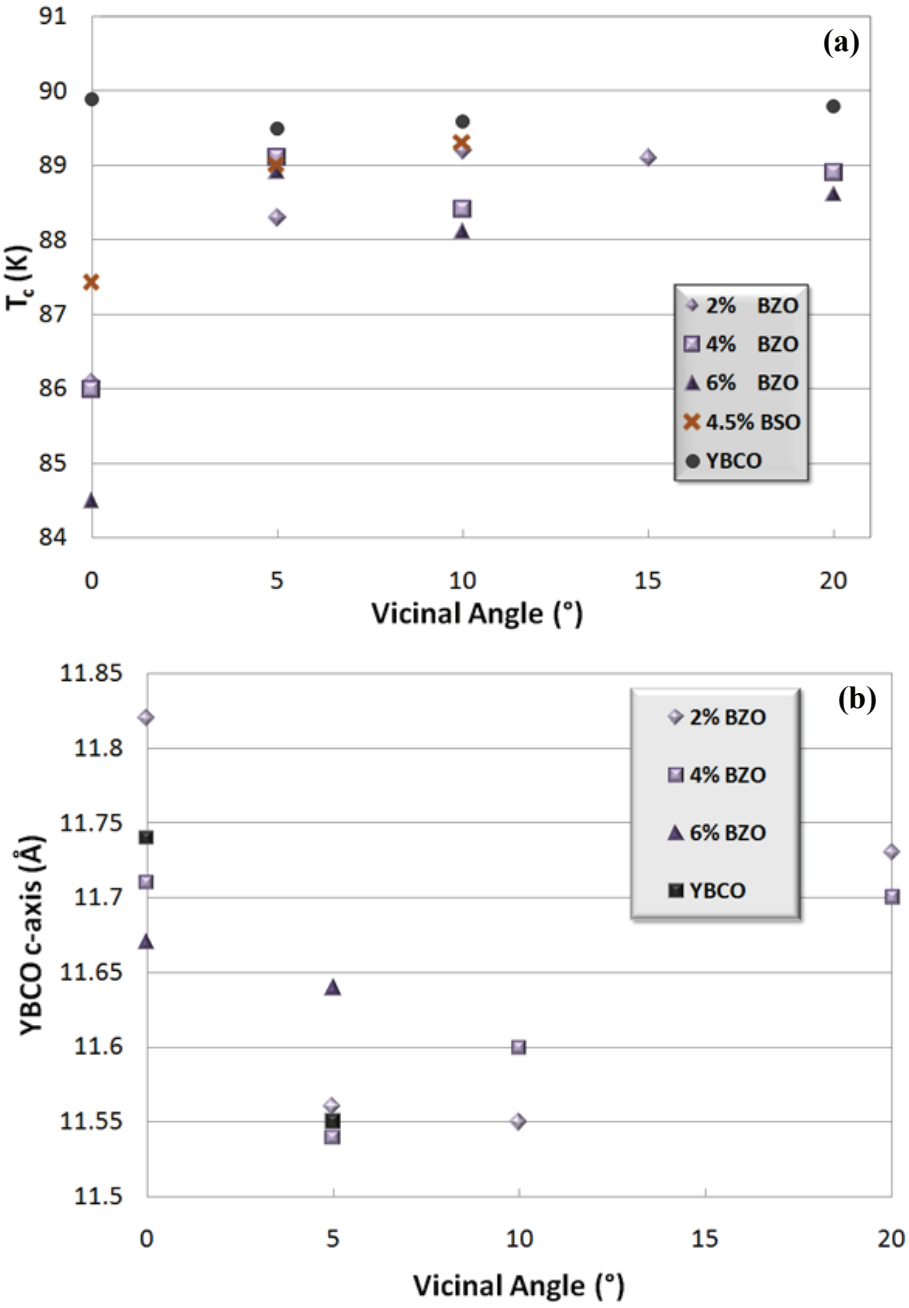

Figure 4.10: (a) Transition temperature, and (b) YBCO c-axis length as function of vicinal angle for 2 – 6 vol. % BZO and 4.5 vol. % BSO concentrations. Values for undoped YBCO are also shown for comparison [54].

is observed with increasing vicinal angle up to ~10° for the various BZO concentrations, which relates to the generally levelling T_c in the doped vicinal samples. However, the *c*-axis parameter does increase again in the 20° vicinal samples, corresponding to the *a*-*b* realignment in the 2 – 4% BZO samples, but without a decrease in T_c in this case. Thus, while the structural changes may have some influence in the transition temperature leveling, other factors may be contributing to the effects on T_c.

4.4 Conclusions

While increasing the YBCO dopant concentration provides a means to increase the defect density for increased pinning at higher magnetic field intensities, it also introduces microstructural interactions between the inclusions. In nonvicinal films, the result is simply more nanorods with a shorter spacing. However, since the nanorod assembly and alignment is a strain-mediated process, by reducing the spacing between adjacent nanorods, especially in the modulated vicinal films, the effects of overlapping strain fields become apparent. For example, we have seen that the realignment of the nanorods to the *a*-*b* direction begins at much lower vicinal angles of 5 – 10° when the BZO concentration is increased to 4 vol. %, and is fully realigned at 5° by 6 vol. %.

The overlapping strain effects also become apparent through the distorted YBCO matrix at the lower vicinal angles and 6% BZO doping, which

correspondingly reduces the transport properties in these samples. On the other hand, the strain interaction at 4 vol. % is adequate to induce the *a*-*b* realignment at lower vicinal angles, while maintaining its superconducting properties, including a mediated T_c reduction with increased doping.

We have also shown that the interfacial relationship between the dopant and matrix plays a role in the nanorod alignment. For example, for similar doping concentrations, the lower mismatch of BSO induces nanorod realignment at higher vicinal angles when compared to BZO doping. The large angular distribution produced at low vicinal angles then exceeds the range over which added splay is beneficial to vortex pinning, as reflected by the depressed $J_c(\theta)$ performance.

While simple thermodynamic and more extensive growth models applied to self-assembled quantum dots provide some basic qualitative agreement with these results, extending predictive models would require much more detailed analysis. However, the self-assembly process is likely very dependent on dynamic effects that are explicitly accounted for by these models. Therefore, we will next consider the effects of growth temperature and dynamics on the self-assembly process for doped YBCO thin films.

Chapter 5

Growth Temperature and Microstructural Effects

The temperature at which the substrate is held during the growth of YBCO thin films plays an important role in the overall quality of the sample. Phase stability and microstructure are among the properties influenced, consequently affecting the superconducting properties, including the critical current and transition temperature [92 – 93]. Additionally, and perhaps more dramatically, the dynamics of the growth process are strongly dependent on temperature. If the supplied thermal energy is large enough, the depositing species may become sufficiently excited to overcome potential barriers, allowing for increased surface diffusion and longer diffusion lengths, thus influencing nucleation location [94]. Since the change in growth dynamics affects the microstructure of the YBCO lattice, the defect landscape may also change, influencing the overall vortex pinning structure of the film.

The changes in vortex pinning effects with growth temperature (T_g) of undoped YBCO samples have been studied by Wang, et al, and an increasing trend in $J_c(H)$ with growth temperature was reported for magnetic fields up to ~4.9 T [95]. Correspondingly, the density of microstructural stacking faults increased with T_g and it was suggested that the associated dislocation cores provided the additional pinning centers responsible for the higher $J_c(H)$ [95]. Thus, as we expect a variation of growth temperature to influence the microstructure of the growing film, we may also expect a corresponding change in the formation of secondary inclusions such as BZO

nanorods, and ultimately the $J_c(H)$ dependence. Indeed, this kind of behavior was recently observed by Maiorov, et al., where they showed that up to H ~ 3 T, $J_c(H||c)$ increases with growth temperature for 745° C < T_g < 800° C, but begins to decrease beyond that range [96]. Corresponding to the $J_c(H)$ increase, they observed that with increasing T_g, longer, more parallel BZO nanorods form. From this T_g dependence, together with data showing that reducing the laser pulse repetition rate (deposition rate) produces a comparable increase in $J_c(H||c)$, the authors demonstrate that growth dynamics play a vital role in the overall vortex pinning and $J_c(H)$ behavior.

The change in pinning structure shown by Maiorov, et al. gives insight into the interesting dynamic effects involved in the self-assembly and alignment of the nanorods in YBCO films. Together with the equilibrium observations of the last two chapters, we may assemble a clearer understanding of the mechanisms responsible. However, it is notable that, in the experimental conditions of their work, an ablation target containing both 5 mol. % Y_2O_3 (~ 2.3 vol. %) and 5 mol. % BZO (~ 2.6 vol. %) was used. This may be a significant experimental variation since, as we saw previously, the strain relationship between inclusions in the YBCO matrix also plays an important role in the nanorod alignment. In addition, inclusions of Y_2O_3 are commonly observed in pure as well as doped YBCO thin films (some examples of dopants showing these inclusions include BZO, Y_2BaCuO_5, and Y_2O_3), and increasing the concentration of Y_2O_3 would increase the number density of these particles [22, 24, 51]. These kinds of particles and discontinuous Y_2O_3 layers aligned along the *a-b* plane were indeed observed by Maiorov, et al., and thus we expect the

alignment, growth and continuity of the BZO nanorods may be affected by their addition.

Therefore, in this Chapter, we investigate the microstructure of 2 vol. % BZO-doped YBCO films with varied growth temperature, and together with the data shown by Maiorov, et al., examine the dynamic mechanisms guiding the nanorod growth and alignment. By considering the microstructural and vortex pinning dependence on T_g, we then examine the application of the growth and alignment models discussed in previous chapters to the behavior observed in this system.

5.1 Basic Growth Dynamics of Thin Films

As introduced in Chapter 2, the growth of thin films by PLD varies with several parameters. In particular, the mobility of deposited adatoms, which gives a measure of the tendency for species migration at the growth surface and within the film, is strongly dependent on growth temperature. While variations in the surface energy (like those discussed in previous chapters for vicinal surfaces) influence nucleation and growth, the available thermal energy determines the diffusivity, and thus the characteristic length for atoms traversing the growth surface [68, 94]. Therefore, since the formation of nanorods requires an ordering of the supplied second-phase material through the YBCO matrix, the growth temperature should also play a significant role in this process. To understand this growth mechanism, we first consider some of the basic thermodynamic quantities involved, followed by some aspects of models describing the dynamics of thin film growth.

While in thermodynamic equilibrium, film growth proceeds by one of (or a combination of) three growth modes, as discussed in Chapter 3. Although the growth mode is strongly influenced by the thermodynamic surface energies of the system, kinetic effects are also significant when the supplied energy is large enough. Given enough energy, motion across the growth surface as well as through the bulk of the thin film is possible and follows a classical thermodynamic description. In general, a flux of diffusing species, *J*, is expected under a given driving force such as a gradient in concentration or chemical potential, and is described by the relationship given by *Fick's Law* [87, 97],

$$\vec{J} = -D\vec{\nabla}N \qquad (5.1).$$

Here *N* is the concentration of diffusing atoms, and *D* the *diffusion coefficient* (or *diffusivity*). For the case of a growing crystal, the diffusivity introduces an exponential temperature dependence,

$$D = D_0 e^{-E_d/k_B T} \qquad (5.2)$$

where E_d is an activation energy determining the barrier height that restricts atomic motion at the growth surface. The coefficient D_o depends on sample geometry and rate of arrival, but is independent of temperature [33]. Thus, the diffusivity quickly increases with increasing temperature but gradually levels to a nearly constant value, as qualitatively shown in Figure 5.1. From this perspective, the increasing diffusivity

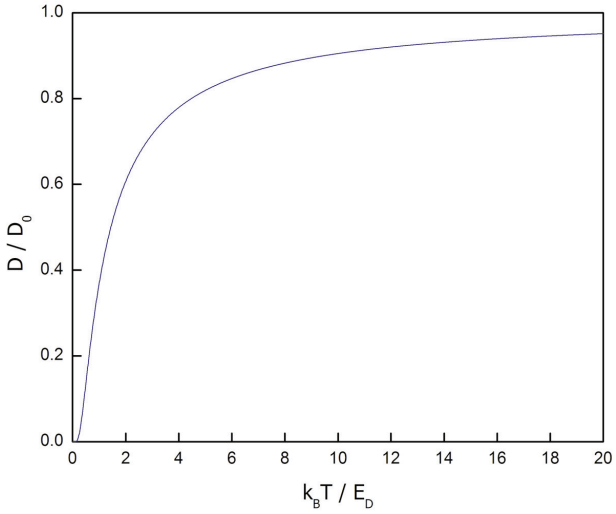

Figure 5.1: Calculated diffusivity as a function of temperature. The horizontal axis is plotted in units of (k_B/E_D) while the vertical is scaled by D_o.

with temperature would allow for an increased range of BZO migration, thus providing more favorable conditions for continuous columnar growth as opposed to discrete particles or truncated rods.

To examine the BZO nanorod dependence on mobility, we have varied the growth temperature and examined the resulting microstructure and vortex pinning behavior. From the contribution of the diffusivity in allowing the BZO to migrate and add to the average nanorod length, we would expect the most rapid increase with temperature until approximately $T_g = E_D/k_B$, where the rate would begin to slow. However, the diffusivity does not solely determine the probability of correlated BZO growth (as we saw in Chapters 3 – 4), and we might expect the strain distribution, growth rate and BZO concentration to also contribute.

The growth dynamics thus give another means to design the defect structure to produce the needed geometry, and growing continuous, longer length nanorods along the *c*-axis would strongly enhance $J_c(H \,||\, c)$. However, as we saw in the 2 vol. % BZO-doped films at low vicinal angle, a degree of splay is necessary to prevent vortex hopping. This again indicates that growth conditions leave considerable flexibility for optimization.

5.2 Experimental Details

Thin films of epitaxially grown YBCO were deposited on single crystal $SrTiO_3$ and $LaAlO_3$ substrates by PLD, as described in Chapter 2. Although $LaAlO_3$ has a slightly smaller mismatch to YBCO, overall the vortex pinning behavior was comparable to films grown on $SrTiO_3$. Therefore, the abundance of twin boundaries native to the $LaAlO_3$, may produce the most significant microstructural difference between them. Because of the minute difference in pinning behavior, only films grown on the $SrTiO_3$ substrates were characterized by TEM, and the superconducting properties shown here are for these samples only.

To examine the role of mobility in BZO nanorod formation, the substrate temperature was varied while the other growth conditions were held constant. The fixed parameters of 300 mTorr O_2 partial pressure, 3.2 J/cm^2 laser energy density, and an 8 Hz pulse rate were used for each deposition. A deposition rate of 33 – 38 nm/min for 10.25 min produced films 340 – 390 nm thick. The ablation target, with 2% BZO by volume, was mixed, pressed and sintered as described in Chapter 2. The

varied growth temperature ranged from 780° C to 835° C. The resulting vortex pinning behavior as indicated by the $J_c(H)$ dependence as well as T_c were determined magnetically using a vibrating sample magnetometer. The resulting microstructures were characterized by cross-sectional TEM and XRD. TEM cross-sections were prepared by FIB (as described in Chapter 2), producing ~15 μm long (along <*100*> or <*010*>) and 150 – 250 nm thick foils. Final thinning was carried out using 1-2 keV Ar ions incident at 10 – 15° from the <*001*> directions. Amorphized or damaged material was commonly observed as a result of the high energy Ga and Ar milling, and the foils were polished using 600 – 900 eV Ar ions at 10 – 12° from <*001*> to remove the damage area.

5.3 Microstructural Results

Cross-sectional TEM images of the YBCO + 2 vol. % BZO films were recorded and show the evolution of the microstructure with increasing growth temperature. Figure 5.2 illustrates this by showing bright-field images that look down the <*100*> or <*010*> directions of the YBCO. In this figure, we can see a general trend of increasing BZO nanorod length and continuity with increasing growth temperature. In Figure 5.2, the drawn lines illustrate examples of the paths of the nanorods through the matrix and their overall length. Measurements of segment length and their relative alignment angles with respect to [*001*] were made by

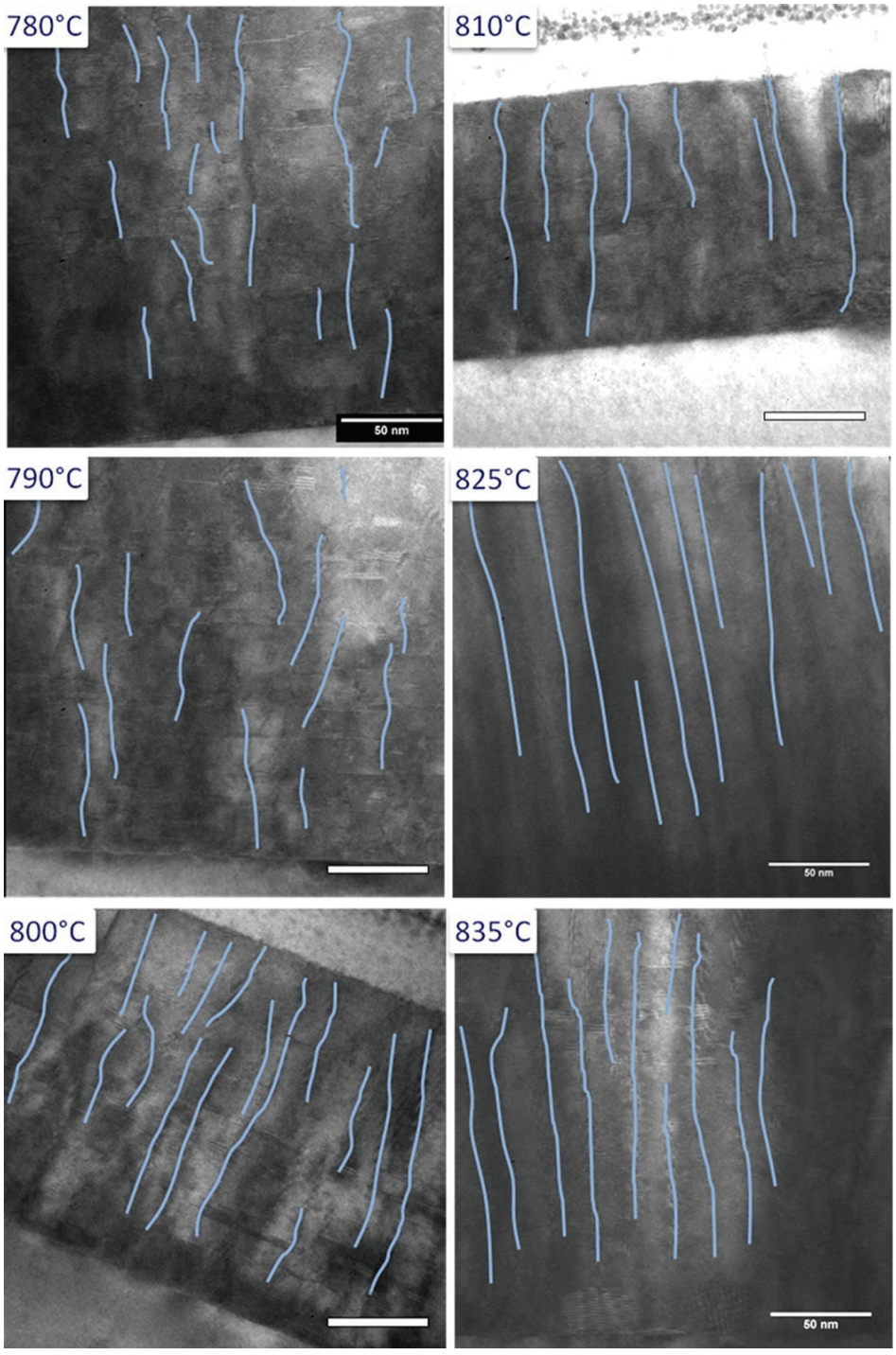

Figure 5.2: Cross-sectional bright field TEM images of YBCO thin films doped with 2 vol. % BZO. Images are shown for growth temperatures of 780° – 835°C, and the overlaid lines illustrate the paths of the BZO nanorods through the film. The scale bars represent 50 nm.

nanorods increases on average from 46.3 nm to 118 nm for increasing T_g from 780° C to 835° C. The average nanorod diameters increased only slightly and ranged from 4.7 – 6.0 nm. Additionally, the overall alignment of the BZO nanorods relative to the YBCO c-axis increases, with the average angle of deviation from $[001]_{YBCO}$ decreasing from 10.6° to 6.3° over the same range of T_g. Thus, longer, more parallel nanorods are observed with increasing growth temperature. This appears to be consistent with previous reports, and illustrates the influence of dynamic effects during growth [96]. The increasing length of the nanorods with T_g is consistent with the increase in mobility with temperature shown in Figure 5.1, and may reflect the added probability for self-assembly by allowing for BZO migration to energetically preferred sites for nucleation (for instance, where strain is minimized).

By comparison, however, Maiorov, et al. showed the average nanorod length increases at a seemingly different rate over a wider temperature scale [96]. This is illustrated in Figure 5.3, where the average nanorod length measured in this study is plotted versus growth temperature along with the values reported in Ref. [96]. In this figure it is apparent that over a smaller temperature range (780° C – 835° C), our measured rate of increase of average length is faster than in that reported in Ref. [96]. It is possible that this indicates a discrepancy in temperature calibration and scaling between the two experimental setups, but it may also show a physical distinction in the mechanisms governing the nanorod formation. To understand the discrepancy, we will further expand on the range of values measured when the superconducting

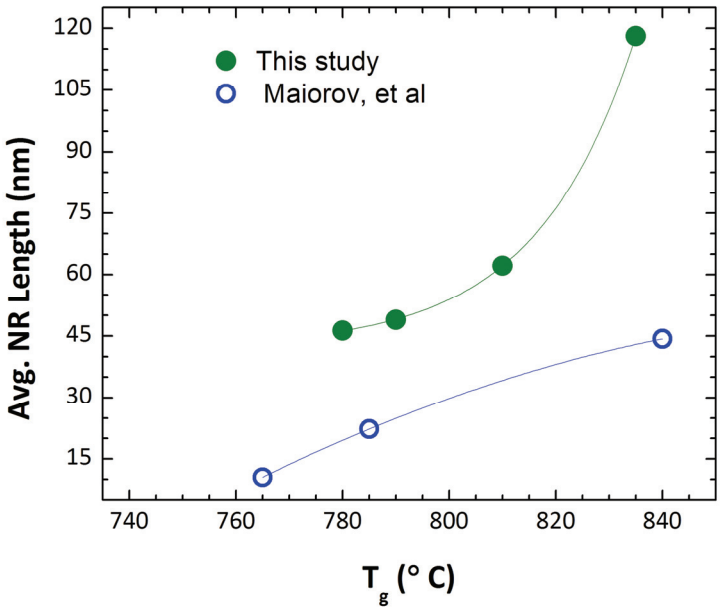

Figure 5.3: Average BZO nanorod length in YBCO matrix as compared to values reported in Ref. [96]. The solid lines represent a polynomial fit to the data points shown by symbols.

properties are discussed. However, this may give a preliminary indication of an impeding effect of the Y_2O_3 on the BZO nanorod formation. Several mechanisms may lead to the disruption of the nanorod growth, such as the modified strain distribution, chemical potential, and diffusivity. It is worth noting that the misfit of the cubic Y_2O_3 is 'negative', meaning that a compressive strain is induced on the YBCO lattice, compared to the tensile strain due to the BZO. Thus, the presence of Y_2O_3 could locally reduce the net strain on the YBCO lattice due to the BZO. Some of the effects of these changes, and the implied distinctions from the results shown in Ref. [96] will be discussed further in the following sections as we consider the extension of dynamic models to this system.

5.4 Superconducting Properties with T_g

The change in vortex pinning with increasing growth temperature is significant, as evident in Figure 5.4 where the critical current density vs. applied magnetic field is shown for $H \parallel c$, measured at 77 K. Overall, an increasing trend in $J_c(H)$ is observed with increasing T_g. The largest increases occur as the growth

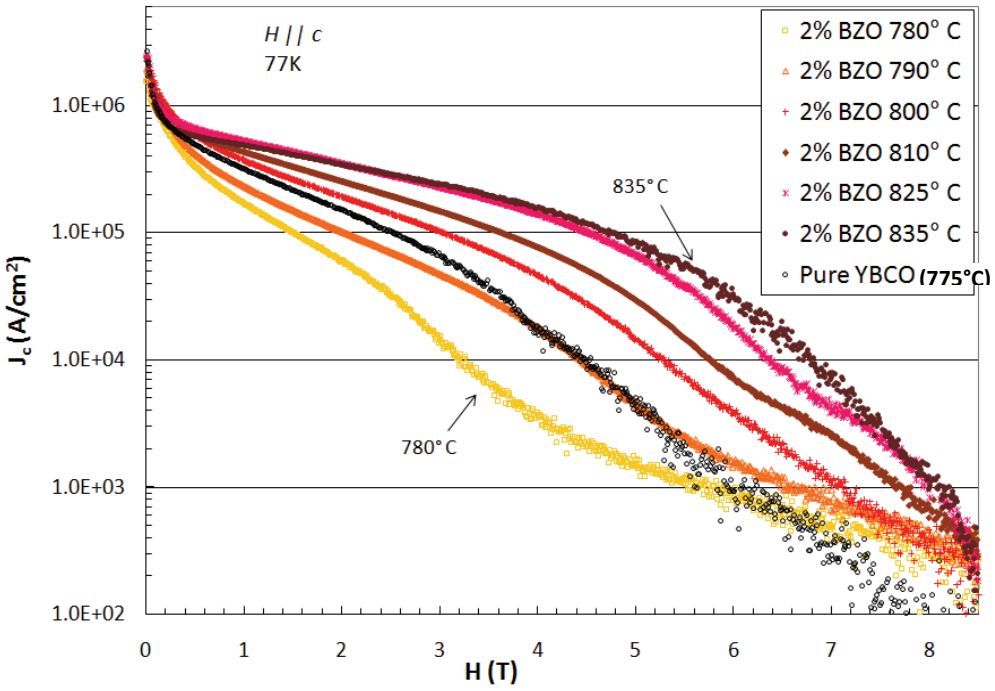

Figure 5.4: J_c vs. applied magnetic field for YBCO films with 2 vol. % BZO with varied growth temperature. Data for an undoped ("pure YBCO") sample is included as a reference. An increasing trend with T_g is clear for H > 0.5 T, indicating a change in the vortex pinning structure. Each plotted point represents a measured value.

temperature is raised from the lowest value of 780° C, but $J_c(H)$ continues to consistently increase until $T_g \sim 825°$ C. This behavior, especially when compared to the $J_c(H)$ of the pure YBCO film, appears to agree with the microstructural observations of more continuous BZO nanorods in the film. It is interesting,

however, that although the nanorods continue the trend of increasing average length up to 835° C, the rate of increase of $J_c(H)$ appears to slow at this temperature range. This may be caused by the reduced splay of ~ 6° at this temperature, which is consistent with the comparable values of splay measured in the nonvicinal BZO-doped sample shown in Figure 3.1. However, the modified pinning structures produced by the longer nanorods at the intermediate temperatures appear to provide a higher force per unit length on the vortices, thus increasing the maximum net F_p and, consequently, J_c. This is seen in Figure 5.5, which shows a plot of the flux pinning force $F_p(H)$ as defined in Chapter 1. The added length and continuity of the nanorods probably comes at the expense of smaller nanoparticles that, with the added mobility, are able to overcome the activation barrier and nucleate at a position where they instead contribute to the columnar structure.

Another interesting feature of Figure 5.5 is that both the magnitude of the maximum F_p, as well as the value H_{max} at which this occurs, increase with increasing T_g. This trend is clearly seen in Figure 5.6, where the value of H corresponding to the maximum pinning force density is plotted against the growth temperature.

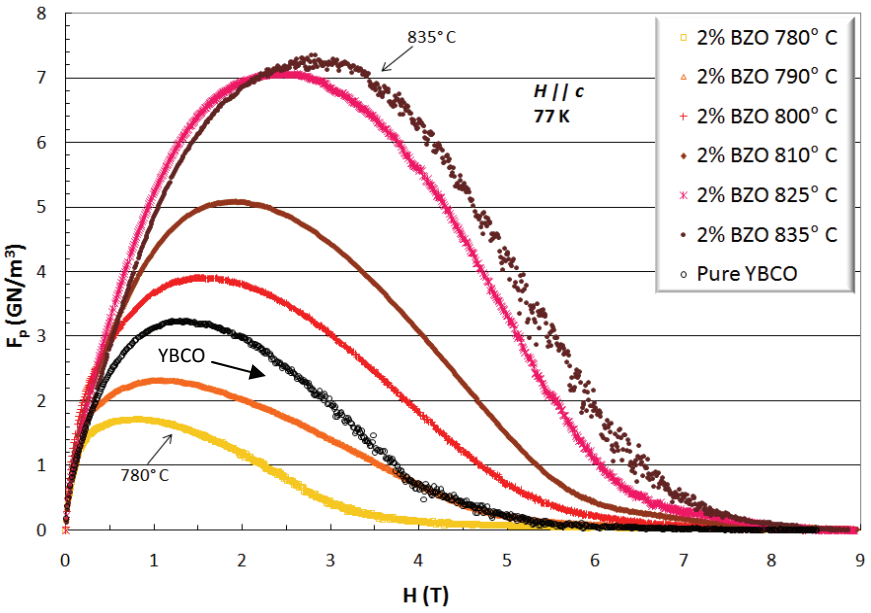

Figure 5.5: Flux pinning force (per unit volume) vs. applied magnetic field for T_g from 780° C to 835° C. The increasing value of $F_{p\,max}$ and H_{max} indicate the increased correlation of the BZO nanorods with T_g Each plotted point represents a measured value.

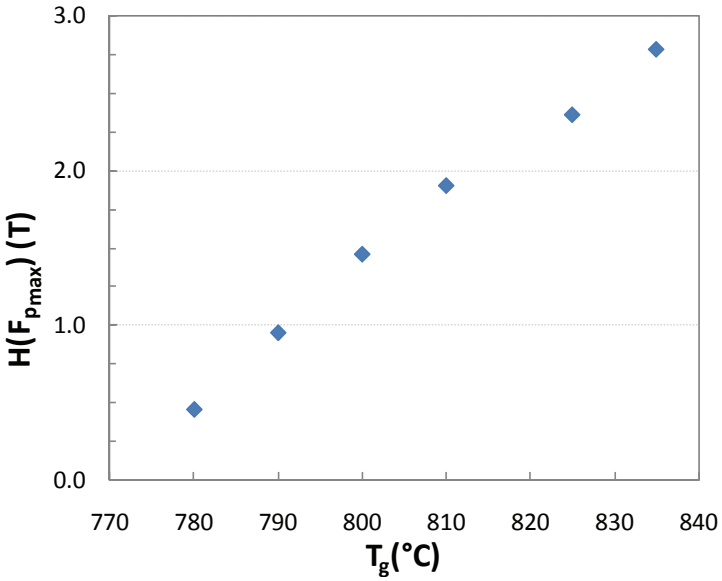

Figure 5.6: Values of the applied magnetic field at which the maximum flux pinning force density occurs.

Since accommodating higher magnetic field intensities generally requires increasing the number of available vortex pinning sites, the nearly linear increase in H_{max} implies that the matching field of the defect density is increasing with T_g. This is not necessarily expected since the concentration of BZO (and thus the expected defect density) is unchanged in this experiment. However, from the cross-sectional TEM images, the average nanorod spacing is observed to indeed decrease with increasing T_g. These measured average distances are shown in Figure 5.7, where we see the separation decreases from approximately 24 nm to 11 nm over the 55° C temperature

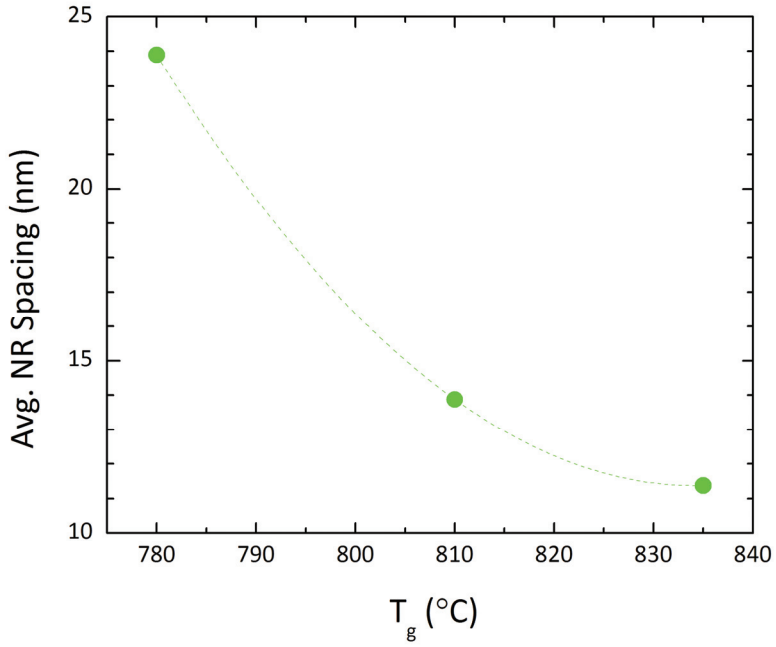

Figure 5.7: Average separation between BZO nanorods as a function of growth temperature. The averages are based on multiple measurements of several cross-sectional TEM images at each temperature. The dashed line represents a polynomial fit to the data points shown by symbols.

range. Assuming a triangular lattice distribution of nanorods, this results in an increased defect density from ~5.1 x 10^{10} cm^{-2} to ~2.2 x 10^{11} cm^{-2}, which would account for part of the approximately factor of six increase in matching field. These results suggest inconsistency however, since increasing both the number of nanorods and their length would imply an increase in the total BZO volume. Similar accounting discrepancies have been observed in vicinal BZO doped YBCO films, and x-ray diffraction studies suggested that additional $Ba_2Zr_{2-x}Y_xO_6$ phases may be present [24]. The higher growth temperature may reduce the formation of these additional phases, contributing to the Zr availability for the additional $BaZrO_3$ observed.

An increase in vortex pinning with T_g was also reported by Maiorov, et al. However, in their work a distinct turning point is observed, after which increased T_g results in lower $J_c(H)$ [96]. This is illustrated in Figure 5.8 where J_c values are plotted for self-field, 1 T and 3 T at 77 K. From this figure, maxima are evident in the trendlines for the data reported in Ref. [96], while such turning points are not as clear in our experimental data. From the positions of the turning points, a general leftward shift (lower T_g) is apparent as compared to the data of Ref. [96].

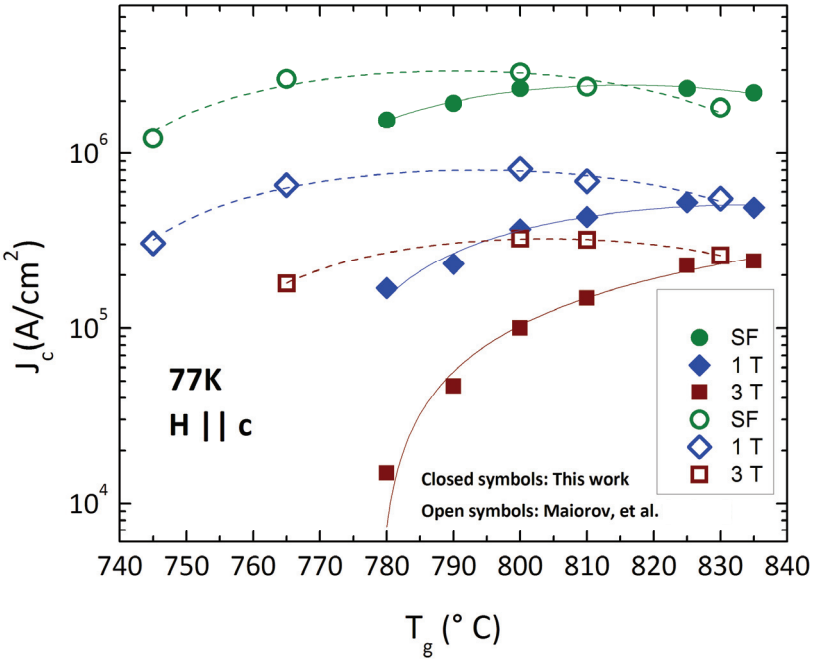

Figure 5.8: Critical current densities at self-field, 1 T and 3 T as a function of growth temperature. The closed symbols are the data points collected in this work, and for comparison, the open symbols show the values reported in Ref. [96]. The solid and dashed lines represent a polynomial fit to the data points shown by symbols.

To gauge the effects of calibration and scaling differences between the experimental setups as opposed to physical distinctions, Figure 5.9 shows J_c as a function of average nanorod length for the two data sets. If the vortex pinning mechanisms are the same, we expect that the maximum critical current density should occur for comparable defect structures. Therefore, the dependence of J_c on length should be consistent if the same pinning mechanisms are responsible, though a shift may be possible due to systematic error in measurement. However, Figure 5.9 shows that the change in peak position (maximum J_c for a given applied magnetic field) is

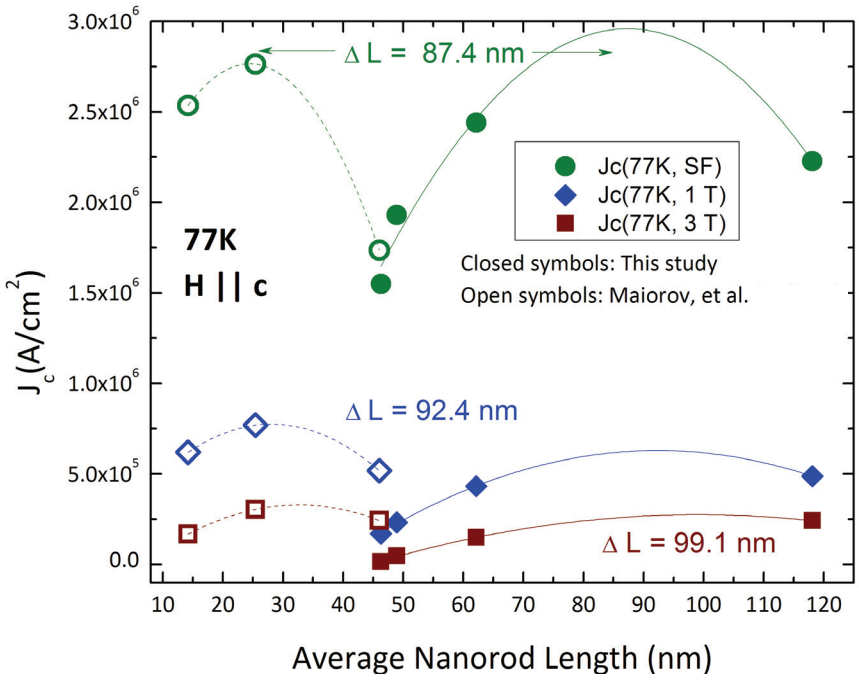

Figure 5.9: Critical current density at self-field, 1 T and 3 T as a function of average nanorod length. Values are shown both for the work of this study and those from Ref. [96]. The difference in peak positions of the fitted curves is indicated. The solid and dashed lines represent a polynomial fit to the data points shown by symbols.

increasing with increased intensity of *H*. Thus, it appears less likely that systematic error, such as temperature calibration, is responsible for the difference in pinning behavior, and more likely that it is a different mechanism.

Since the J_c dependence is less likely to result from systematic discrepancy, the observed change in pinning mechanism also appears to indicate the significant role of the Y_2O_3 particles. Since the particles also act as pinning centers, it is reasonable to expect an altered $J_c(H)$ behavior. This illustrates an added degree of control over the defect landscape through the addition of randomly distributed point-

like defects. It also shows that the growth dynamics are significantly altered by the coupled effects of the BZO and Y_2O_3 inclusions.

5.5 Microstructural Mechanisms of Aligned Growth

In Chapter 4, we discussed the application of the growth model for vertically correlated quantum dots to the YBCO/BZO system. In this model, Xie, et al. develop an expression for the effective probability of In adatom migration to the strain-relaxed region immediately "above" the preceding island [89]. Given the dynamic nature of this strain-mediated correlation model, the growth temperature is a key parameter. That is, the ability for adatom migration to the energetically preferable nucleation site is an essential condition for correlation, and diffusion processes are directly linked. Therefore, using the microstructural data collected we may investigate the application of this correlated growth model by varying another significant parameter, the growth temperature.

The effective probability for migration shown by Xie, et al. is given by the expression [89],

$$K = \frac{2D_0}{k_B T} e^{-E_d/k_B T} \frac{\Delta\mu}{l} \qquad (5.3).$$

Where, as previously defined, Δμ is the change in chemical potential as a function of position along the growth direction (z), and in the lateral direction, l is the spacing between islands. This expression is plotted qualitatively to show its dependence on temperature in Figure 5.10. This plot shows that for all other parameters held constant, increasing temperature produces a sharp maximum in the effective

probability at $T = E_D/k_B$. This result shows what may be intuitively expected since the increasing thermal energy eventually meets the activation energy barrier, and migration and the correlation probability are maximized. According to this description, the likelihood of correlated growth increases quickly toward the activation energy temperature. However exceeding this temperature by a factor of two reduces the probability by approximately 17%, while an excess of five times would result in nearly half the probability. As we saw in Figure 5.3, the average length of the nanorods continued to increase with T_g, showing qualitative agreement with the predicted probability increase. Since a 7% increase in temperature (from 780° C to 835° C) yields approximately a factor of 1.5 increase in average nanorod length, it is likely that this range lies in a region approaching the barrier potential.

As previously discussed, the model by Xie, et al. approaches the correlated growth mechanism by primarily considering strain-induced diffusion effects. This explicit consideration of the growth dynamics is convenient for the YBCO/BZO system since the nanorods appear to be more like continuous structures than particles separated by layers of matrix material. However, models like one shown by Tersoff, et al. predict similar results by specifically considering nucleation at strain minima [98]. In this case, the dynamic effects are assumed implicitly through the nucleation treatment shown elsewhere, but intentionally excluded from the correlated growth model [99].

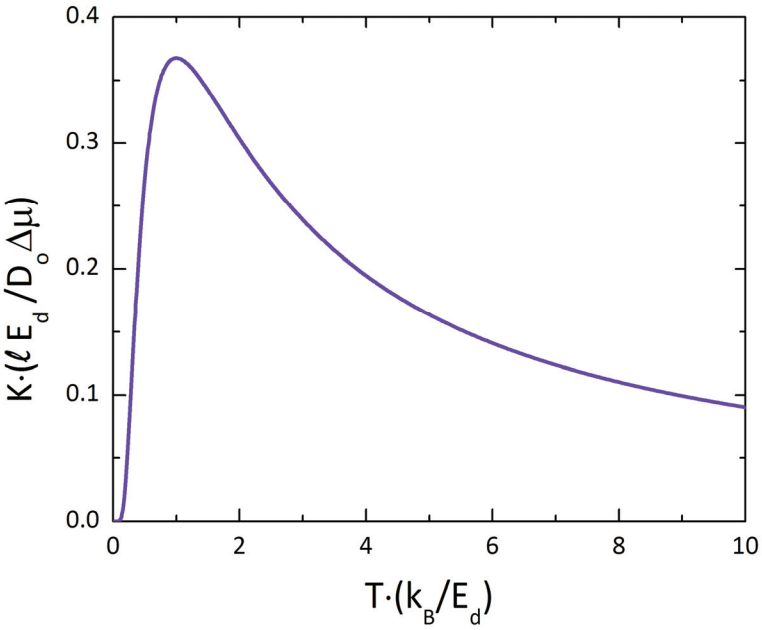

Figure 5.10: Calculated plot of the effective probability for migration and correlated growth showing the dependence on temperature. (Expression derived by Xie, et al. Ref. [89]).

5.6 Conclusions

Growth dynamics provide an additional level of control over the defect structure in doped YBCO films. With increasing temperature, the added mobility allows for migration of the dopant species over longer lengths, further enabling growth to proceed at preferential locations. Thus, the dopant may reduce the strained interfacial area by growing longer nanorods in favor of particles or short segments.

Experimentally, we showed that with increased growth temperature, on average, the BZO nanorods became longer and aligned with reduced splay with respect to the *c*-axis. This shows direct consequence to the vortex pinning properties, with significant increase in $J_c(H)$ for 780° C < T_g < 825° C. While the average nanorod length continued to increase over the range of temperatures measured, the rate of increase in $J_c(H)$ slowed at 835° C, which probably results from the reduced nanorod splay at this growth temperature.

The dynamic effects on BZO self assembly appear to vary when additional dopant phases are introduced. Our results, showing a continued increase in average nanorod length and altered $J_c(H)$ dependence with increasing T_g for 2 vol. % BZO-doped YBCO, deviate from a similar study where BZO and Y_2O_3 inclusions were added. This indicates that BZO self-assembly is impeded by the additional dopant phase, possibly due to variations of the YBCO strain.

Chapter 6

Conclusions and Future Directions

6.1 Conclusions

High temperature superconductors hold promise for diverse power generation applications. However, vortex motion has been a limiting factor to J_c when high magnetic fields are also required. Vortex pinning by insertion of non-superconducting defects like BZO or BSO nanorods into a YBCO matrix improves J_c at increased magnetic fields, especially when incident parallel to the nanorod alignment. These second-phase inclusions happen to self-assemble into columnar structures that provide strong pinning along the length of the flux-line, but current growth methods limit the experimental control of the growth direction. In this thesis, we aimed to produce a defect landscape that was tunable to the demands of an application by studying the mechanisms guiding the nanorod alignment in BZO- and BSO-doped YBCO thin films on vicinal substrates.

By examining the microstructures of BZO-doped YBCO films grown on substrates of varied vicinal angle, we found that a range of nanorod alignments is produced. For the lower vicinal angles of 5° – 10°, the average angular deviation from the YBCO c-axis, or splay, of the nanorods increases by approximately 55% when compared to the nonvicinal films. While at higher angles of 15° – 20°, the nanorods show a dramatic transition to an orthogonal alignment in the *a*-*b* planes of the YBCO. These varied defect geometries produced vortex pinning structures that

improve the $J_c(H)$ and $J_c(\theta)$ over several regimes. For example, significantly broadened peaks were shown for $J_c(H \,||\, c)$ at the 5° vicinal angle, and for $J_c(H \,||\, a\text{-}b)$ at the 10° vicinal angle, when compared to nonvicinal BZO-doped YBCO. The increased $J_c(H \,||\, c)$ may result from reduced vortex hopping aided by the added splay in the BZO nanorods, while prolific planar defects enhance $J_c(H \,||\, a\text{-}b)$. The fully a-b aligned nanorods at the 20° vicinal angle produced an increase in $J_c(H \,||\, a\text{-}b)$, while the $J_c(H \,||\, c)$ curve remained nearly flat, as expected from the defect geometry.

These results begin to show how the $J_c(H,\theta)$ dependence may be tailored through a controlled microstructure. Since the nanorods are thought to assemble by a strain-mediated process, we then consider the effect of the vicinal substrates on the strained interfaces within the doped YBCO film. The widths of the surface terraces on the substrates decrease with increasing vicinal angle, which means that depositing atoms encounter more steps as the vicinal angle is increased. This results in a relative increase in contact area between the film and steps, which produces a net increase in the matrix strain up to a 10° vicinal angle. This increase in strain is indicated by a contracted *c*-axis length and increased average dislocation spacing in the 2 vol. % BZO-doped YBCO film. However, after surpassing a critical vicinal angle of 15° – 20°, further contraction of the *c*-axis may reduce the relative in-plane misfit between the YBCO and BZO such that nanorod growth in the *a*-*b* plane is energetically preferential.

By increasing the dopant concentration, or relative spacing between nanorods, increased magnetic fields may be accommodated by additional pinning centers. However, the reduced nanorod separation also introduces microstructural interactions between the inclusions. At 4 – 6 vol. % BZO doping, we observed that the transition to *a*-*b* aligned nanorods occurs at much lower vicinal angles of 5° – 10°. This indicates the strain fields from adjacent nanorods begin to overlap at the reduced spacing. The additional strain due to the proximity of the nanorods may also reduce the *c*-axis to *a*-*b* plane misfit between the BZO and YBCO, again promoting growth in this direction.

The misfit between the dopant and YBCO matrix affects the dimension of the nanorod inclusions, and, as we have shown using strain modulated growth, also influences the alignment. With a slightly smaller in-plane misfit to YBCO, BSO forms nanorods with larger diameters of approximately 9.5 nm on nonvicinal STO substrates compared to diameters of 5 – 6 nm for BZO. The varied misfit between BZO- and BSO-doped YBCO may then help to verify the role of strain in the nanorod alignment. For YBCO/BSO, the ratio of *c*-axis to *a*-*b* misfit is slightly smaller than that for YBCO/BZO. Therefore, if indeed the *a*-*b* nanorod alignment is favored when this ratio is increased by growth on vicinal substrates, then we would expect the critical angle for realignment to increase. We have observed a mixed distribution of mostly *c*-axis and *a*-*b* aligned nanorods at a 5° vicinal angle in 4.5 vol. % BSO-doped YBCO. Since the 4 vol. % BZO-doped YBCO is dominated by *a*-*b* aligned nanorods at the same vicinal angle, this appears to support the notion of an increased *c* to *a*-*b*

misfit ratio promoting the realignment. However, further support for this finding could be met using a dopant with a more substantial misfit anisotropy, such as the recently reported rare-earth tantalates.

While the equilibrium strain is important in the direction of nanorod alignment, the dynamic conditions for growth are also significant in their formation. By varying the growth temperature, we observed significant changes in the vortex pinning behavior. Distinct increases in $J_c(H)$ were measured with increasing growth temperature in BZO-doped YBCO, reflecting the observed microstructure. Cross-sectional images showed longer, more continuous nanorods at higher temperature, indicating the role of diffusion effects in the self-assembly mechanism. Interestingly, by comparison to data for YBCO films doped with both Y_2O_3 and BZO, our experiments showed significant shifts in nanorod parameters such as average length as a function of growth temperature. This appears to indicate that the presence of additional dopants or nanoparticles act as an inhibitor to nanorod growth, perhaps due to a shifted activation energy.

We have seen that we may produce a controllable defect landscape by manipulation of microstructural and growth conditions. Since both equilibrium strain and dynamic growth conditions play important roles in the formation of second-phase defect structures, methods of controlling these parameters offer a means to tuning the vortex pinning properties of YBCO films to those required for specific applications.

6.2 Future Directions

Many questions remain unanswered about the directional control of nanorods in YBCO thin films, and several experiments may begin to address them. For example, while strain modulation appears to provide an effective method of controlled nanorod alignment, quantitative descriptions of strain distributions surrounding the nanoinclusions are presently unknown. While XRD measurements give an accurate measure of lattice parameters, the values are averaged over relatively large areas of the thin film (several hundred square micrometers). This led, for example, to ambiguity of YBCO *c*-axis length of the BZO-doped 20° vicinal samples, especially in the vicinity of the nanorods (Chapters 3 – 4).

To understand the role of the modulated strain in the nanorod alignment, measurements of the local strain (microstrain) would aid in determining the change in misfit anisotropy leading to the aligned defect structures. A technique particularly suited for these measurements is an electron diffraction method know as Convergent Beam Electron Diffraction (CBED). Using this method, which has been applied in characterizing semiconductor devices, highly accurate (within approximately 0.01% error) measurements of lattice parameters over 4–6 nm diameters are possible [100 – 103]. Many experimental parameters must be carefully controlled in these techniques, including uniformity of sample thickness and the energy distribution of the electron beam [100–101]. However, precise sample preparation techniques, like the FIB methods of Chapter 2 offer this control, and are well suited for these measurements.

In addition, since we saw that growth dynamics through temperature control plays an essential role in the formation of aligned nanorods in YBCO films, more efficient methods of defect landscaping may be sought through processing techniques. For example, since the activation energy plays a significant role in the diffusion of BZO through the YBCO matrix, we may imagine that providing the necessary thermal energy for these processes in post-growth techniques may produce similar results. For example, we may show this experimentally by exposing BZO- or BSO- doped YBCO films grown at lower deposition temperatures (such as the samples shown in Chapter 5 grown in the 780°C range) to higher temperatures after growth. This may alleviate the need for growth temperatures greater than those approaching equipment limits, as was the case for the 835° C samples shown in Chapter 5. The high-temperature post-processing would require heating in an oxygen environment since the YBCO phase is known to lose oxygen content when exposed to temperatures as low as 200° – 300° C [104].

Thus, by understanding the mechanisms and conditions that produce the defect landscapes desired for specific applications, we may attempt to find process variables that may be tuned to produce them using more practical manufacturing techniques. For example, by manipulating the misfit anisotropy through combined defect inclusions, or by post-annealing thin films at high temperatures, it may be possible to produce similar controlled nanorod alignment as shown in this dissertation without the use of costly vicinal substrates or impractical growth conditions.

References

1. **Lehndorff, B. R.** *High-Tc Superconductors for Magnetic and Energy Technology: Fundamental Aspects.* Berlin : Springer, 2001.

2. *High-Tc superconducting materials for electric power applications.* **Larbalestier, D., et al.** 2001, Nature, Vol. 414, pp. 368-377.

3. **Buckel, W. and Kleiner, R.** *Superconductivity: Fundamentals and Applications.* Weinheim : Wiley-VCH, 2004.

4. What is a smart grid? [ed.] Dennis Dimick. *National Geographic Special Edition: Energy for Tomorrow.* June 2009.

5. *Next Generation More-Electric Aircraft: A Potential Application for HTS Superconductors.* **Luongo, C. A., et al.** 2009, IEEE Transactions on Applied Superconductivity, Vol. 19, pp. 1055-1068.

6. **Holtz, R. L., et al.** High Temperature Superconductors for Naval Power Applications. *Materials Science and Technology: 2006 NRL Review.* 2006, pp. 1-3.

7. *Review of high power density superconducting generators: Present state and prospects for incorporating YBCO windings.* **Barnes, P. N., Sumption, M. D. and Rhoads, G. L.** 2005, Cryogenics, Vol. 45, pp. 670-686.

8. **Matthews, J. N. A.** Superconductors to boost wind power. *Physics Today.* April 2009, p. 25.

9. NREL to validate 10-MW superconductor wind turbine. *CompositesWorld.* [Online] Gardner Publications, Inc, February 16, 2009. http://www.compositesworld.com/news/american-superconductor-nrel-planning-10-mw-wind-turbine.aspx.

10. *Materials science challenges for high-temperature superconducting wire.* **Foltyn, S. R., et al.** 2007, Nature Materials, Vol. 6, pp. 631-642.

11. **Matsushita, T.** *Flux Pinning in Superconductors.* Berlin : Springer, 2007.

12. **Huebener, R. P.** *Magnetic Flux Structures in Superconductors.* 2nd ed. Berlin : Springer, 1979.

13. *Flux pinning in superconducting 123 materials.* **Matsushita, T.** 2000, Superconductor Science and Technology, Vol. 13, pp. 730-737.

14. *Studies at IBM on Anisotropy in Single-Crystals of the High-Temperature Oxide Superconductor Y1Ba2Cu3O7-x.* **Gallagher, W. J.** 1988, Journal of Applied Physics, Vol. 63, pp. 4216-4219.

15. *Magnetic Measurements Of The Upper Critical-Field Of YBa2Cu3O7-d Single-Crystals.* **Welp, U., et al.** 1989, Physical Review Letters, Vol. 62, pp. 1908-1911.

16. *Measurements of Anisotropic Characteristic Lengths in YBCO Films at Microwave-Frequencies.* **Jiang, H., et al.** 1993, Journal of Applied Physics, Vol. 73, pp. 5865-5867.

17. *Critical current enhancement in YBa2Cu3O7-d towards the intrinsic depairing value in short current pulses.* **Lang, W., et al.** 2007, Physica C, Vols. 460–462, pp. 827–828.

18. *Direct observation of the depairing current with short current pulses in ultrathin high-temperature superconductor films.* **Puica, I., et al.** 2006, Journal of Physics: Conference Series, Vol. 43, pp. 670–673.

19. *Anisotropy of Critical Current in Layered Oxide Superconductors.* **Tachiki, M. and Takahashi, S.** 1989, Solid State Communications, Vol. 72, pp. 1083-1086.

20. *Angular dependence of critical current density in Y-Ba-Cu-O thin films.* **Horide, T., et al.** 2005, IEEE Transactions on Applied Superconductivity, Vol. 15, pp. 3734-3737.

21. *Vortex confinement by columnar defects in YBa2Cu3O7 crystals: Enhanced pinning at high fields and temperatures.* **Civale, L., et al.** 1991, Physical Review Letters, Vol. 67, pp. 648-651.

22. *Addition of nanoparticle dispersions to enhance flux pinning of the YBa2Cu3O7-x superconductor.* **Haugan, T., et al.** 2004, Nature, Vol. 430, pp. 867-870.

23. *Jc Enhancement in YBa2Cu3Ox Thin Films by Introduction of One-Dimensional Artificial Pinning Centers.* **Matsumoto, K., et al.** 2005, IEEE Transactions On Applied Superconductivity, Vol. 15, pp. 3774-3777.

24. *Strongly enhanced current densities in superconducting coated conductors of YBa2Cu3O7-x + BaZrO3.* **Macmanus-Driscoll, J. L., et al.** 2004, Nature Materials, Vol. 3, pp. 439-443.

25. *Irradiation-free, columnar defects comprised of self-assembled nanodots and nanorods resulting in strongly enhanced flux-pinning in YBa2Cu3O7−δ films.* **Goyal, A., et al.** 2005, Superconductor Science and Technology, Vol. 18, pp. 1533-1538.

26. *Flux pinning enhancement in YBa2Cu3O7-x films with BaSnO3 nanoparticles.* **Varanasi, C. V., et al.** 2006, Superconductor Science and Technology, Vol. 19, pp. L37-L41.

27. **Blatter, G. and Geshkenbein, V. B.** Vortex Matter. [book auth.] K. H. Bennemann and J. B. Ketterson. *The Physics of Superconductors, Vol. I: Conventional and High-Tc Superconductors.* Berlin : Springer, 2003.

28. *Reducing vortex motion in YBa2Cu3O7 crystals with splay in columnar defects.* **Civale, L., et al.** 1994, Physical Review B, Vol. 50, pp. 4102--4105.

29. *Flux pinning effects Of Y2O3 nanoparticulate dispersions in multilayered YBCO thin films.* **Campbell, T. A., et al.** 2005, Physica C, Vol. 423, pp. 1-8.

30. *Transmission Electron Microscopy of YBCO with flux pinning additions* . **Baca, F. J., et al.** Detroit : s.n., 2007. Materials Science and Technology Conference 2007 (MS&T 07).

31. *Temperature and Magnetic Field Dependence of Critical Current Density of YBCO With Varying Flux Pinning Additions.* **Haugan, T. J., et al.** 2009, IEEE Transactions on Applied Superconductivity, Vol. 19, pp. 3270-3274.

32. *Optimization of the BaZrO3 concentration in YBCO films prepared by pulsed laser deposition.* **Peurla, M., et al.** 2006, Superconductor Science and Technology, Vol. 19, pp. 767–771.

33. **Callister, William D.** *Materials Science and Engineering: An Introduction.* Hoboken : John Wiley and Sons, 2007.

34. **Kolasinski, Kurt W.** *Surface Science: Foundations of Catalysis and Nanoscience.* 2nd Edition. West Sussex : John Wiley and Sons, 2008.

35. *Origin of high critical currents in YBa2Cu3O7-d superconducting thin films.* **Dam, B., et al.** 1999, Nature, Vol. 399, pp. 439-442.

36. *Natural strong pinning sites in laser-ablated YBa2Cu3O7-d thin films.* **Huijbregtse, J. M., et al.** 2000, Physical Review B, Vol. 62, pp. 1338-1348.

37. **Norton, D. P.** Pulsed Laser Deposition of Complex Materials: Progress Towards Applications. [book auth.] R. Eason. *Pulsed Laser Deposition of Thin Films: Applications-Led Growth of Functional Materials.* Hoboken : John Wiley and Sons, 2007.

38. *Effect of O2 partial pressure on YBa2Cu3O7-d thin film growth by pulsed laser deposition.* **Haugan, T., et al.** 2003, Physica C, Vol. 397, pp. 47-57.

39. Neocera's Thin-Film Technology. *Neocera Inc.* [Online]

40. *Critical current density and microstructure variations in Ba2Cu3O7−x + BaSnO3 films with different concentrations of BaSnO3.* **Varanasi, C. V., et al.** 2008, Journal of Materials Research, Vol. 23, pp. 3363-3369.

41. *Microstructures and critical current densities of YBCO films containing structure-controlled BaZrO3 nanorods.* **Ichinose, A., et al.** 2007, Superconductor Science and Technology, Vol. 20, pp. 1144–1150.

42. *Self-assembled, rare earth tantalate pyrochlore nanoparticles for superiorflux pinning in YBa2Cu3O7−δ films.* **Harrington, S. A., et al.** 2009, Superconductor Science and Technology, Vol. 22, p. 022001.

43. **Fultz, B. and Howe, J. M.** *Transmission Electron Microscopy and Diffractometry of Materials.* 3rd ed. Berlin : Springer, 2008.

44. Titan Transmission Electron Microscope. *FEI Company.* [Online] 2009. http://www.fei.com/products/transmission-electron-microscopes/titan.aspx.

45. Learn about electron microscopy. *FEI Company Website.* [Online] http://www.fei.com/resources/student-learning/.

46. **Hirsch, P., et al.** *Electron Microscopy of Thin Crystals.* Huntington : Robert E. Krieger Publishing, 1977.

47. **Williams, D. B. and Carter, C. B.** *Transmission Electron Microscopy: A Textbook for Materials Science.* New York : Springer, 1996.

48. **Smith, Donald L.** *Thin Film Deposition: Principles and Practice.* Boston : McGraw-Hill, 1995.

49. **Edington, J. W.** *Practical Electron Microscopy in Materials Science.* New York : Van Nostrand Reinhold Company, 1976.

50. *Identification of the misfit dislocations at YBa2Cu3O7-d/SrTiO3 interface using moiré fringe contrast.* **Wang, H., et al.** 2006, Physica C, Vol. 444, pp. 1-4.

51. *Interfacial Defects and Flux-Pinning Effects in Nanostructured YBa2Cu3O7-d Thin Films.* **Wang, H. and Wang, J.** 2009, IEEE Transactions on Applied Superconductivity, Vol. 19, pp. 3395-3398.

52. This novel method of sample mounting courtesy of Dr. Bob Wheeler, UES Inc., AFRL Microstructural Characterization Facility, WPAFB, Ohio.

53. **Emergo, R. L.** All transport measurements courtesy of Rose Emergo, University of Kansas..

54. **Emergo, Rose Lynn.** *PhD Dissertation, University of Kansas.* Lawrence : s.n., 2009.

55. *Effects of nanocrystalline target and columnar defects on flux pinning in pure and BaZrO3-doped YBa2Cu3O6+x films in fields up to 30 T.* **Peurla, M., et al.** 2007, Physical Review B, Vol. 75, p. 184524.

56. *Growth mode issues in epitaxy of complex oxide thin films.* **Dam, B. and Stauble-Pumpin, B.** 1998, Journal of Materials Science: Materials in Electronics, Vol. 9, pp. 217-226.

57. *Growth mechanism of sputtered films of YBa2Cu3O7 studied by scanning tunneling microscopy.* **Hawley, M., et al.** 1991, Science, Vol. 251, pp. 1587-1589.

58. *Fermi level pinning by misfit dislocations at GaAs Interfaces.* **Woodall, J. M., et al.** 1983, Physical Review Letters, Vol. 51, pp. 1783-1786.

59. *Strong isotropic flux pinning in solution-derived YBa2Cu3O7−x nanocomposite superconductor films.* **Gutierrez, J., et al.** 2007, Nature Materials, Vol. 6, pp. 367-373.

60. *In-field critical current of type-II superconductors caused by strain from nanoscale columnar inclusions.* **Rodriguez, J. P., Barnes, P. N. and Varanasi, C. P.** 2008, Physical Review B, Vol. 78, p. 052505.

61. *Strain control and spontaneous phase ordering in vertical nanocomposite heteroepitaxial thin films.* **MacManus-Driscoll, Judith L., et al.** 2008, Nature Materials, Vol. 7, pp. 314-320.

62. *Structural phase transitions and stress accommodation in () composite films.* **Lebedev, O. I., et al.** 2002, Physical Review B, Vol. 66, p. 104421.

63. *Self-assembled growth of BiFeO3-CoFe2O4 Nanostructures.* **Zheng, H., et al.** 2006, Advanced Materials, Vol. 18, pp. 2747-2752.

64. *Multiferroic BaTiO3-CoFe2O4 nanostructures.* **Zheng, H., et al.** 2004, Vol. 303, pp. 661-663.

65. *Structure and properties of artificial [(La0.7Sr0.3MnO3)m (SrTiO3)n]15 superlattices on (001) SrTiO3.* **Lebedev, O. I., et al.** 2003, Journal of Applied Physics, Vol. 94, pp. 7646-7656.

66. **Zangwill, Andrew.** *Physics at Surfaces.* Cambridge : Cambridge UP, 1988.

67. *Properties of YBa2Cu3O7-d thin films grown on vicinal SrTiO3 (001) substrates.* **Mechin, L., Berghuis, P. and Evetts, J. E.** 1998, Physica C, Vol. 302, pp. 102-112.

68. **Venables, John A.** *Introduction to Surface and Thin Film Processes.* Cambridge : Cambridge UP, 2000.

69. *Steps on surfaces: experiment and theory.* **Jeong, Hyeong-Chai and Williams, Ellen D.** 1999, Surface Science Reports, Vol. 34, pp. 171-294.

70. *Energies of steps, kinks, and defects on Ag{100} and Ag{111} using the embedded atom method, and some consequences.* **Nelson, R. C., Einstein, T. L. and Khare, S. V.** 1993, Surface Science, Vol. 295, pp. 462-484.

71. *Growth mechanism of YBa2Cu3O7−d thin films and precipitates on planar and vicinal SrTiO3 substrates.* **Kim, J., et al.** 2000, Journal of Materials Research, Vol. 15, pp. 596-613.

72. *Strong nanopore pinning enhances Jc in YBa2Cu3O7-d films.* **Wu, J. Z., et al.** 2007, Applied Physics Letters, Vol. 93, p. 062506.

73. *Tuning porosity of YBa2Cu3O7−d vicinal films by insertion of Y2BaCuO5 nanoparticles.* **Emergo, R. L. S., et al.** 2005, Applied Physics Letters, Vol. 87, p. 232503.

74. *Pore formation and increased critical current density in YBa2Cu3Ox films deposited on a substrate surface modulated by Y2O3 nanoparticles.* **Baca, F. J., et al.** 2007, Superconductor Science and Technology, Vol. 20, pp. 554–558.

75. *Ultra-high flux pinning properties of BaMO3-doped YBa2Cu3O7−x thin films (M = Zr, Sn).* **Mele, P., et al.** 2008, Superconductor Science and Technology, Vol. 21, p. 032002.

76. *Enhanced Pinning with Controlled Splay Configurations of Columnar Defects; Rapid Vortex Motion at Large Angles.* **Krusin-Elbaum, L., et al.** 1996, Physical Review Letters, Vol. 76, pp. 2563-2566.

77. *Unpublished.* **Emergo, R. L., et al.**

78. *Transport properties and flux pinning by self-organization in YBa2Cu3O7-d films on vicinal SrTiO3 (001).* **Haage, T., et al.** 1997, Physical Review B, Vol. 56, pp. 8404-8418.

79. *Growth mechanism of YBa2Cu3O7 thin films on vicinal MgO.* **Norton, M. Grant, et al.** 1991, Journal of Crystal Growth, Vol. 114, pp. 258-263.

80. **Norton, M. Grant and Carter, C. Barry.** Observations on the Growth of YBa2Cu3O7-d Thin Films by Transmission Electron Microscopy. [ed.] Subhash L. Shinde and David A. Rudman. *Interfaces in High-Tc Superconducting Systems.* New York : Springer-Verlag, 1993, 1, pp. 1-27.

81. *Anisotropic nonmonotonic behavior of the superconducting critical current in thin YBa2Cu3O7−d films on vicinal SrTiO3 surfaces.* **Cantoni, C., et al.** 2005, Physical Review B, Vol. 71, p. 054509.

82. *Effects of surface miscuts on the epitaxy of YBa2Cu3O7-d and NdBa2Cu3O7-g on SrTiO3 (001).* **Maurice, J.-L., et al.** 2003, Physical Review B, Vol. 68, p. 115429.

83. *Vortex confinement by columnar defects in YBa2Cu3O7 crystals: enhanced pinning at high fields and temperatures.* **Civale, L., et al.** 1991, Physical Review Letters, Vol. 67, pp. 648-651.

84. *Magnetic field dependence of the critical current and the flux pinning mechanism in YBa2Cu3O6+x films doped with BaZrO3.* **Traito, K., et al.** 2006, Physical Review B, Vol. 76, p. 224522.

85. *Systematic study of the BaSnO3 insertion effect on the properties of YBa2Cu3O7-x films prepared by pulsed laser ablation.* **Mele, P., et al.** 2008, Superconductor Science and Technology, Vol. 21, p. 125017.

86. **Russ, John C.** *The Image Processing Handbook.* Boca Raton : CRC Press, 2007.

87. **Schroeder, Daniel V.** *An Introduction to Thermal Physics.* San Francisco : Addison Wesley Longman, 2000.

88. **Howe, James M.** *Interfaces in Materials.* New York : John Wiley and Sons, 1997.

89. *Vertically Self-Organized InAs Quantum Box Islands on GaAs(100).* **Xie, Qianghua, et al.** 13, September 1995, Physical Review Letters, Vol. 75, pp. 2542-2545.

90. **Goyal, A., et al.** *Engineered columnar defects for coated conductors.* s.l. : DOE High Temperature Superconductivity (HTS) Program Peer Review, 2009.

91. *Microstructure and critical current density of YBa2Cu3O7-x + BaSnO3 thick films grown with pre-mixed pulsed laser ablation target.* **Burke, J., et al.** 2010, To be published in Advances in Cryogenic Engineering-Materials.

92. *Influence of growth temperature on critical current and magnetic flux pinning structures in YBa2Cu3O7−x.* **Feldmann, D. M., et al.** 2007, Appl. Phys. Lett. , Vol. 91, p. 162501.

93. *Phase equilibria in the Y-Ba-Cu-O system and melt processing of Ag clad Y1BaECU307-x tapes at reduced oxygen partial pressures.* **MacManus-Driscoll, J. L., Bravman, J. C. and Beyers, R. B.** 1995, Physica C, Vol. 241, pp. 401-413.

94. **Rijnders, Guus and Blank, Dave H. A.** Growth Kinetics During Pulsed Laser Deposition. [book auth.] Robert Eason. *Pulsed Laser Deposition of Thin Films: Applications-Led Growth of Functional Materials.* Hoboken : John Wiley and Sons, 2007.

95. *Flux pinning in YBa2Cu3O7−d thin film samples linked to stacking fault density.* **Wang, J., et al.** 2008, Applied Physics Letters, Vol. 92, p. 082507.

96. *Synergetic combination of different types of defect to optimize pinning landscape using BaZrO3-doped YBa2Cu3O7.* **Maiorov, B., et al.** 2009, Nature Materials, Vol. 8, pp. 398 - 404.

97. **Kittel, Charles.** *Introduction to Solid State Physics, 8th ed.* Hoboken : John Wiley and Sons, 2005.

98. *Self-Organization in Growth of Quantum Dot Superlattices.* **Tersoff, J., Teichert, C. and Lagally, M. G.** 1996, Physical Review Letters, Vol. 76, pp. 1675-1678.

99. *Competing relaxation mechanisms in strained layers.* **Tersoff, J. and LeGoues, F. K.** 1994, Physical Review Letters, Vol. 72, pp. 3570-3573.

100. **Spence, J. C. H. and Zuo, J. M.** *Electron Microdiffraction.* New York : Plenum Press, 1992.

101. *Conventional transmission electron-microscopy techniques in convergent-beam electron diffraction.* **Tanaka, M.** 1986, Journal of Electron Microscopy, Vol. 35, pp. 314-323.

102. *High-resolution strain measurement in shallow trench isolation structures using dynamic electron diffraction.* **Kim, M., Zuo, J. M. and Park, G.-S.** 2004, Applied Physics Letters, Vol. 84, pp. 2181-2183.

103. *Residual strain measurement of SOI wafer using convergent beam electron diffraction.* **Kuramochi, K., et al.** 2005, Microscopic Microanalysis, Vol. 11, pp. 776-777.

104. **Knizhnik, A.** Times of establishing, positions and constants of equilibrium of YBCO with oxygen. [book auth.] D. M. Friedman. *New Research on YBCO Superconductors.* s.l. : Nova Science Publishers, 2008, pp. 265-277.

Publication List

2009

21. **F. J. Baca**, P. N. Barnes, R. L. Emergo, T. J. Haugan, J. N. Reichart, and J. Z. Wu, "Control of $BaZrO_3$ nanorod alignment in $YBa_2Cu_3O_{7-x}$ thin films by microstructural modulation" *Applied Physics Letters* **94**, 102512 (2009).

20. **F. J. Baca**, R. L. Emergo, J. Z. Wu, T. J. Haugan, J. N. Reichart, and P. N. Barnes, "Microstructural characterization of $YBa_2Cu_3O_{7-x}$ films with $BaZrO_3$ nanorods grown on vicinal $SrTiO_3$ substrates" *IEEE Transactions on Applied Superconductivity* **19**, 3371 (2009).

19. T. J. Haugan, **F. J. Baca**, M. J. Mullins, N. A. Pierce, T. A. Campbell, E. L. Brewster, P. N. Barnes, H. Wang, and M. D. Sumption, "Temperature, Angle and Field Dependence of YBCO with Nanoparticle and Nanorod Flux Pinning Additions" *IEEE Transactions on Applied Superconductivity,* **19**, 3270 (2009).

18. P. N. Barnes, T. J. Haugan, **F. J. Baca**, C. V. Varanasi, R. Wheeler, F. Meisenkothen, and S. Sathiraju, "Inducing self-assembly of Y_2BaCuO_5 nanoparticles via Ca-doping for improved pinning in $YBa_2Cu_3O_{7-x}$" Invited contribution, accepted for publication in *Physica C* (2009).

17. G. Xu, Z. Z. Li, **J. Baca**, and J. Wu, "Probing Nucleation Mechanisms of Self-catalyzed InN Nanostructures" accepted for publication in *Nanoscale Research Letters* (2009).

16. **F. J. Baca**, P. N. Barnes, T. J. Haugan, J. N. Reichart, and J. Z. Wu "Controlled Correlation of $BaZrO_3$ Nanorods in $YBa_2Cu_3O_{7-x}$ Thin Films through Controlled Growth Dynamics," In preparation for publication.

15. **F. J. Baca**, R. L. Emergo, J. Z. Wu, J. Burke, C. V. Varanasi, T. J. Haugan, and P. N. Barnes "Controlled Alignment of Nanostructures through Global and Local Strain Mediation in $YBa_2Cu_3O_{7-x}$ Thin Films," In preparation for publication.

14. C. Rochford, Z. Z. Li, **F. J. Baca**, J. Wu, J. Liu, J. Li "The effect of crystallinity on the photoconductivity of individual CNF/TiO_2 core-shell nanowires," Submitted for publication in *Nano Letters.*

13. B. –H. Tsao, J. W. Lawson, J. D. Scofield, and **J. Baca** "TEM Observations of Ti/AlNi/Au Contacts on p-Type 4H-SiC," Submitted for publication in *Materials Science Forum*.

12. R. L. Emergo, **F. J. Baca**, J. Z. Wu, T. J. Haugan, and P. N. Barnes, "3-D landscaping of $BaZrO_3$ nanorods in $YBa_2Cu_3O_{7-\delta}$," In preparation for publication.

11. R. L. S. Emergo, **F. J. Baca**, J. Z. Wu, T. J. Haugan, and P. N. Barnes "Thickness evolution of splayed $BaZrO_3$ nanorods in $YBa_2Cu_3O_{7-\delta}$ films." In preparation for publication.

10. Z. Z. Li, C. Rochford, **J. Baca**, J. Wu, J. Liu, and Jun Li, "Investigation of Photoconductivity in single CNF/TiO_2-dye core-shell nanostructure" Submitted for publication.

2008

9. Z. Z. Li, **J. Baca**, and J. Wu, "In situ switch of boron nanowire growth mode from vapor-liquid-solid to oxide-assisted growth" *Applied Physics Letters* **92**, 113104 (2008).

8. Z. Z. Li, **J. Baca**, S. H. Yun, and J. Wu, "Gold/Boron core-shell nanocables synthesized from gold-boron eutectic droplets" *Nanotechnology* **19**, 55606 (2008).

7. J. Wang, J. H. Kwon, J. Yoon, H. Wang, T. J. Haugan, **F. J. Baca**, N .A. Pierce, and P. N. Barnes, "Flux pinning in $YBa_2Cu_3O_{7-d}$ thin film samples linked to stacking fault density" *Applied Physics Letters* **92**, 082507 (2008).

6. C. Varanasi, J. Bulmer, L. Brunke, J. Burke, **J. Baca**, K. Yost, and P. Barnes, "Growth and Characterization of Carbon Nanotubes on Constantan (Ni-Cu-Mn Alloy) Metallic Substrates without Adding Additional Catalysts" *J. Vacuum Science and Technology A* **26**, 832 (2008).

2007 and Prior

5. **F. J. Baca**, D. Fisher, R. L. S. Emergo and J. Z. Wu, "Pore formation and increased critical current density in $YBa_2Cu_3O_x$ films deposited on a substrate surface modulated by Y_2O_3 nanoparticles" *Superconductor Science and Technology* **20**, 554 (2007).

4. T. J. Haugan, P. N. Barnes, T. A. Campbell, N. A. Pierce, **F. J. Baca**, M. F. Locke, I. Brockman, A. L. Westerfield, J. M. Evans, R. Morgan, P. Klenk, B. C. Harrison, A. D. Chaney and I. Maartense, "Superconducting Properties of $(M_x/YBa_2Cu_3O_{7-\delta\ y})_N$ Multilayer Films With Variable Layer Thickness x" *Journal of Electronic Materials* **36**, 1234 (2007).

3. T. J. Haugan, P. N. Barnes, T. A. Campbell, N. A. Pierce, **F. J. Baca** and I. Maartense, "Flux Pinning of Y-Ba-Cu-O Films Doped with $BaZrO_3$ Nanoparticles by Multilayer and Single Target Methods" *IEEE Transactions on Applied Superconductivity* **17**, 3724 (2007).

2. J. R. Dizon, H. Zhao, **J. Baca**, S. Mishra, R. L. Emergo, R. S. Aga, Jr. and J. Z. Wu, "Fabrication and characterization of two-pole X-band $HgBa_2CaCu_2O_{6+d}$ microstrip filters" *Applied Physics Letters* **88**, 092507 (2006).

1. D. Neimeier, D. Oesch, J. Andrews, **J. Baca**, and S.W. Teare, "Multiwavelength differential image motion monitor" *Optics Express* **10**, 561 (2002).